FRIEDRICH-SCHILLER-
UNIVERSITÄT
JENA

UNIVERSITÄTS
KLINIKUM
jena

DISSERTATION

zur Erlangung des akademischen Grades
Doctor rerum naturalium Dr. rer. nat.

Multiparametric quantitative Magnetic Resonance Imaging of musculoskeletal tissues in vivo

---

vorgelegt dem Rat der Medizinischen Fakultät der
Friedrich-Schiller-Universität Jena von

Marta Brigid Maggioni

Jena, 01.08.2024

Gutachter (akademischer Grad, Vor- und Nachname sowie Wirkungsort)
1. Prof. Dr. Jürgen Reichenbach, Jena
2. Prof. Dr. Ferdinand Von Eggeling, Jena
3. Prof. Dr. Fritz Schick, Tübingen
Tag der öffentlichen Verteidigung: 18.06.2024

Contents

1. List of abbreviations

ADC	**A**pparent **D**iffusion **C**oefficient
AFI	**A**ctual **F**lip angle **I**maging
FA	**F**lip **A**ngle
FLASH	**F**ast **L**ow **A**ngle **SH**ot
FFT	**F**ast **F**ourier **T**ransform
GRE	**GR**adient **E**cho
IVIM	**I**ntra **V**oxel **I**ncoherent **M**otion
MR	**M**agnetic **R**esonance
MRI	**M**agnetic **R**esonance **I**maging
MRS	**M**agnetic **R**esonance **S**pectroscopy
NMR	**N**uclear **M**agnetic **R**esonance
MT	**M**agnetisation **T**ransfer
NSLBP	**N**on **S**pecific **L**ow **B**ack **P**ain
OA	**O**steo**A**rthritis
PGSE	**P**ulsed **G**radient **S**pin **E**cho
qMRI	**q**uantitative **M**agnetic **R**esonance **I**maging
ROI	**R**egion **O**f **I**nterest
RF	**R**adio **F**requency
Rx	**R**eceive
SE	**S**pin **E**cho
TE	**E**cho **T**ime
TR	**R**epetition **T**ime
Tx	**T**ransmit
UTE	**U**ltrashort **E**cho **T**ime
VFA	**V**ariable **F**lip **A**ngle
VTR	**V**ariable **T**ime **R**epetition

2. Summary

Magnetic Resonance Imaging (MRI) has established itself as a very reliable non-invasive imaging method for a large part of the musculoskeletal system (de Mello et al., 2019).

Traditionally, the examination of the musculoskeletal system has been limited to qualitative MRI sequences. However, as the interest in musculoskeletal MRI application has kept growing over the years (Solomon et al., 2003), an emerging field is quantitative MRI (qMRI). QMRI lends itself as a complementary tool to the standard qualitative diagnostic imaging methods by providing quantitative values of various MR-related parameters. These parameters have been shown to aid in early disease detection, enable comparative studies and treatment monitoring (Mosher, 2006; Ahn and El-Khoury, 2007; de Mello et al., 2019). Yet, despite this increased interest, numerous areas still remain relatively underresearched.

The primary goal of this work was to contribute to this quantification effort in such less well researched areas, by providing reference values and improving existing MR techniques. Specifically, qMRI methods were applied on tendons of the knee and the lumbar back muscles at rest, which constitute crucial components of the musculoskeletal system and are often considered together as the muscle-tendon unit.

Due to microstructural differences between tendons and muscles, different challenges remained to be addressed in their quantification: in tendons, the main challenge is the very fast decay of the MR signal, which has significantly hindered qMRI applications in these tissues in the past. Only with recently developed Ultrashort Echo Time (UTE) sequences, it has become feasible to capture signal in tendons, opening the door to qMRI applications (Qian et al., 2012). Similarly, the (more subtle) long-term effects of exercise on the lumbar back muscle, have rarely been analysed with qMRI at rest, instead the majority of research focuses on measuring the more prominent changes of MR quantitative parameters immediately after a strenuous exercise session (Fleckenstein et al., 1988; Hiepe et al., 2012; Hata et al., 2019; Zaeske et al., 2022).

In this work, different MRI methods were used to address aforementioned challenges. UTE sequences were used for the knee tendons applications, whereas a pilot study on the lumbar back muscle was conducted with a combination of conventional MR techniques.

The difficulties in obtaining signals from tendons limits the available literature on the values of qMRI parameters in these tissues. To tackle this issue the UTE results obtained in this work were validated in phantoms (where the expected values of the relaxation parameters are known a priori) and by comparing different methods to measure T_1 (see 5.1).

In order to achieve accurate and reliable values of T_1, B_1 field inhomogeneities had to be taken into account. Mapping and correcting for these inhomogeneities is essential for achieving accurate quantification of T_1 relaxation parameter values. However, most of the

well established B_1-field mapping methods are not compatible with UTE acquisition due to its short echo times. While the Actual Flip angle (AFI) method can be implemented with UTE acquisition, it is very time consuming and dependent on multiple spoiling parameters (Yarnykh, 2007; Nehrke, 2009). In this work, an original improvement of the AFI method is used, which allows for faster acquisition times and greater robustness against spoiling parameters compared to the previous implementations (see 5.2).

Expanding upon the previously investigated qMRI parameters, a pilot study in the lumbar back muscles (see 5.3), was conducted. This study encompassed a comprehensive multiparametric MR protocol. This protocol included not only T_2, and B_1-corrected T_1 (as in the aforementioned knee results) but also fat fraction, and IVIM diffusion parameter values, which are essential for quantitative muscle tissue characterisation. This protocol was applied to three healthy, differently trained cohorts. With the help of a group analysis, it was possible to determine that the physiological changes resulting from repetitive long-term physical activity indeed impact the qMRI parameters listed above. This approach also helped to identify which of those demonstrated the highest sensitivity to these training-induced changes. The results indicated significant differences between trained and untrained subjects for T_2, fat fraction and IVIM perfusion fraction, while the longitudinal component of the diffusion tensor effectively differentiated between the two athletes cohorts.

In conclusion, this work aims to fill gaps in qMRI for musculoskeletal applications in vivo, with a specific focus on tendons and muscles. For tendons of the knee, this work not only contributed to establish a baseline of quantitative MR values but also supported the effort for accurate T_1 quantification. To tackle this latter challenge, a novel implementation of a UTE compatible B_1-field mapping method was developed. Additionally the application of multiparametric methods was extended to assess training induced adaptations in the lumbar back muscle, specifically targeting the less well researched context of resting conditions.

2. Zusammenfassung

Die Magnetresonanztomographie (MRT) hat sich als sehr zuverlässige nicht-invasive Bildgebungsmethode für einen großen Teil des Bewegungsapparats etabliert (de Mello et al., 2019).

Traditionell war die Untersuchung des Bewegungsapparats auf qualitative MRT Sequenzen beschränkt. Neben dem allgemein steigenden Interesse an der Anwendung der MRT für den Bewegungsapparat (Solomon et al., 2003), hat sich mit der quantitativen MRT (qMRT) zusätzlich ein neuer Bereich etabliert. QMRT ist eine hervorragende Erweiterung der standardmäßigen qualitativen diagnostischen Bildgebungsverfahren, da es verschiedene MR-bezogener Parameter quantifiziert. Die Quantitativen Parameter helfen nachweislich bei der Früherkennung von Krankheiten, ermöglich vergleichende Studien und die Behandlungsüberwachung (Mosher, 2006; Ahn and El-Khoury, 2007; de Mello et al., 2019). Trotz der bekannten Schwierigkeiten quantitativer Analysen in der MRT nimmt das Interesse qMRT gerade auch für den Bewegungsapparat stark zu.

Das Hauptziel dieser Arbeit war es, durch die Bereitstellung von Referenzwerten und die Verbesserung bestehender MR-Techniken einen Beitrag zu den Quantifizierungsbemühungen in diesen weniger gut erforschten Bereichen zu leisten. Konkret wurden qMRI-Methoden an den Kniesehnen und der lumbalen Rückenmuskulatur im Ruhezustand angewandt, die wichtige Komponenten des Bewegungsapparats darstellen und oft als Muskel-Sehnen- Einheit betrachtet werden.

Aufgrund der mikrostrukturellen Unterschiede zwischen Sehnen und Muskeln waren bei ihrer Quantifizierung verschiedene Herausforderungen zu bewältigen: Bei Sehnen besteht die größte Herausforderung im sehr schnellen Abklingen des MR-Signals, was in der Vergangenheit qMRT-Anwendungen in diesen Geweben erheblich behindert hat. Erst mit den kürzlich entwickelten Sequenzen mit ultrakurzer Echozeit (UTE) ist es möglich geworden, Signale in Sehnen zu erfassen und damit die Tür für qMRI-Anwendungen zu öffnen (Qian et al., 2012). In ähnlicher Weise wurden die (subtileren) langfristigen Auswirkungen von Training auf den lumbalen Rückenmuskel nur selten mit qMRI im ausgeruhten Zustand analysiert; stattdessen konzentriert sich die Mehrheit der Forschung auf die Messung der auffälligeren Veränderungen der quantitativen MR-Parameter unmittelbar nach einer anstrengenden Trainingseinheit (Fleckenstein et al., 1988; Hiepe et al., 2012; Hata et al., 2019; Zaeske et al., 2022).

In dieser Arbeit wurden verschiedene MRT-Methoden verwendet, um die vorgenannten Herausforderungen zu bewältigen. Für die Kniesehnen wurden UTE-Sequenzen verwendet, während eine Pilotstudie an der lumbalen Rückenmuskulatur mit einer Kombination aus konventionellen MR-Techniken durchgeführt wurde.

Die Schwierigkeiten bei der Gewinnung von Signalen aus Sehnen limitiert die verfügbare Literatur über die Werte der qMRT-Parameter in diesen Geweben . Um dieses Problem anzugehen, wurden die in dieser Arbeit erzielten UTE-Ergebnisse in Phantomen, mit a priori bekannten Relaxationsparametern, und durch den Vergleich verschiedener Methoden zur Messung von T_1 (see 5.1) validiert.

Um zuverlässig genaue T_1-Werte zu erhalten, mussten B_1-Feld-Inhomogenitäten berücksichtigt werden. Die Erfassung und Korrektur dieser Inhomogenitäten ist eine wesentliche Voraussetzung für eine genaue Quantifizierung der T_1-Relaxationsparameterwerte.

Die meisten der etablierten B_1-Feld-Mapping-Methoden sind jedoch aufgrund der kurzen Echozeiten nicht mit der UTE-Methode kompatibel. Die Actual Flip Angle (AFI)-Methode kann zwar bei UTE-Akquisition implementiert werden, ist aber sehr zeitaufwändig und von mehreren Spoiling-Parametern abhängig (Yarnykh, 2007; Nehrke, 2009). In dieser Arbeit wird eine selbstentwickelte Verbesserung der AFI-Methode eingesetzt, die im Vergleich zu den bisherigen Implementierungen eine schnellere Akquisition und eine größere Robustheit gegenüber Spoiling-Parametern ermöglicht (see 5.2).

Zusätzlich zu den zuvor untersuchten qMRT-Parametern wurde eine Pilotstudie an der Lendenwirbelsäulenmuskulatur (see 5.3) durchgeführt. Diese Studie umfasste ein multiparametrisches MR-Protokoll, nicht nur T_2 und B_1-korrigiertes T_1 (wie in den obigen Knieergebnissen), sondern auch den Fettanteil und die IVIM-Diffusionsparameterwerte, die für die quantitative Charakterisierung des Muskelgewebes wesentlich sind. Dieses Protokoll wurde auf drei gesunde, unterschiedlich trainierte Kohorten angewandt. Mit Hilfe einer Gruppenanlayse konnte gezeigt werden, dass die physiologischen Veränderungen aufgrund wiederholter, langfristiger körperlicher Aktivität, tatsächlich Auswirkungen auf die oben genannten qMRT-Parameter haben. Mit Hilfe dieses Ansatzes konnte auch ermittelt werden, welche dieser Parameter die höchste Empfindlichkeit für diese trainingsbedingten Veränderungen aufweisen. Die Ergebnisse zeigten signifikante Unterschiede zwischen trainierten und untrainierten Probanden für die qMRT Parameter T_2, Fettanteil und IVIM-Perfusionsanteil, während die longitudinale Komponente des Diffusionstensors effektiv zwischen den beiden Sportlerkohorten differenzierte.

Zusammenfassend schliesst diese Arbeit Lücken des qMRT für muskuloskelettale Anwendungen in vivo, wobei der besondere Anwendungsschwerpunkt auf Sehnen und Muskeln liegt. Für die Sehnen des Knies hat diese Arbeit nicht nur dazu beigetragen, eine Referenz quantitativer MR-Werte zu erstellen, sondern auch die genaue T_1-Quantifizierung verbessert. Für letzteres wurde eine neuartige Implementierung einer UTE-kompatiblen B_1-Feld Mapping-Methode entwickelt. Darüber hinaus wurde die Anwendung multiparametrischer Methoden erweitert, um trainingsbedingte Anpassungen im lumbalen Rückenmuskel, insbesondere im weniger gut erforschte Kontext der Ruhebedingungen, zu bewerten.

3. Introduction

3.1 Quantitative MRI

While MRI is used daily in the clinical practice as a diagnostic imaging method, the majority of its applications rely on the use of MRI as a qualitative tool (Cashmore et al., 2021). In such instances, the MRI images are represented by grayscale values and evaluated by trained radiologists. The crucial aspect for diagnosis revolves around the relative intensity differences, i.e., the contrast between various tissues or between healthy and pathological areas.

The focus of this work, instead, is on the use of MRI as a quantitative tool to aid in the characterisation of musculoskeletal tissues. Quantitative MRI focuses on extracting absolute values of parameters that depend on the biophysical properties of the tissues and can be obtained by fitting the behaviour of the MR signal in each voxel to known mathematical models. This shift is fundamental for data-driven diagnosis, and it supports the move towards precision medicine, which is based on (more) objective metrics (Keenan et al., 2019). Some of the benefits of this approach (Granziera et al., 2021) range from early disease detection - before any visual changes are visible in the qualitative grayscale images (Bydder et al., 1982) - to tissue characterisation (Bennett et al., 2019) to assessment of treatment response, without the need of more invasive procedures such as biopsies (Keenan et al., 2021).

3.2 Musculoskeletal system

The musculoskeletal system is composed of bones and muscles along with connective structures, such as tendons (which link bones to muscles), ligaments (which join bones to other bones), cartilage (which provides cushioning at the joints) and connective tissues. Its unique functions are postural support, movement and protection against injuries (Kucharz, 1992).

Muscles and tendons (which are the focus of this work) are sometimes referred to as the muscle and tendon unit (Finni, 2006), due to their interconnected and interdependent roles in producing movement and transmitting forces. The muscle-tendon unit plays a central role in human movement and physical function, facilitating the transmission of forces generated by muscle contractions to produce joint motion and perform mechanical work (Finni, 2006; Tadros et al., 2018).

The knee is the largest joint in the body (Affatato, 2015) and plays a crucial role in supporting a significant portion of the body weight and facilitating a broad range of motion with six degrees of freedom in its range of motion (Hirschmann and Müller, 2015). More precisely the knee is a double-joint structure – the tibio-femoral joint and the patello-femoral

joint – and is composed by four bones (tibia, femur, patella, fibula) and a complex system of soft tissues, tendons, ligaments and muscles (see Figure 3.1, left). For the sake of this work, the focus is going to be on tendons and ligaments, in particular on the patellar and quadriceps tendons. The patellar tendon starts at the bottom of the patella and connects it to the front of the tibia. Functionally, since it connects two bones, it is by definition a ligament, but more often referred to as a patellar tendon, reflecting its role in transmitting forces from the quadriceps muscle to the tibia via the patella (Hansen et al., 2006). The quadriceps tendon attaches the quadriceps muscles group (one of the largest in the body) to the patella. Interestingly, the patellar bone is embedded in the quadriceps tendon allowing for better force transmission (Márquez-Flórez et al., 2018). In the realm of quantitative MRI, unique challenges arise because of the heterogeneous nature of musculoskeletal tissues in the knee: ranging from the dense mineralized matrix of bone to the fibrous architecture of tendons, to the soft contractile features of muscles, which leads to very different MRI signal behaviours, and requires specialized sequences to investigate them.

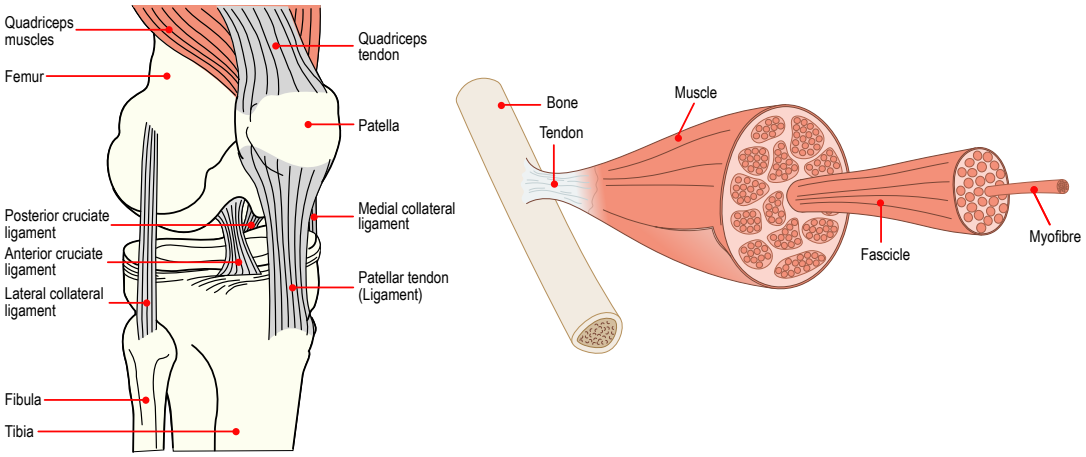

FIGURE 3.1: On the left: Illustration of the human knee: the bones, tendons, ligaments and muscles of the knee are outlined and labelled. On the right: the main components of skeletal muscles along with the muscle-tendon unit are shown. The muscle image is adapted from "Muscle schematic.svg" © Tomáš Kebert CC-BY-SA-4.0

Muscles are considered the largest organ in the body (Pedersen, 2011), and the focus of this work is on skeletal muscles of the knee and the Erector Spinae and Multifidus muscles, of the lumbar spine. Skeletal muscles are highly organised tissues (see Figure 3.1, right) composed by several bundle of myofibres. Myofibres are the cell unit of muscles and contain chains of myofibrils. Myofibres group together to create fascicles, and bundle of fascicles compose the muscle tissue. A comprehensive review of skeletal muscle function and structure is given by (Mukund and Subramaniam, 2020). Muscles are themselves heterogeneous tissues due to the presence of fascia, connective tissues, and notably, in the lumbar

spine region, fat infiltrations (Damon et al., 2016). Such diversity constitutes a challenge in qMRI to properly differentiate the different components of the analysed region.

Nonetheless, despite these challenges, qMRI remains the primary imaging approach to research the musculoskeletal system by providing a non-invasive and versatile tool which combines the soft-tissue contrast with a variety of sequences and parameters that can be optimised to answer many different clinical and research questions. This adaptability has led to improved musculoskeletal tissues characterisation (Mazzoli et al., 2016; Kalia et al., 2017), a deeper comprehension of biomechanical mechanisms (Eck et al., 2023) as well as diagnostic tools (such as multi parametric protocols) for early diagnosis and better prognosis of both acute and degenerative musculoskeletal illnesses (Stahl et al., 2009).

Relevancy of musculoskeletal qMRI for the clinical practice

Even tissues, previously considered very difficult to image, such as tendons and ligaments can now be investigated due to the introduction of Ultrashort Echo Time sequences (Du et al., 2010; Du and Bydder, 2013; Matzat et al., 2013). A comprehensive review of such recent advancements in qMRI and UTE sequences for musculoskeletal applications is presented in (Bydder et al., 2012; Visser et al., 2020; Afsahi et al., 2022) and in section 3.8 of this thesis.

In clinical practice, one example of how these advancements have proven to be useful, is in the diagnosis and management of rotator cuff tears. Traditional diagnostic methods such as physical examination or ultrasound may give preliminary information, but MRI is preferred for surgical planning and is more reliable in the estimation of tears size, depth and location (Zlatkin et al., 1989; Okoroha et al., 2017; Zoga et al., 2021). Another example is patellar tendinopathy: quantitative UTE MRI methods have been proposed, showing the potential of the relaxation parameter T_2^* in assessing the hydration state (Argentieri et al., 2017; Breda et al., 2020) and collagen matrix structure for the patellar tendon, which act as markers for degenerative processes that characterise this painful condition.

Another example of the significance of musculoskeletal MRI in the clinical practice is in the diagnosis of muscular distrophies. These disorders are characterised by progressive fat replacement of the muscle tissues. While qualitative MRI can be used as a initial tool to asses muscular distrophies (Marden et al., 2005), qMRI has the advantage to provide precise quantification of the fat fraction in the muscle tissue, thus allowing non-invasive measurement of the disease progression and treatment response (Burakiewicz et al., 2017). QMRI has also been shown to be able to detect very early signs of the disease - even before they become apparent on qualitative images (Wokke et al., 2013) - and is the preferred methods in the analysis of distrophies that affect deep muscle layers (Janssen et al., 2014).

3.3 History of the project

The Medical Physics group at the University Hospital Jena (IDIR) has a long-established track record of developing and pioneering quantitative methods for biomedical applications (Haacke et al., 2004; Schweser et al., 2011; Reichenbach et al., 2015). Another research focus of the Medical Physics group is: radial, non cartesian MRI sequences for characterisation of different tissues. This lead to the development of UTE sequences (Herrmann et al., 2016), paving the way for investigating and quantifying MRI parameters in tendons, which had only rarely been imaged before due to their fast-decaying signal that is very difficult to record with conventional MRI sequences.

MRI has widely been used to characterise the skeletal muscle response to exercise, and retrieve muscle activation patterns. While studies have focused mostly on the calf (Varghese et al., 2015) and hamstring (Mendez-Villanueva et al., 2016), the Medical physics group's contribution has demonstrated significant changes of qMRI parameters, specifically in the less researched area of the lumbar spinal muscles, immediately after a training session (Hiepe et al., 2012; Hiepe et al., 2014). Moreover, (Green and Wilson, 2000) have reported that the values of those parameters are differently affected depending on the degree of training of the subjects. However, little is known regarding whether differences in baseline MRI quantitative parameters are distinguishable at rest among differently trained cohorts. Some preclinical results (Lyu et al., 2021) hint at exercise-induced muscle damage (and subsequent inflammation) being responsible for different baseline values, even at rest, for differently trained groups. But only very recently a study has explored this aspect in vivo for muscles of the leg (Keller et al., 2020).

3.4 Fundamentals of MRI physics

In the next sections, the fundamentals of MRI physics and the most important quantitative MRI parameters will be briefly introduced. A more comprehensive introduction to the physics of MRI is available in the book (Haacke, 1999).

Origin of the MR signal

MR imaging relies on the physical phenomenon of nuclear magnetic resonance (NMR), which arises from the intrinsic magnetic moment of nuclei with a spin angular momentum (Bloch, 1946; Purcell et al., 1946). Spin is a quantum property, conventionally denoted by the letter I. Only nuclei with non-zero I are relevant for NMR, because they possess a nuclear magnetic dipole moment $\vec{\mu}$:

$$\vec{\mu} = \gamma \hbar \vec{I} \tag{3.1}$$

where $\hbar$=$\frac{h}{2\pi}$ is the reduced Planck's constant and γ is the gyromagnetic ratio. The nuclei imaged in MRI are mostly hydrogen protons, because of their abundance in the human body, found both in water (H_2O) and lipid molecules (the latter containing long CH_2 chains). In the presence of an external magnetic field $\vec{B}$, the potential energy E of a magnetic moment can be expressed as:

$$E = -\vec{\mu}\vec{B}. \tag{3.2}$$

For a spin I, the direction of the angular momentum is quantized, resulting in $2I + 1$ possible orientations. For the ^1H nucleus (with spin of $1/2$) there are two available states in the presence of an external static magnetic field $\vec{B}$, oriented along the z direction (B=$B_0\,\hat{z}$). These two states are: a high energy state $|-1/2>$ (anti parallel to B_0) and a low energy state $|+1/2>$ (parallel to B_0). The energy gap between these two states is:

$$\Delta E = \Delta E_{-1/2} - \Delta E_{+1/2} = \hbar\gamma B_0. \tag{3.3}$$

In order to transition between these two states an energy transfer is required, as follows:

$$\Delta E = \hbar\omega_0 \tag{3.4}$$

where ω_0 is the resonance frequency. The combination of the last two equations 3.3 and 3.4 leads to the Larmor equation:

$$\omega_0 = \gamma B_0 \tag{3.5}$$

the equation above highlights the condition between the resonance frequency and the field strength of the external magnetic field. Furthermore, when transitioning from a single spin to an ensemble, as is the case in a sample, we can define $\vec{M}$ as the net (macroscopic) magnetisation that arises as a consequence of the superposition of the magnetic moments of many spins. If the lattice (i.e. the surroundings) is at equilibrium (in the presence of an external magnetic field), there is a nearly equal probability for the jump between the two available energy states, which results in a dynamic balance of the number of spins that populate the energy states, with a slightly higher amount of spins in the low energy state according to the Boltzmann distribution. At equilibrium, the net magnetisation $\vec{M}$ has only a longitudinal non zero component, M_0, which is aligned with $\vec{B}$.

RF excitation

In order to generate a MR signal, the net magnetisation needs to be tipped away from equilibrium (by a flip angle α), this is achieved through the application of an oscillating magnetic field $\vec{B_1}$, perpendicular to $\vec{B}$ (Figure 3.2). $\vec{B_1}$ needs to match the Larmor frequency in order to be able to tip away the net magnetisation. In MRI, for protons and typical clinical field strengths, this matching condition lies in the radio frequency (RF) range, so the $\vec{B_1}$ field is

also referred to as RF pulse. The application of the RF pulse causes more spins to absorb the energy required to jump to the higher energy state and exerts a torque on the net magnetization $\vec{M}$ causing it to spiral away from the longitudinal direction. For this reason it is useful to break down the magnetisation vector in its longitudinal and transverse components as shown in Figure 3.2. The precession of $\vec{M}$ produces a magnetic field oscillating with the Larmor frequency, that, in turn, induces an alternating electric voltage in the receiver coil, allowing detection of a signal.

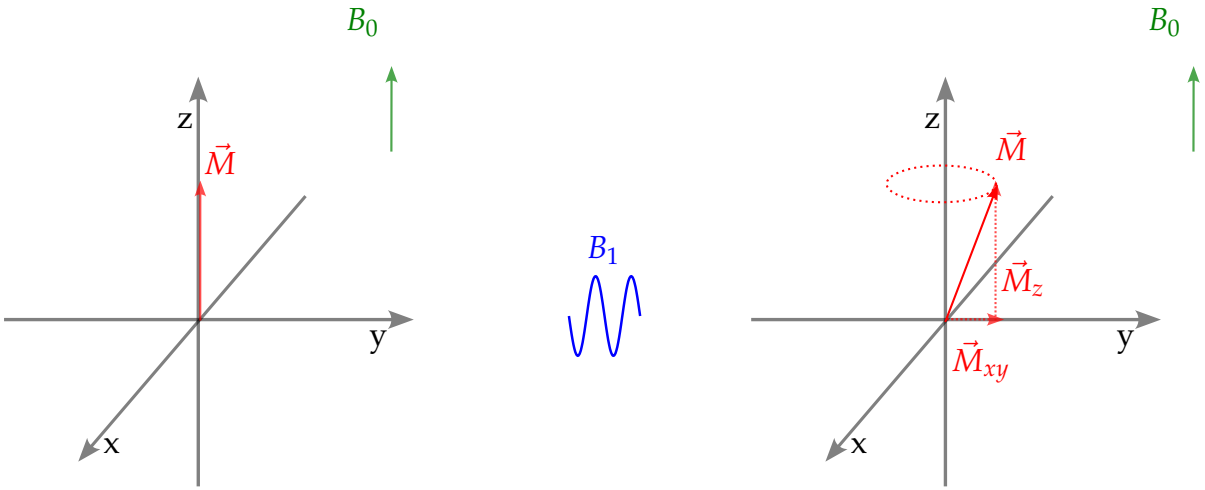

FIGURE 3.2: Illustration of the magnetization vector $\vec{M}$ before and after the application of a rotating field of magnitude B_1, which tilts $\vec{M}$ away from the z axis. The transverse and longitudinal components (M_{xy} and M_z) of the net magnetisation are also shown.

After the RF pulse is turned off, the spins start to return to their equilibrium state (aligned with the external static field) from the higher energy level to the lower. The evolution of the net magnetisation in time (after the application of the RF pulse) is phenomenologically described by the Bloch equations (Bloch, 1946):

$$\frac{dM_x}{dt} = \omega_0 M_y - \frac{M_x}{T_2} \tag{3.6a}$$

$$\frac{dM_y}{dt} = -\omega_0 M_x - \frac{M_y}{T_2} \tag{3.6b}$$

$$\frac{dM_z}{dt} = \frac{(M_0 - M_z)}{T_1} \tag{3.6c}$$

where T_1 and T_2 are the longitudinal and transverse relaxation rates, respectively.

3.5 Relaxation and relaxation constants

T_1 and T_2 are considered fundamental MRI parameters: T_1 also known as the spin-lattice relaxation, T_2 also known as the spin-spin relaxation.

Longitudinal relaxation parameter: T_1

The dynamics of the longitudinal magnetization $M_z(t)$ towards recovery to the initial value M_0 at thermal equilibrium in the presence of B_0 is described by equation 3.6c, (as illustrated in Figure 3.3). The solution of the differential equation 3.6c after an RF pulse is:

$$M_z(t) = M_0 + (M_z(0) - M_0)e^{-\frac{t}{T_1}}. \tag{3.7}$$

When spins in the high-energy state return to the low-energy state, they release energy to the surrounding lattice. T_1 is the time needed after an RF pulse for the longitudinal magnetization to recover 63% of its initial equilibrium magnetization. Different tissues, characterised by different microstructural surroundings, have different T_1 relaxation times.

Transverse relaxation parameter: T_2

Immediately after the RF pulse, the transverse component of the magnetisation M_{xy} has its maximum value. However, each spin is exposed to an effective magnetic field composed by the external magnetic field B_0 and the local fields created by the magnetic moments of neighbouring atoms. Thus, rather than precessing at a singular resonance frequency, the spins in the sample precess at slightly different frequencies, resulting in loss of phase coherence. This, in turn, leads to dephasing and a decrease of the M_{xy} transverse magnetisation (as illustrated in Figure 3.3). For the sake of convenience, we define a rotating frame with the direction of the constant magnetic field $\vec{B}$ as rotation axis and the Larmor frequency (ω_0) as the rotation frequency, the evolution of M_{xy} in time in this rotating reference system can be described as:

$$\frac{dM_{xy}}{dt} = -\frac{M_{xy}}{T_2} \tag{3.8}$$

which can be solved as:

$$M_{xy}(t) = M_{xy}(0)e^{-\frac{t}{T_2}}. \tag{3.9}$$

T_2 is the time of the decay of the transverse magnetisation after an RF pulse when 37% of the initial transverse magnetization remains. The micro structural characteristics of tissues impact their T_1 and T_2 values. For example cortical bone (a very dense tissue, with minimal water content (Fernández-Seara et al., 2002)) or tendons (highly ordered structures) have lower values of T_1 and T_2 when compared to muscles, which are less homogeneous structures and characterised by higher perfusion values.

Effective transverse relaxation parameter: T_2^*

Another source of transverse magnetisation dephasing are inhomogeneities of the external magnetic field $\vec{B}$. This effect becomes particularly prominent for gradient echo (GRE)

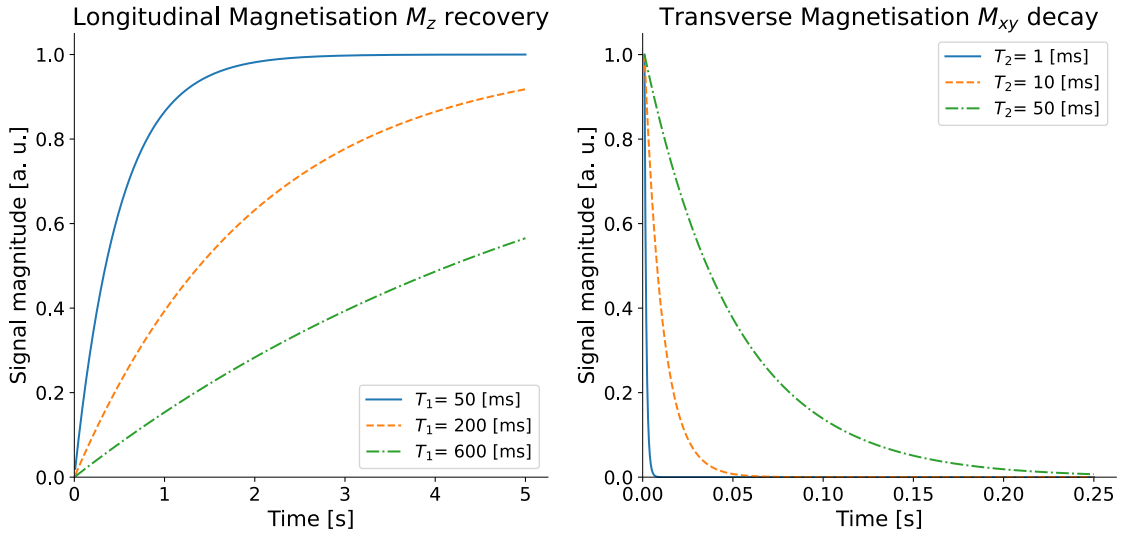

FIGURE 3.3: Magnitude of M_z and M_{xy} during relaxation for different values of the longitudinal relaxation parameter T_1 (left) and of the transverse relaxation parameter T_2 (right). Please note that the reference frame used is the rotating frame.

acquisition (see 3.7) where the residual mesoscopic inhomogeneities are not refocused, differently from a spin echo (SE) acquisition (see 3.7). This additional relaxation sources are characterised by the time constant $T_2{}'$. The effective transverse relaxation time T_2^*, instead, includes all the contributions that decrease the transverse magnetisation. T_2^* can be derived as follows:

$$\frac{1}{T_2^*} = \frac{1}{T_2} + \frac{1}{T_2{}'}. \tag{3.10}$$

For perfectly homogeneous B_0 fields the T_2^* approximates T_2. For any other experiment, the Bloch equations still hold while replacing T_2 with T_2^*.

3.6 From signal to image

In order to correctly localize where the excited spins are spatially located MRI uses additional magnetic field gradients. The gradients alter the main magnetic field linearly along the x, y and z directions and are transiently turned on and off during the imaging process.

$$\vec{G} = (G_x, G_y, G_z) = (\frac{dB_z}{dx}, \frac{dB_z}{dy}, \frac{dB_z}{dz}) \tag{3.11}$$

Under the influence of the gradients, the information encoded in the MR received signal from the sample $S(x, y, z)$ are encoded as spatial frequencies in k-space as follows:

$$s(k_x, k_y, k_z) = \int_x \int_y \int_z S(x, y, z) e^{-i2\pi(k_x x + k_y y + k_z z)} dx dy dz \tag{3.12}$$

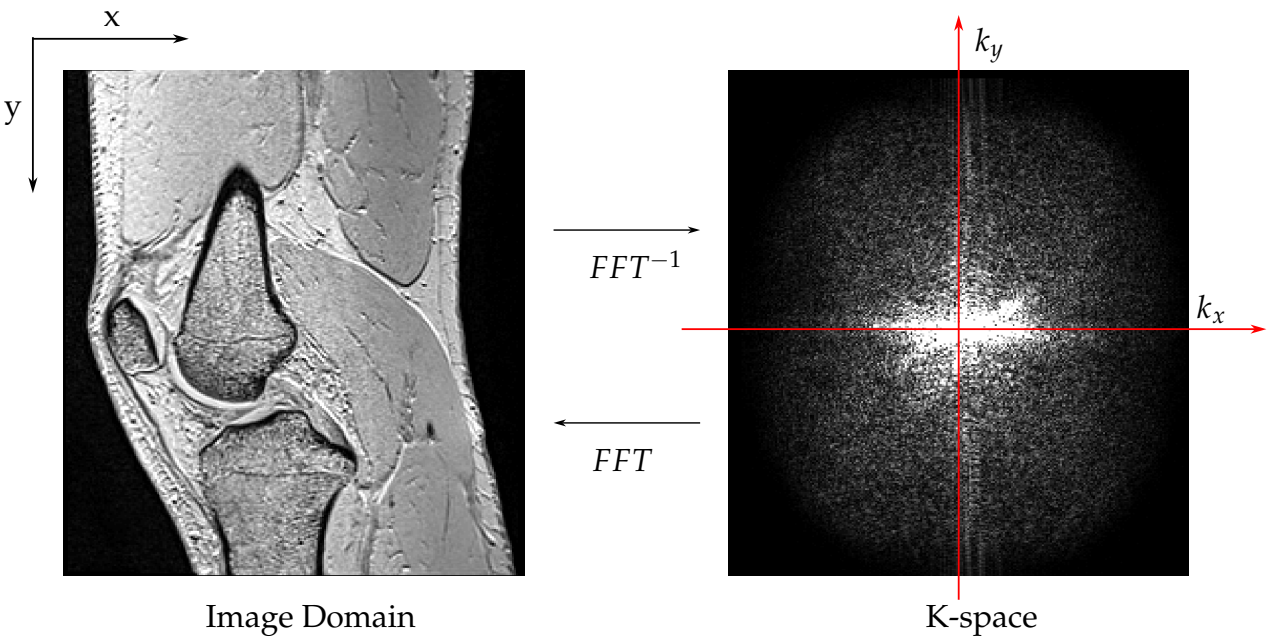

FIGURE 3.4: Magnitude image of a volunteer's knee and corresponding magnitude data in k-space. The application of a Fast Fourier Transform (FFT) enables the conversion between the image domain and k-space and vice versa.

where k_x,k_y,k_z represent the spatial frequencies

$$\begin{aligned} k_x &= \gamma \int_0^t G_x(t)dt \\ k_y &= \gamma \int_0^t G_y(t)dt \\ k_z &= \gamma \int_0^t G_z(t)dt \end{aligned} \tag{3.13}$$

The image of the sample in the spatial domain is obtained applying an inverse Fourier transform to the signal in k-space as shown in Figure 3.4. Many different sampling schemes can be used for filling k-space such as cartesian, spiral and radial (Bernstein et al., 2004).

3.7 Fundamental MRI pulse sequences

In MRI, the term "sequences" refers to a series of RF pulse and magnetic field gradient applications accompanied by specific settings of parameters such as echo time (TE), repetition time (TR) and flip angle (FA) to acquire images with the targeted contrast. Although there is a vast array of different sequences, some common characteristics help distinguish MRI sequences in two main categories. A more comprehensive introduction to the different MRI sequences is available in the book (Bernstein et al., 2004).

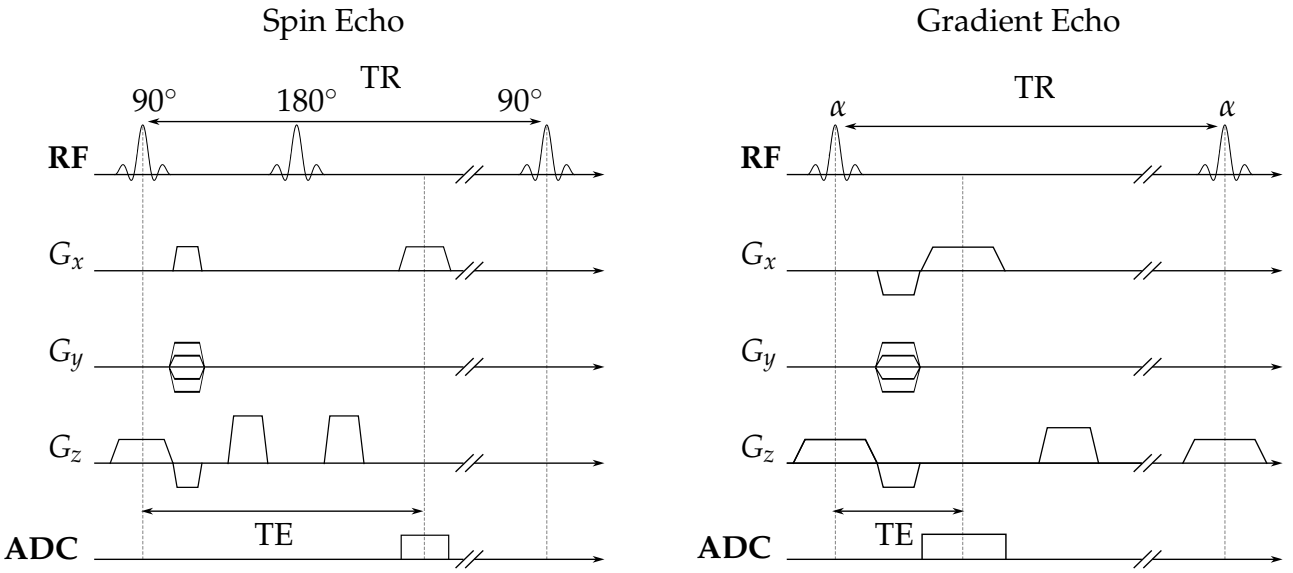

FIGURE 3.5: On the left: sequence diagram of a Spin Echo (SE) sequence; on the right: sequence diagram of a spoiled Gradient Echo sequence (GRE). Note the shorter echo time possible in the GRE sequence, due to the lack of the 180° refocusing pulse. TR is the repetition time, TE stands for the echo time and ADC for the time window in which the signal is recorded. G_x is the read-out gradient while G_y is the phase encoding gradient and G_z is the slice select gradient. The vertical dashed lines serve to emphasize center of the RF pulses or ADC, delineating the TR and TE accordingly.

Spin Echo Imaging Sequences

The signal in SE sequences is produced by pairs of RF pulses. Often, the first is a 90 degree pulse (i.e. a RF pulse with a 90 degree flip angle) followed by a 180 degree refocusing pulse. The second pulse is surrounded by crusher gradients, as shown in Figure 3.5. The first crusher gradient assures that the refocused spins still maintain phase coherence, while the latter spoils any undesired new signal contributions from spins that might have moved into or out of the slice selected with G_z due to physiological motions.

spoiled Gradient Echo Imaging Sequences

GRE sequences, differently than SE sequences, are characterised by a single radio frequency pulse, per k-space line, thus allowing for shorter echo times, and are often applied with low flip angles and short TRs. This regime is also called Fast Low Angle SHot (FLASH). In spoiled GRE sequences, dephasing effects resulting from magnetic field inhomogeneities are not eliminated as they would be with a SE sequence. Furthermore, spoiler gradients and the introduction of a carefully selected RF phase offset between two consecutive repetitions are used to avoid the signal of the current repetition to be affected by remnants of the transverse magnetisation from previous repetitions (Zur et al., 1991). FLASH sequences are GRE imaging sequences that allow for a significant reduction of the measurement time (Haase et al.,

1986). The FLASH equation (which describes the steady state signal under FLASH conditions) can be derived starting from equation 3.7, which provides the time dependent signal of $M_z(t)$ after an RF pulse. If RF pulses are applied sufficiently quickly: the magnetization does not recover fully between pulses and develops a steady-state magnetisation M_{ss} that is distinct from M_0. After n RF pulses (played out every TR), the longitudinal magnetization can be expressed as:

$$M_z(t_{TR+1}) = M_z(t_{TR})e^{-\frac{TR}{T_1}}\cos(\alpha) + M_0(1 - e^{-\frac{TR}{T_1}}) \tag{3.14}$$

when a steady state for the longitudinal magnetisation is reached $M_z(t_{TR}) = M_z(t_{TR+1}) = M_{ss}$, yielding:

$$M_{ss} = \frac{M_0(1 - e^{-\frac{TR}{T_1}})}{1 - \cos(\alpha)e^{-\frac{TR}{T_1}}} \tag{3.15}$$

$$M_{xy} = M_{ss}\sin(\alpha) = \frac{M_0(1 - e^{-\frac{TR}{T_1}})}{1 - \cos(\alpha)e^{-\frac{TR}{T_1}}}\sin(\alpha). \tag{3.16}$$

Taking into account T_2^* relaxation leads to:

$$M_{xy}(t) = M_{ss}\sin(\alpha) = \frac{M_0(1 - e^{-\frac{TR}{T_1}})}{1 - \cos(\alpha)e^{-\frac{TR}{T_1}}}\sin(\alpha)e^{-\frac{TE}{T_2^*}}. \tag{3.17}$$

T_2^* and T_1 maps can be obtained by acquiring several dataset with varying values of the echo time (for T_2^*) or repetition time (TR) or the flip angle (α) and fitting the acquired data in a non-linear fashion voxel-by-voxel with the relevant part of equation 3.17. The two different methods for T_1 quantification are called Variable Repetition Time (VTR) and Variable Flip Angle (VFA), respectively (Christensen et al., 1974).

3.8 Ultrashort Echo Time Sequences

This section provides an introduction of Ultrashort Echo Time sequences as well as their use and differences from standard MRI sequences (Bergin et al., 1991; Tyler et al., 2007; Qian et al., 2012).

The need for UTE sequences arises because the main source of signal collected with standard MRI sequences used daily in the clinical practice, are free or loosely bound water protons. However, it has been estimated that 20 % to 30 % of the hydrogen signal (i.e. signal originating from tightly bound water protons) remains undetected with clinical MRI (Duck, 2013).

As a result, tissues containing high amounts of tightly bound water, as is the case with water bound to collagen fibres (or in cortical bone), are very challenging or nearly impossible to image using standard MRI sequences. The difficulty in imaging tendons lies in the presence of highly ordered collagen fibres, which causes a non isotropic tumbling motion that results in the destruction of the coherent magnetisation due to rapid dephasing, yielding very short values of T_2^*. A comprehensive review of the physical principles of the MRI signals of so-called "short T_2^* tissues" and the sequences used for imaging them is presented in the book (Bydder et al., 2012).

UTE sequences employ extremely short excitation pulses and echo times, thus allowing to capture the signal of short T_2^* tissues. As the name suggest, they are characterised by a short Echo Time (calculated as the time interval from the end of the RF excitation pulse and the beginning of the acquisition) smaller than 1 ms. Both 3D and 2D acquisition schemes are available: a 3D acquisition scheme provides more efficient RF excitation but it requires more acquisition time. On the other hand, a 2D scheme is faster but prone to slice profile inaccuracies (Johnson et al., 2013).

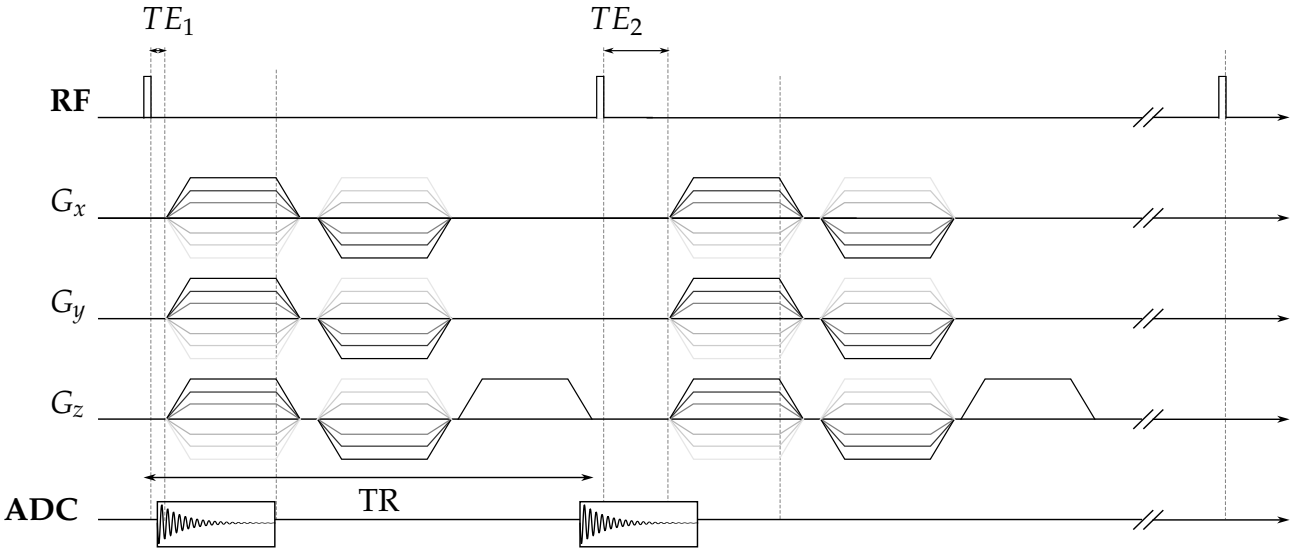

FIGURE 3.6: Sequence diagram of an echo train shifted 3D Ultrashort Echo Time sequence. The 3D radial "spikey ball" sampling scheme is represented by the different shading of the gradient amplitudes.

For the 3D acquisition, the excitation pulse is typically a hard non-selective pulse, followed by 3D encoding gradients. A detailed sequence diagram is shown in Figure 3.6. For 2D acquisition the excitation pulse is typically a half-pulse: i. e. two consecutive excitations with the second one having its gradient polarity reversed. The data from both excitations are then combine to encode a single line in k-space. For both 2D and 3D sequences the acquisition scheme is non-Cartesian. For 3D sequences different approaches ranging from a radial inside out spokes (spikey ball) (Herrmann et al., 2016; Krämer and Maggioni et al., 2019), spiral (Gurney et al., 2006) or stack of stars (Kronthaler et al., 2021) are available. An

additional advantage of the the non-cartesian k-space sampling is the oversampling of the centre of the k-space which increases protection against motion and fold-over artifacts.

3.9 B_1-field mapping and correction

B_1-field mapping refers to the need to appropriately map the spatial distribution of the transmitted RF field, because its inhomogeneities can affect the final quantification of T_1. This section introduces the concept of B_1-field mapping and describes the most commonly used techniques for this application. In the following section, the magnitude of the $\vec{B_1}$ vector field will be indicated as B_1.

These inhomogeneities arise due to interactions between the RF field and the measured subject or sample, and have a much greater effect at higher field strengths ($\geq$ 3T) due to a reduction of the RF wavelength with increasingly larger magnetic field strengths. If the RF wavelength is in the same order of magnitude as the imaged object, constructive or destructive interferences of the transmitted RF field occur in the measured sample (Collins et al., 2005). These interferences lead to spatially varying amplitude and phase of the transverse magnetic field (so called B_1 inhomogeneities) which, in turn, cause spatially varying flip angles, ultimately causing erroneous T_1 parameter estimation and inhomogeneous signal intensity. FLASH sequences in particular are affected by B_1 inhomogeneities (Zelaya et al., 1997; Dietrich et al., 2008) because their T_1-weighting, besides TR, depends on the flip angle, as shown in equation 3.17.

B_1-field mapping sequences can be divided in two main subcategories: phase-based and magnitude-based methods.

Signal phase-based B_1-field mapping

The Bloch-Siegert method (Bloch and Siegert, 1940; Sacolick et al., 2010) is a well known example of a phase-based B_1 mapping method. This approach uses a Gradient Echo (GRE) acquisition with a strong off-resonance pulse after the initial excitation and before acquisition (Figure 3.7): the first RF pulse creates a transverse magnetisation, while the second creates an incremental phase in the transverse magnetisation, which is B_1-dependent.

Conceptually, the resonance frequency of a spin experiences a shift when a strong enough off-resonance RF pulse is applied. This causes the spin to precess at a frequency that depends on the magnitude of B_1 and the difference between the spin resonance and the RF frequency (ω_{RF}). After the application of the off resonance RF pulse the effective B_1 field for an on-resonance spin is (Sacolick et al., 2010):

$$\gamma B_1^{eff} = \sqrt{\omega_{RF}(t)^2 + (\gamma B_1(t)^2)}. \tag{3.18}$$

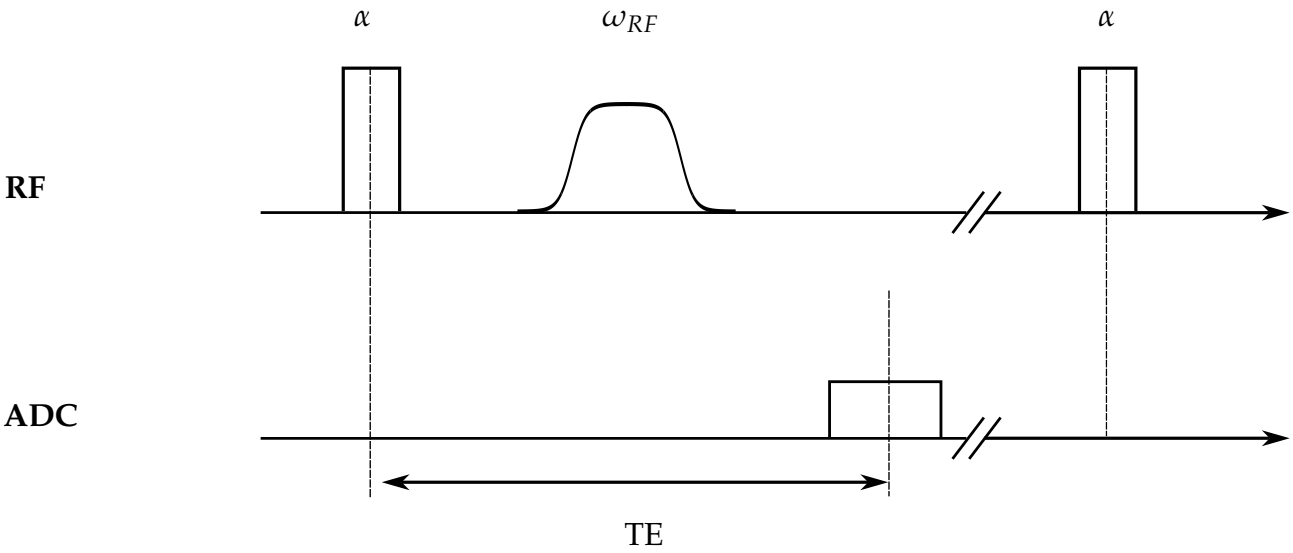

FIGURE 3.7: Bloch-Siegert sequence diagram, note the off resonance (Fermi) pulse (ω_{RF}) after the initial RF excitation, which encodes the B_1 inhomogeneities into the phase of the signal. However, the additional pulse results in a long echo time (TE) before acquisition. Note that no spatial encoding is shown in this sequence diagram.

Please note that equation 3.18 is given in the rotating frame of the RF pulse. If the applied pulse is strongly off-resonance, we can assume $\omega_{RF} >> \gamma B_1$, thus leading to the approximation of 3.18 as:

$$\gamma B_1^{eff} \approx \omega_{RF}(t) + \omega_{BS}(t) \tag{3.19}$$

where $\omega_{BS}=\frac{(\gamma B_1)^2}{2\omega_{RF}}$ is the small off-resonant contribution along the direction of B_1^{eff}. The effective frequency due to the Bloch-Siegert phenomenon causes spins to accumulate a phase as:

$$\phi_{BS} = \int_o^\tau \omega_{BS}(t)\, dt \tag{3.20}$$

where τ is the duration of the off-resonance pulse. The expected phase shift can be calculated from 3.20 for any pulse $B_1(t)$ with frequency offset ω_{RF}. Undesired phase sources are removed by taking the phase difference between two images acquired one with the off-resonance frequency of the Bloch Siegert pulse set to ω_{RF} and one with -ω_{RF}.

Signal magnitude-based B_1-field mapping

In contrast to the Bloch-Siegert method, the Actual Flip Angle Imaging method (AFI) is a signal magnitude-based B_1-field mapping technique (Yarnykh, 2007). This method employs a dual steady state acquisition characterised by two interleaved TRs, where the B_1 map can be calculated by the ratio of the two signals.

As illustrated in Figure 3.8, the acquisition is GRE with RF pulses of flip angle α separated by interleaved TRs: TR_1 and TR_2. Similar to many GRE sequences, the underlying assumption is that: after a number of sequence repetitions, the magnetisation reaches a steady state.

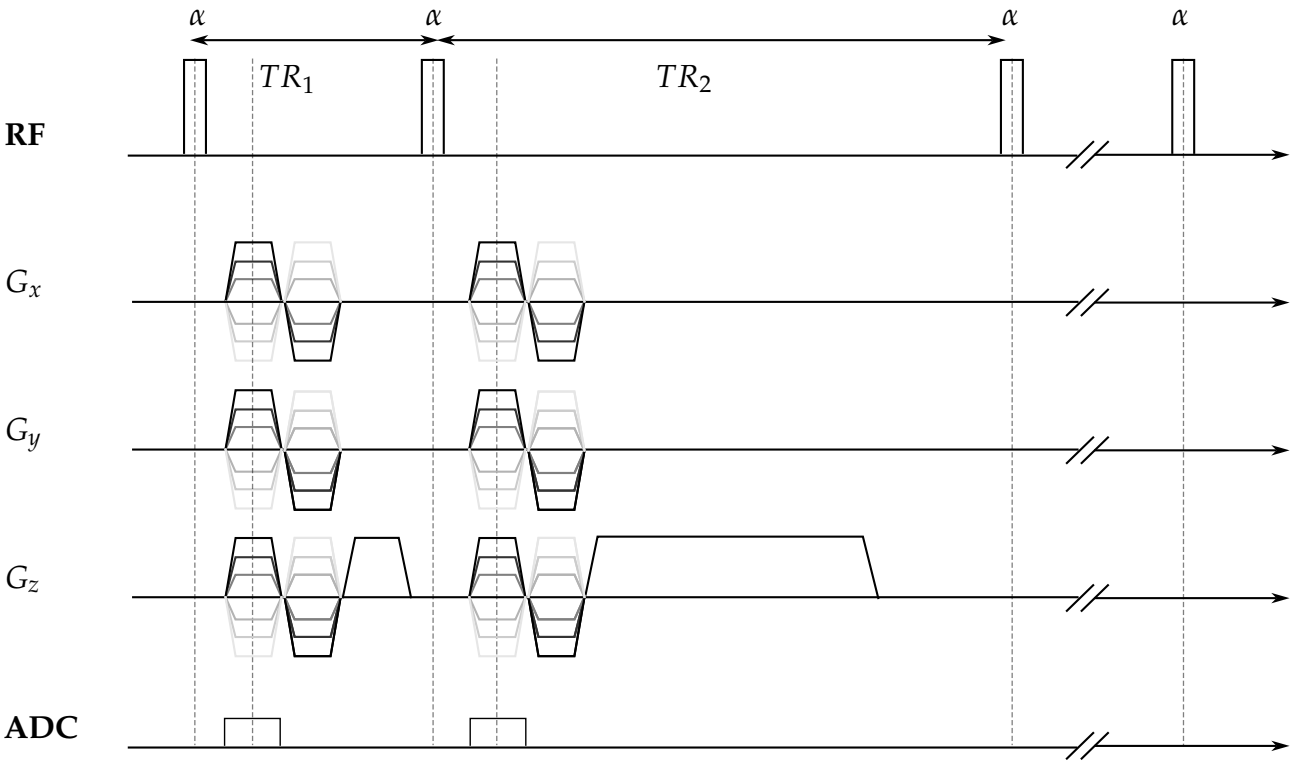

FIGURE 3.8: AFI sequence diagram with interleaved RF pulses, all with the same flip angle α, characterised by two different repetition times T_1 and T_2. Note the large gradient spoiler along the z direction necessary to achieve "perfect spoiling" conditions.

However, the distinctive aspect of the AFI method is the use of a pulsed steady-state signal acquisition (Nehrke, 2009), where both TR_1 and TR_2 are shorter than T_1. This approach circumvents the limitation present in prior methods that required prolonged relaxation delays between sequence repetitions.

Under the assumption of ideal spoiling, a consecutive solution of the Bloch equations results in expressions for the longitudinal components of the magnetisation (Yarnykh, 2007):

$$\begin{aligned} M_{z1} &= M_0 \frac{1 - E_2 + (1 - E_1)E_2 \cos\alpha}{1 - E_1 E_2 \cos^2\alpha} \\ M_{z2} &= M_0 \frac{1 - E_1 + (1 - E_2)E_1 \cos\alpha}{1 - E_1 E_2 \cos^2\alpha} \end{aligned} \tag{3.21}$$

where $E_i{=}e^{(-\frac{TR_i}{T_1})}$. After a RF pulse, the received signal is:

$$S_i = M_{z,i} e^{(-\frac{TR_i}{T_2})} \sin\alpha. \tag{3.22}$$

Assuming that $TR_i \gg T_1$ and applying first order approximation, it follows:

$$E_i = e^{(-\frac{TR_i}{T_1})} \approx 1 - \frac{TR_i}{T_1}. \tag{3.23}$$

Inserting 3.23 in 3.22 and taking the ratio of S_1 and S_2 leads to:

$$r = \frac{S_2}{S_1} \approx \frac{1 + n\cos\alpha}{n + \cos\alpha}, \tag{3.24}$$

where n=$\frac{TR_2}{TR_1}$. Which allows to calculated the actual flip angle (α) as follows:

$$\alpha \sim \arccos\frac{rn - 1}{n - r}. \tag{3.25}$$

The GRE acquisition of the AFI method makes it compatible with UTE sequences, but its effectiveness fully depends on achieving "perfect spoiling" conditions, which (in the current implementations) results in extremely long acquisition times. Furthermore, the method provides limited accuracy for tissues with very short T_1.

3.10 Diffusion and fat-water signal separation

In this section the fundamentals of two additional quantitative MRI parameters will be explored. These parameters are diffusion and fat-water quantification, which have a variety of uses in MRI but are of particular interest for the quantification of parameters in muscles as they can indirectly provide informations about muscles' composition and structure. This is due to the fact that the values of these quantitative parameters are influenced by factors such as muscle fibres' size, orientation and composition.

Diffusion Weighted Imaging

Diffusion is defined as the stochastic motion of molecules or atoms in fluids or gases as a consequence of random movements due to thermal energy, T. According to the Einstein-Stokes equation (Einstein, 1905) the diffusion coefficient (which is a measure of the mobility of a particle in a medium) can be expressed as:

$$D = \frac{k_B T}{6\pi\eta r} \tag{3.26}$$

where k_B is the Boltzmann constant, η the viscosity of the medium and r the radius of the particle. Diffusion can be investigated by diffusion sensitized MRI sequences, where D can be extracted by taking into account the signal attenuation caused by diffusion. After the application of a 90 degree RF pulse the water protons start to dephase as described in section

3.5. If a subsequent 180 degree pulse is applied, in the absence of diffusion, it would re-establish phase coherence resulting in maximum signal intensity. However, in the presence of diffusion, the protons will have moved, experiencing slightly different local fields during dephasing than during rephasing. This discrepancy leads to a signal decay as follows (Stejskal and Tanner, 1965):

$$S(g) = S_0 e^{(-D\gamma^2 g^2 \delta^2 (\Delta - \frac{\delta}{3}))} \tag{3.27}$$

where g is the amplitude, δ the duration of the gradient and Δ the interval between the first and second diffusion gradient, G_{diff} (as shown in Figure 3.9). Equation 3.27 can be rewritten as:

$$S(b) = S_0 e^{(-bD)} \tag{3.28}$$

where $b = \gamma^2 g^2 \delta^2 (\Delta - \frac{\delta}{3})$ represents the so-called b-value: it stands for the strength of the diffusion weighting, created by the diffusion gradients. By acquiring multiple images with varying b-values, and fitting the data to 3.28, the value of the diffusion coefficient D, in a given tissue, can be estimated and parametric maps can be computed enabling quantitative assessment of the diffusion values (Portakal et al., 2018).

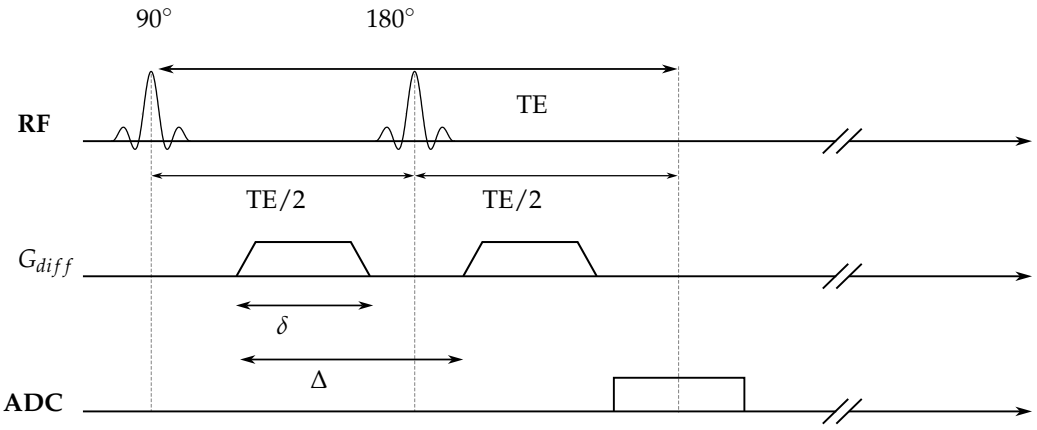

FIGURE 3.9: Pulse Gradient Spin Echo (PGSE) sequences. The phases of stationary spins are unaffected by the diffusion gradients (G_{diff}), in contrast the diffusing spins experience a mismatch between the phases acquired during each gradient pulse, leading to a loss of coherence and diffusion dependent signal attenuation.

Thus far, only isotropic diffusion has been considered, yielding a scalar value of the diffusion coefficient. However, in biological tissues the diffusion of free water molecules is hindered by the presence of macromolecules, fibres, cell membranes and other sub cellular structures. For this reason, it is beneficial to introduce the concept of the Apparent Diffusion Coefficient (ADC). Typically smaller than the value of the self diffusion coefficient D, the ADC accounts for these obstructions.

Moreover, in biological samples, the aforementioned constraints on the water molecule movement tend to lack spherical symmetry. Instead, they exhibit a preferred direction along

which the diffusion coefficients are significantly higher compared to the other directions. Which leads to the expression of D as tensor to account for different diffusion coefficients along different directions.

$$D = \begin{bmatrix} D_{xx} & D_{xy} & D_{xz} \\ D_{xy} & D_{yy} & D_{yz} \\ D_{xz} & D_{yz} & D_{zz} \end{bmatrix} \tag{3.29}$$

Intra Voxel Incoherent Motion (IVIM) (Le Bihan et al., 1988; Le Bihan, 2019) is an extension of diffusion MRI, which allows differentiation between free water diffusion and perfusion-related signal attenuation due to blood circulation in capillaries. This differentiation provides additional insights into the micro circulation of the investigated tissues and can be beneficial for the characterisation of healthy tissue such as muscle (Filli et al., 2015) as well as to highlight a pathological state. A comprehensive review of IVIM for skeletal muscle analysis is presented by (Englund et al., 2022). The signal decay in IVIM can be described by (Le Bihan et al., 1988):

$$S = S_0(fe^{-b(D+D^*)}) + (1-f)e^{-bD}) \tag{3.30}$$

where D^* is the additional attenuation coefficient as a consequence of perfusion and f is the perfusion fraction (i.e. the fraction of the signal originating from protons in blood vessels).

Fat-water signal separation

The chemical shift phenomenon describes a small shift in the resonance frequency of a proton due to its partial shielding from the external magnetic field by the surrounding electron cloud. For instance, a proton within a lipid molecule (characterised by long hydrocarbon chains) feels a slightly weaker magnetic field than a proton in a water molecule. For a field strength of 3T this corresponds to a shift in the resonance frequency of about 428 Hz, which causes water and fat protons to precess at slightly different frequencies. The resonance frequency shift causes the magnetisation vectors of water and fat protons to be aligned (or in phase) or anti-aligned (or out of phase) depending on how much time has passed since the RF excitation (see Figure 3.10).

By acquiring images at different echo times (both in phase and out of phase) and linearly combining them it is possible to generate separate water (S_w) and fat (S_f) images and calculate the percentage of fat in the investigated tissues as follows (Ma, 2008):

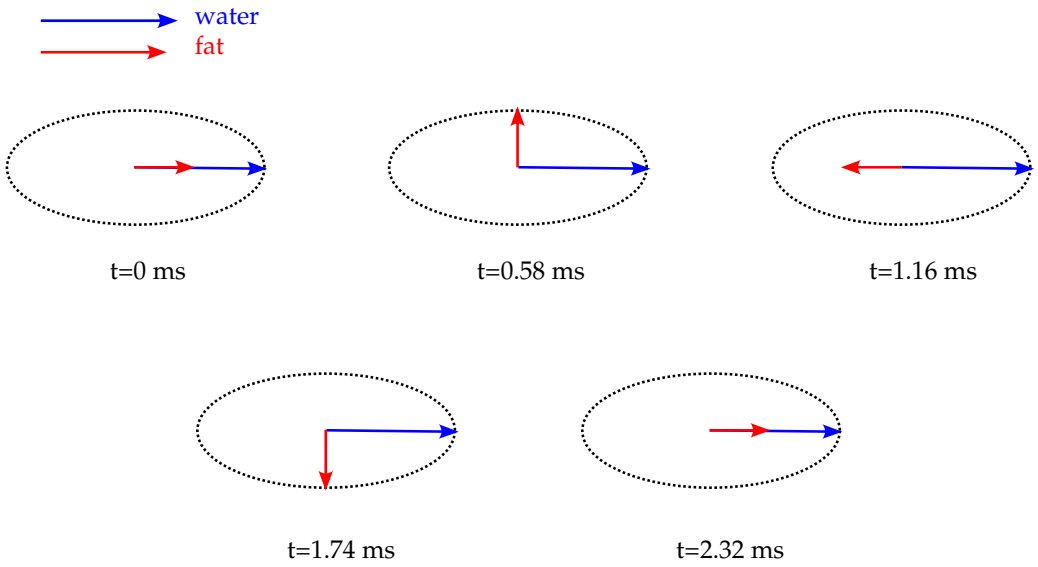

FIGURE 3.10: Behaviour of the water and fat magnetisation vectors after a RF pulse. Immediately after the RF pulse the two vectors are in phase, since the water protons are less shielded than the lipid protons, they process slightly faster, leading to both destructive (circa 1.16 ms after the pulse) and constructive interferences.

$$S_F = \frac{S_{\text{in phase}} - S_{\text{out of phase}}}{2}$$
$$S_W = \frac{S_{\text{in phase}} + S_{\text{out of phase}}}{2} \tag{3.31}$$

This method of fat-water signal separation is called Dixon method (Dixon, 1984), and is widely applied for musculoskeletal applications due to its robustness and the ability to be combined with both GRE and SE acquisitions (Lins et al., 2020). However, it is important to point out that this method is sensible to B_0 field inhomogeneities, which could lead to incorrect quantification of fat for some voxels.

4. Objectives of the work

The primary goal of this work was to evaluate and optimise quantitative MRI techniques for less well researched areas of the musculoskeletal system. The applications of these techniques were in two distinct areas: the tendons of the knee and lumbar back muscles, each posing unique challenges due to their microstructural characteristics.

The knee application focused on quantitative methods in previously scarcely imaged and highly ordered collagen rich areas, such as tendons of the knee. These tissues, traditionally, are known to be difficult to image with conventional MRI due to their fast decaying signal. The goal was to assess the feasibility of employing UTE sequences (Qian et al., 2012) to enable quantitative T_1 and T_2^* analysis in these tissues. Given the difficulties in imaging of tendons there is a scarcity of literature available for comparison and testing the robustness of accurate quantification (Kijowski et al., 2017; Ma et al., 2019). The strategy to address this gap included using values in other (better researched) areas for indirect validation and employing two different methods to measure the values of T_1, and compare their results.

The lumbar back muscle pilot study aimed at developing a protocol to investigate whether physiological adaptations caused by different training routines are reflected in changes of MR quantitative parameters. While these differences have been previously detected with a variety of invasive (such as biopsies (Flück et al., 2019)) and non invasive (such as electromyography (Schönau and Anders, 2023)) methods, incorporating an imaging approach would aid in the understanding of such physiological adaptations. The pilot study's focus was on potential differences at rest, stemming from long-term sports practice, contrasting with the immediate consequence of an exercise intervention most commonly investigated in literature. For this purpose, a multi parametric protocol was developed, expanding upon the parameters used in the knee application, to investigate which quantitative parameters were more sensitive to these changes and could be used to help interpret changes in healthy muscle tissues.

One common challenge in the first two objectives is accurate quantification of T_1 in the presence of B_1 inhomogeneities. To address this issue, B_1 correction is necessary. Therefore, an overarching goal is to implement B_1 correction methods with existing state of the art techniques (Sacolick et al., 2010), wherever feasible, while also proposing optimised methods addressing the unique challenges of B_1 mapping with UTE acquisition. In conclusion, the goals of this work were to evaluate state of the art quantitative MRI methods, demonstrate the feasibility of the use of such methods in short T_2^* tissues and develop optimizations where necessary, to provide insights in different tissues of the musculoskeletal system.

5. Manuscripts

5.1 T_1 and T_2* mapping of the human quadriceps and patellar tendons using ultra-short echo-time (UTE) imaging and bivariate relaxation parameter- based volumetric visualization

Authors: M. Krämer[1], M.B. Maggioni[1], N.M. Brisson, S. Zachow, U. Teichgräber, G.N. Duda, J.R. Reichenbach

[1] the two authors contributed equally

Magnetic Resonance Imaging 63 (2019) 29–36

Contents lists available at ScienceDirect

Magnetic Resonance Imaging

journal homepage: www.elsevier.com/locate/mri

Original contribution

T_1 and T_2^* mapping of the human quadriceps and patellar tendons using ultra-short echo-time (UTE) imaging and bivariate relaxation parameter-based volumetric visualization

M. Krämer[a,*,1], M.B. Maggioni[a,1], N.M. Brisson[b], S. Zachow[c], U. Teichgräber[d], G.N. Duda[b], J.R. Reichenbach[a]

[a] Medical Physics Group, Institute of Diagnostic and Interventional Radiology, Jena University Hospital, Friedrich Schiller University Jena, Germany
[b] Julius Wolff Institute and Center for Musculoskeletal Surgery, Charité – Universitätsmedizin Berlin, Germany
[c] Zuse Institute Berlin, Germany
[d] Institute of Diagnostic and Interventional Radiology, Jena University Hospital, Friedrich Schiller University Jena, Germany

ARTICLE INFO

Keywords:
UTE
Tendons
Patellar ligament
Segmentation
3D visualization

ABSTRACT

Quantification of magnetic resonance (MR)-based relaxation parameters of tendons and ligaments is challenging due to their very short transverse relaxation times, requiring application of ultra-short echo-time (UTE) imaging sequences. We quantify both T_1 and T_2^* in the quadriceps and patellar tendons of healthy volunteers at a field strength of 3 T and visualize the results based on 3D segmentation by using bivariate histogram analysis. We applied a 3D ultra-short echo-time imaging sequence with either variable repetition times (VTR) or variable flip angles (VFA) for T_1 quantification in combination with multi-echo acquisition for extracting T_2^*. The values of both relaxation parameters were subsequently binned for bivariate histogram analysis and corresponding cluster identification, which were subsequently visualized. Based on manually-drawn regions of interest in the tendons on the relaxation parameter maps, T_1 and T_2^* boundaries were selected in the bivariate histogram to segment the quadriceps and patellar tendons and visualize the relaxation times by 3D volumetric rendering. Segmentation of bone marrow, fat, muscle and tendons was successfully performed based on the bivariate histogram analysis. Based on the segmentation results mean T_2^* relaxation times, over the entire tendon volumes averaged over all subjects, were 1.8 ms ± 0.1 ms and 1.4 ms ± 0.2 ms for the patellar and quadriceps tendons, respectively. The mean T_1 value of the patellar tendon, averaged over all subjects, was 527 ms ± 42 ms and 476 ms ± 40 ms for the VFA and VTR acquisitions, respectively. The quadriceps tendon had higher mean T_1 values of 662 ms ± 97 ms (VFA method) and 637 ms ± 40 ms (VTR method) compared to the patellar tendon. 3D volumetric visualization of the relaxation times revealed that T_1 values are not constant over the volume of both tendons, but vary locally. This work provided additional data to build upon the scarce literature available on relaxation times in the quadriceps and patellar tendons. We were able to segment both tendons and to visualize the relaxation parameter distributions over the entire tendon volumes.

1. Introduction

Patellar tendinopathy often affects athletes of various disciplines and is mainly caused by tendon overuse, although the origin of the pathology is still incompletely understood [1]. Thus, insight into the MR relaxation properties of tendons and ligaments may be highly valuable to detect and potentially understand possible pathological developments due to the intricate interplay between water molecules and tendon tissue [2]. Conventional MR imaging protocols commonly applied in clinical practice are typically only able to detect later stages of the diseases, as direct imaging of ligaments and tendons by means of magnetic resonance imaging (MRI) is challenging due to the short T_2^* relaxation times in compact tissues, typically ranging between 0.5 ms and 2.5 ms [3–6]. With such fast decaying transverse magnetizations,

* Corresponding author at: Medical Physics Group, IDIR, Jena University Hospital, Philosophenweg 3, D-07443 Jena, Germany.
E-mail addresses: martinkraemer84@gmail.com (M. Krämer), marta.maggioni@uni-jena.de (M.B. Maggioni), nicholas.brisson@charite.de (N.M. Brisson), zachow@zib.de (S. Zachow), ulf.teichgraeber@med.uni-jena.de (U. Teichgräber), georg.duda@charite.de (G.N. Duda), Juergen.Reichenbach@med.uni-jena.de (J.R. Reichenbach).
[1] Both authors contributed equally.

https://doi.org/10.1016/j.mri.2019.07.015
Received 11 April 2019; Received in revised form 8 July 2019; Accepted 23 July 2019

tendons and ligaments appear characteristically black with no measurable signal on the images when data are acquired with conventional MRI sequences. However, with recent advances in ultra-short echo-time (UTE) imaging sequences, direct imaging of tendons has become possible, offering the possibility to quantify their relaxation parameters. Typically, UTE imaging sequences use 2D half pulses [7,8] or non-selective short rectangular radiofrequency (rf) pulses [9–12] for excitation to achieve echo times (TE) below 1 ms. With the introduction of UTE sequences, interest in the quantitative analysis of tendons tissues has been steadily increasing. Previous studies have demonstrated relevant changes in the T_2^* relaxation time as a consequence of loading [13], disease (e.g., diagnosed patellar tendinopathy [6]) and physical activity [14]. While the relevance of identifying changes of T_1 [5] is currently still under discussion, this work nevertheless explores the possibility of creating a single imaging protocol to quantify both parameters, T_2^* and T_1.

Various methods have been proposed to quantify T_1 relaxation time constants. Most methods combine an inversion pulse with fast low-angle shot (FLASH) or spin-echo based acquisition modules [15–17]. With UTE imaging, however, applying any spin-echo based technique in tissues with very short T_2/T_2^* relaxation times is challenging because the necessary time span between excitation and formation of a spin-echo initiated by the refocusing rf-pulse is usually too long. Furthermore, combining 3D-UTE imaging with hard pulse excitation, as used in this study, with an inversion pulse is not convenient because truly inverting short T_2^* components is challenging and total acquisition time would be considerably increased. For these reasons, estimation of T_1 with UTE sequences typically applies either the variable flip angle (VFA) [18,19] or the variable repetition time (VTR) [20] technique. Both methods exploit the fact that the steady state magnetization of a gradient-echo FLASH based UTE sequence can be deliberately modified by changing either the acquisition flip angle or the repetition time (TR).

So far, quantification of relaxation parameters in ligaments and tendons has focused mostly on the Achilles tendon [3,4,21–23], while only few studies have focused on tendons of the knee [6,24]. It was thus the aim of this work to apply isotropic, 3D, multi-echo UTE imaging with both VFA and VTR techniques to estimate T_1 in the patellar and quadriceps tendons and to compare the extracted values between the two methods. Implementing the sequence as a multi-echo, gradient-echo sequence enabled us to also extract effective transverse relaxation times T_2^*. Due to the isotropic spatial resolution, 3D visualization of the relaxation time parameters of the patellar and quadriceps tendons was facilitated.

2. Material and methods

2.1. T_1 estimation with VFA and VTR

UTE imaging sequences typically use gradient-echo based, FLASH-type, acquisition schemes with short repetition times in combination with low flip-angles for fast acquisition. The equilibrium signal in such sequences is given by:

$$S = M_0 \sin(\alpha)\frac{1 - exp(-TR/T_1)}{1 - exp(-TR/T_1)\cdot cos(\alpha)}\cdot \exp(-TE/T_2^*) \quad (1)$$

with initial magnetization M_0, flip angle α, repetition time TR and echo-time TE. While the three parameters T_1, T_2^*, and M_0 in Eq. (1) are object-specific, the three parameters, TR, TE and α, can be controlled directly via the imaging sequence parameter settings. Considering only data acquired at a particular echo time removes the dependency from T_2^* as a fit parameter and reduces Eq. (1) to an equation containing only two parameters, p_0 and T_1:

$$S(\alpha, TR) = p_0 \sin(\alpha)\frac{1 - exp(-TR/T_1)}{1 - exp(-TR/T_1)\cdot cos(\alpha)} \quad (2)$$

where the terms M_0 and $exp(-TE/T_2^*)$ have been merged together into a single fit parameter p_0. Data acquired with a set of different flip angles in case of VFA or a set of different repetition times in case of the VTR method can then be fitted to Eq. (2) for extracting T_1.

2.2. UTE imaging protocol

A radial 3D-UTE sequence with non-selective hard pulse excitation and center-out spikey-ball trajectory was applied [12]. To avoid digital filtering artifacts affecting the first sampling points, the data sampling was switched on 20 µs before ramping-up the gradients. Constant z-spoiling was applied at the end of each repetition in order to spoil residual magnetization. Multi-echo acquisition was performed in a monopolar fashion during one readout train by using rephasing gradients between the echoes.

Measurements were performed on five volunteers aged between 24 and 50 years old (three male and two female) without known pathologies on a 3 T whole-body MRI scanner (Magnetom PRISMA, Siemens Healthineers, Erlangen, Germany) using a 16-channel NORAS Variety flex coil (NORAS MRI products GmbH, Höchberg, Germany). All volunteers gave written informed consent following the guidelines of the institutional ethics committee. Imaging data were acquired with a field-of-view (FoV) of (160 × 123 × 100) mm^3 and an acquisition matrix size of 80 × 61 × 50, resulting in an isotropic spatial resolution of (2.0 × 2.0 × 2.0) mm^3. For each filled *k*-space, a total of 12,590 radial spokes were acquired with a readout bandwidth of 125 kHz. The duration of the rectangular excitation pulse was 150 µs. VTR acquisition was performed using five different repetitions times of 8 ms, 16 ms, 30 ms, 50 ms and 80 ms, and a constant flip angle of 25°. VFA data were acquired with five different flip angles of 5°, 12°, 20°, 30° and 38°, and TR of 20 ms. Both VTR and VFA protocols acquired 3 echoes with echo-times of 0.10 ms, 2.48 ms and 4.90 ms to allow extracting of T_2^*. The total acquisition time was 63 min (41 min of VTR and 22 min of VFA, respectively). The multi-echo 3D-UTE sequence and the order of the VFA and VTR acquisitions are depicted in Fig. 1.

2.3. Image reconstruction and relaxation parameter fitting

Images were reconstructed offline using MATLAB (The MathWorks, Inc., Natick, Massachusetts, United States of America) using re-gridding with iterative sampling density compensation and an optimized kernel [25]. Using the first echo of the VFA or VTR data series, spatial maps of the T_1 relaxation time were created by fitting the data to Eq. (2) voxel-by-voxel. To extract T_2^* relaxation times, all VFA and VTR datasets were exponentially fitted to corresponding power images computed from the magnitude data [26]. To account for a potential noise bias [27], the squared exponential fitting was performed with an additional offset parameter. Reconstructed mid-sagittal slices from the isotropic 3D-UTE datasets were used to draw regions-of-interest (ROI) manually in the mid-tendon regions of the patellar and quadriceps tendons. The ROIs were drawn on difference images calculated between the first and second echoes, and subsequently applied to both the T_2^* and T_1 maps. The extracted relaxation times were averaged over all voxels of the ROIs and compared between both tendons as well as the VFA and VTR techniques. On average, the ROIs included 38 and 57 voxels for the patella and quadriceps tendon, respectively. Fig. 2 shows the ROIs and the fit curves in the quadriceps tendon for one single subject. Finally, the average relaxation times were used as boundary parameters for the subsequent bivariate histogram analysis.

2.4. Bivariate histogram analysis

Prior to the calculation of bivariate histograms between T_2^* and T_1, the 3D relaxation parameter maps were masked to exclude contributions from noise regions outside the knee. Masking was performed by intensity thresholding of the magnitude image of the first echo, followed by erosion and dilation to remove outliers. To refine the mask, a

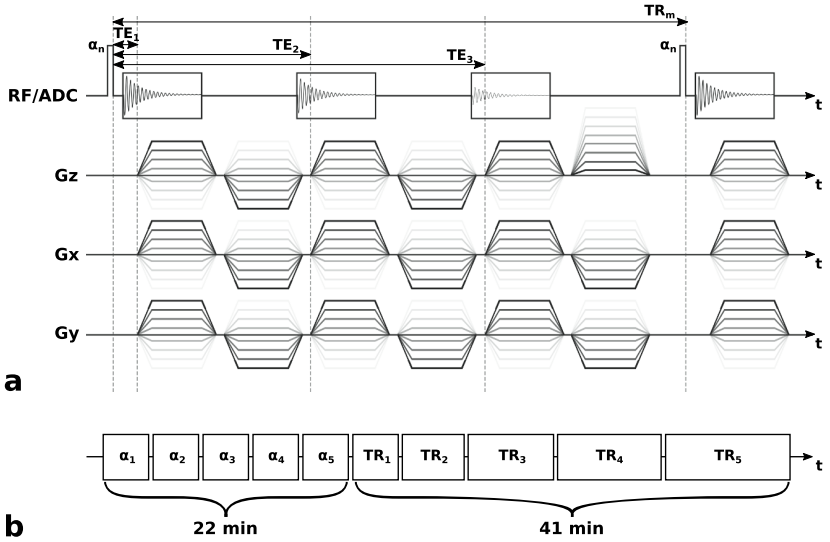

Fig. 1. (a) Sequence diagram depicting the 3D multi-echo UTE acquisition using rectangular excitation pulses with flip angle α_n, echo times TE_1, TE_2 and TE_3, and repetition time TR_m. (b) The course of the experiment showing the order of the different flip angles (VFA method) and repetition times (VTR method).

connectivity analysis was performed to find the connected components in the binary mask with the largest volume. Following extraction of the largest connected component, the resulting binary mask was further processed by closing all holes within the mask with an inverse flood fill operation, i.e., all voxels that cannot be reached by flood filling from the edges of the FoV [28]. The masking process is illustrated for one dataset in Fig. 3.

After masking the 3D relaxation parameter maps, bivariate histograms were calculated by binning the T_1 and T_2^* relaxation times of all voxels into equally sized bins. Because the T_1 relaxation times extracted from the VFA and VTR datasets were very similar (see Fig. 4), only the T_1 values from the VFA method were used for creating the histogram as this method has a shorter acquisition time and is therefore better suited for clinical applications. Clearly visible clusters in the histograms were manually

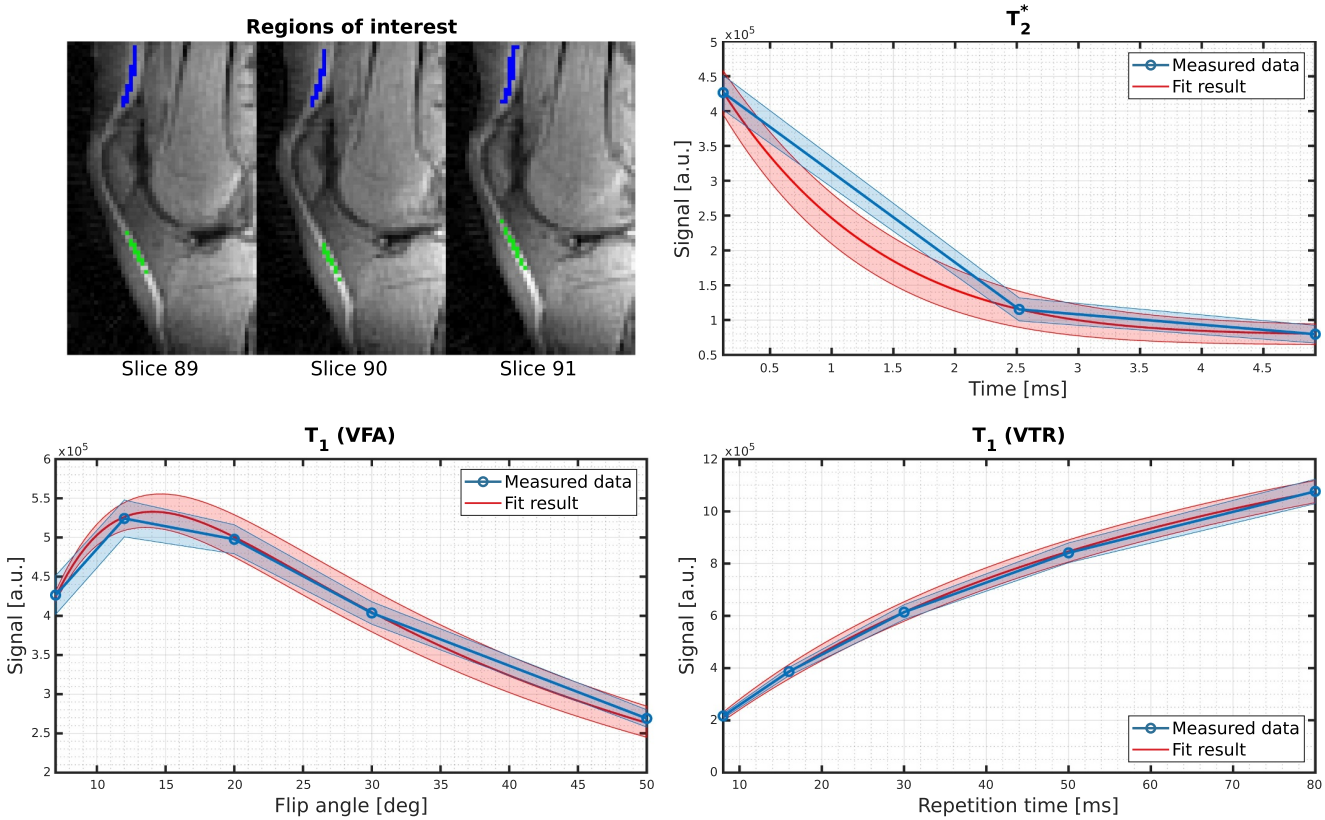

Fig. 2. Placement of tendon ROIs in a single subject for the quadriceps (blue) and patellar (green) tendons (*upper left*). The three plots show the measured signal and the fit results for T_2^* (*upper right*), T_1 (VFA) (*lower left*) and T_1 (VTR) fitting (*lower right*), averaged over the ROIs of the quadriceps tendon. The colored bands depict the standard deviation over the ROIs.

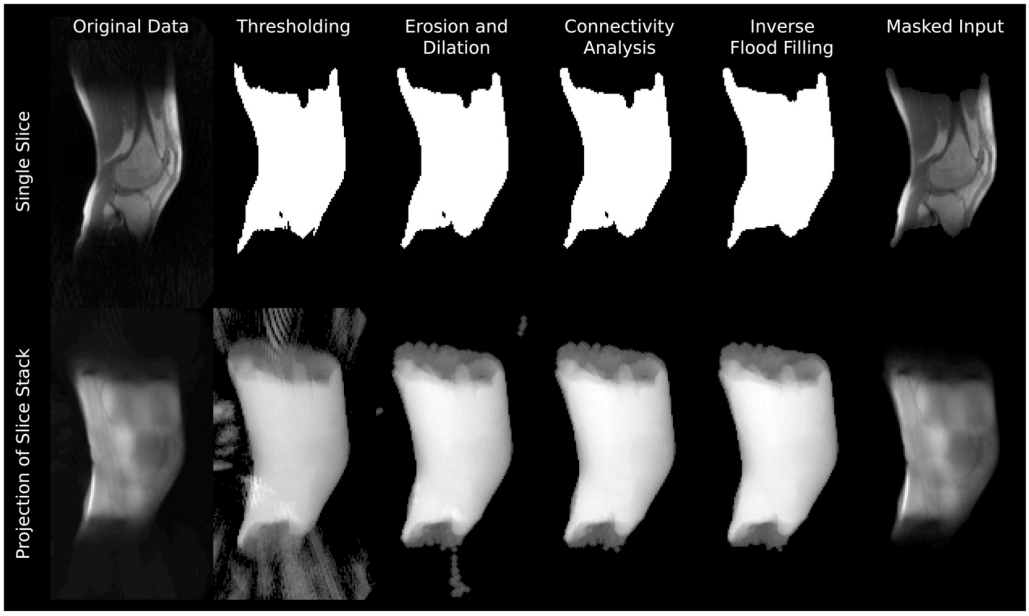

Fig. 3. Illustration of the masking process for the input data to remove outliers prior to bivariate histogram calculation. (*Top row*) Processing steps for obtaining masked data, including thresholding, erosion and dilation, connectivity analysis and inverse flood filling, applied to a single slice. (*Bottom row*) Results of the individual processing steps projected over the entire slice stack.

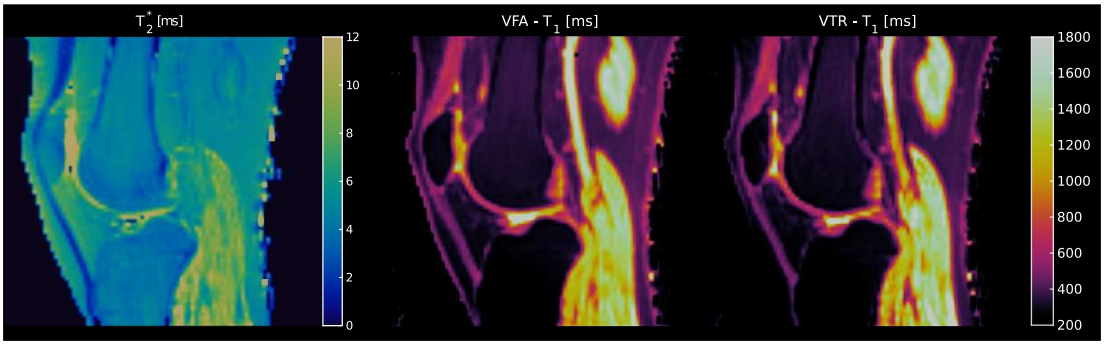

Fig. 4. *Left:* T_2^*-map of a single subject, scaled between 0 ms and 12 ms. *Middle and right*: T_1-maps of the same subject, scaled between 100 ms and 1800 ms, for both the VFA and the VTR methods, respectively. In both maps the patellar and the quadriceps tendons are easily identified by their different relaxation times to the surrounding tissues.

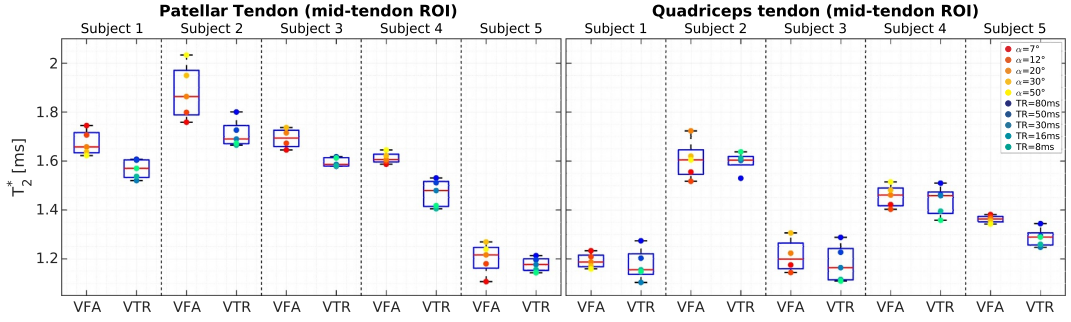

Fig. 5. Box plots of the T_2^* relaxation times derived from manually drawn ROIs in the patellar and quadriceps mid-tendons, obtained from all multi-echo 3D-UTE acquisitions with different flip angles (VFA) and repetition times (VTR).

outlined by drawing ROIs around them, and subsequently visualized using 3D surface reconstruction. To improve the masks resulting from this histogram analysis and to remove outliers, a connectivity analysis similar to that described above was performed prior to visualization, retaining only the largest connected components of the masks. Since no prominent cluster was found in the bivariate histogram located in the range of the extracted T_1 and T_2^* times of the patellar and quadriceps tendons, a ROI was placed in the histogram encompassing a rectangular region in the ranges of 1.0 ms < T_2^* < 3.0 ms and 350 ms < T_1 < 900 ms. Finally, the masks of those cluster ROIs corresponding to bone marrow and the patellar and quadriceps tendons were visualized using a T_1- and T_2^*-based color-encoded semi-transparent 3D volumetric rendering.

3. Results

As shown in Fig. 4, both the patellar and quadriceps tendons were clearly identifiable on the calculated T_2^* maps due to their short T_2^* relaxation times. Since the longest echo-time acquired was only 4.9 ms, the numerical values obtained for other tissues with longer T_2^* relaxation time constants are more uncertain and likely underestimated and should thus be compared with caution to values from the literature. By comparing the inter-individual mean T_2^* values, extracted from the manually drawn ROIs in the mid-tendons, for a wide range of acquisition parameters of the VTR and VFA approach (Fig. 5), several effects are observed: (1) the patellar tendon reveals a broader inter-individual variation of T_2^* values (ranging from 1.2 ms to 1.9 ms) compared to the quadriceps tendon with a range of 1.2 ms to 1.6 ms; (2) averaged over the VFA and VTR acquisitions and all subjects, the mean T_2^* of the quadriceps tendon is slightly lower (1.4 ms ± 0.2 ms) compared to the patellar tendon (1.6 ms ± 0.2 ms); (3) for the different flip angles and repetition times, the intra-individual T_2^* variation was up to 15% for VFA and 9% for VTR, suggesting only small multi-compartment effects on T_2^* within the tendons; (4) in the patellar tendon, the VFA-based T_2^* values were slightly higher compared to the VTR-based results.

Fig. 4 also displays maps of the T_1 relaxation times for both methods. Both the quadriceps and patellar tendons have distinctly different T_1 relaxation times compared to their surrounding tissues, making it easy to identify them. The visual appearance as well as the numerical T_1 values of the tendons derived from the mid-tendon ROIs are comparable between the two methods, with the T_1 values obtained with the VFA method being slightly higher than those obtained with the VTR method. The mean mid-tendon T_1 values of the patellar tendon, averaged over all subjects, were 501 ms ± 67 ms and 453 ms ± 59 ms for the VFA and VTR acquisitions, respectively. Compared to the patellar tendon, the quadriceps mid-tendon had higher mean T_1 values of 716 ms ± 131 ms and 670 ms ± 82 ms for VFA and VTR, respectively. The differences in T_1 between the patellar and quadriceps mid-tendon ROIs were statistically significant ($p < 0.05$) in a two-sided Wilcoxon rank sum test with p-values of 0.02 (VFA) and 0.01 (VTR), respectively.

The bivariate histogram (Fig. 6) revealed several well-delineated clusters, exhibiting similar relaxation parameters in the range of 150 ms < T_1 < 450 ms and 3 ms < T_2^* < 7 ms. Also visible is a broader cluster in the range of 800 ms < T_1 < 1500 ms and 5 ms < T_2^* < 11 ms. In the specific relaxation time range for the patellar and quadriceps tendons, estimated from the previous mid-tendon ROI analysis (1.5 ms < T_2^* < 2.5 ms and 400 ms < T_1 < 850 ms), no distinct clusters were visible. By separating and masking the bivariate histogram, the tissue types underlying the clusters became evident (Fig. 7). The narrow and sharp clusters between 150 ms < T_1 < 450 ms and 3 ms < T_2^* < 7 ms mainly reflect bone marrow (Fig. 7, blue), as well as fat and skin (Fig. 7, green), while the broader cluster with higher T_1 values (Fig. 7, yellow) can be primarily attributed to muscle tissue. By placing an ROI in the range of 1.0 ms < T_2^* < 3.0 ms and 350 ms < T_1 < 900 ms in the bivariate histogram, the patellar and quadriceps tendons could also be extracted (Fig. 7, red). The boundaries of this ROI were extended from the previously obtained mid-tendon values to allow inclusion of more voxels in the transitory regions of the tendons, specifically the patella and tibia entheses.

Average relaxation parameter distributions obtained after segmenting the entire tendon volumes from the bivariate histograms are shown as box plots in Fig. 8 and Fig. 9 for T_2^* and T_1, respectively. Compared to the ROI-based, mid-tendon results (see Fig. 4), the volume-averaged T_2^* values show less variation between both subjects and methods. The mean T_2^* value in the patellar tendon was 1.8 ms ± 0.1 ms, which was again longer compared to the quadriceps tendon (mean T_2^* = 1.4 ms ± 0.2 ms). Overall, volume-based mean T_2^* values were approximately 10% to 15% larger compared to ROI-based mid-tendon results.

Volume-based, average T_1 relaxation times were 527 ms ± 42 ms (VFA) and 476 ms ± 40 ms (VTR) in the patellar tendon, and 662 ms ± 97 ms (VFA) and 637 ms ± 40 ms (VTR) in the quadriceps tendon. Again, the VTR method consistently resulted in shorter T_1 relaxation times compared to the VFA method. Compared to the mid-tendon ROI analysis, the T_1 relaxation times averaged over the entire tendon volume were comparable within 10%.

Based on the segmentation of the patellar and quadriceps tendons (Fig. 7, red), a color-coded 3D volumetric rendering was created to visualize the distributions of T_1 and T_2^* values over the entire tendon volume (Fig. 10), including parts of the tendons entheses. Inspection of these volumetric renderings indicates that T_1 is not constant over the volume of the tendons but contains “hot spots” in some subjects as well as an increase in the relaxation time towards the entheses. On the other hand, T_2^* shows stronger variations between subjects, which may be related to magic angle effects [2,22] due to possible different knee orientations with respect to B_0. Another reason for these higher variations could be partial volume effects due to the limited spatial resolution.

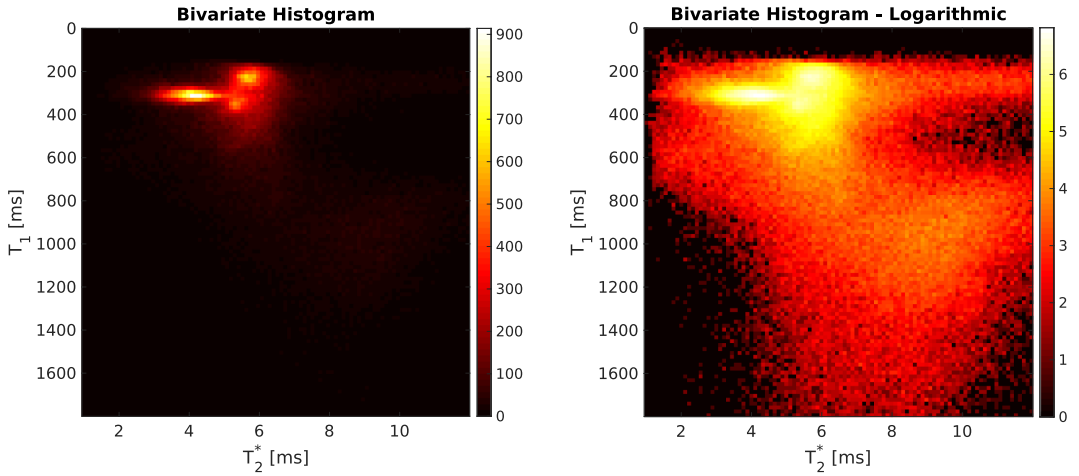

Fig. 6. Bivariate histogram (*left*) and logarithmically-scaled bivariate histogram (*right*) of T_1 and T_2^* showing the color-coded number of voxels corresponding to the respective relaxation times. Several clusters are identifiable in the histogram on the left, corresponding to different tissues. The logarithmic scaling on the right visualizes broader clusters otherwise hidden in the background.

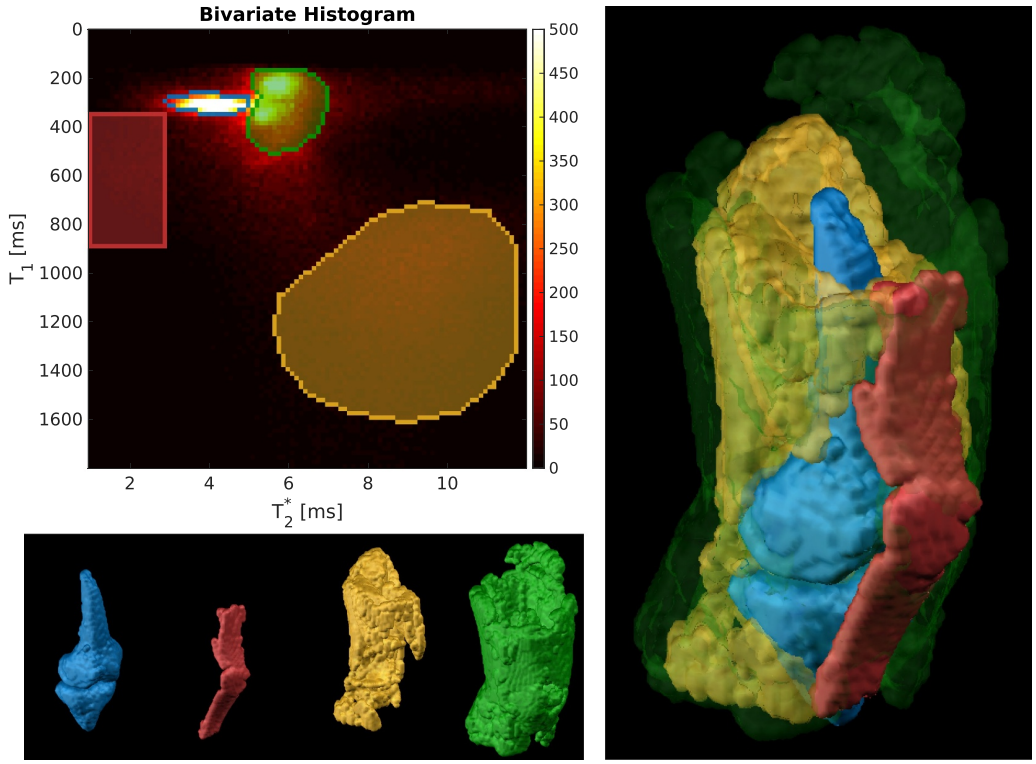

Fig. 7. Based on the bivariate histogram displayed in Fig. 6, clusters were manually selected (*top left*) and visualized as a 3D surface (*bottom left*). The colors correspond to bone marrow (blue), patellar and quadriceps tendons (red), muscle (yellow), as well as skin and other fatty tissue (green). On the right, a combination of all extracted surfaces is shown.

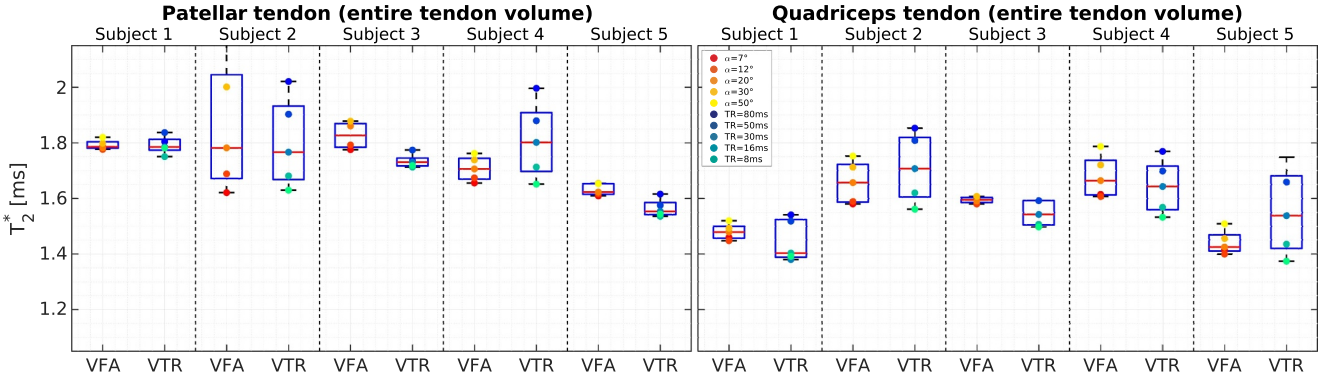

Fig. 8. Box plots of the T_2^* relaxation times, averaged over the entire patellar and quadriceps tendons after segmentation, and obtained from all multi-echo 3D-UTE acquisitions with different flip angles (VFA) and repetition times (VTR).

4. Discussion

The mean T_2^* relaxation time of 1.8 ms for the patellar tendon is comparable with the only known literature reference of 2.0 ms [4]. Similar to the current work, data in that study had also been acquired in vivo and with a 3 T field strength. Although it is conceivable that different tendons in the body should have comparable T_2^* relaxation times, no reference data could be found in the literature for the quadriceps tendon. With T_2^* being much longer than the duration of the short rectangular rf-pulse used for excitation (1.8 ms ≫ 0.15 ms), relaxation effects during the rf-pulse [19,29] should be negligible for the analysis of the VFA and VTR data in estimating T_1. The observed differences in T_2^* between the VFA and VTR methods in the patellar tendon (Fig. 5) might be related to subject motion and partial volume effects due to the limited spatial resolution. Since the datasets were acquired sequentially, even small movements of the subjects between the scans can cause changes in T_2^* as the ROIs shift out of their mid-tendon position. This effect should be more pronounced with the patellar tendon as it is thinner than the quadriceps tendon and thus more susceptible to motion. The higher volume averaged T_2^* values compared to the mid-tendon ROI analysis might be related to the decreases of T_2^* towards the center of the tendons. The intra-individual variation of T_2^* with changing flip angle (VFA) or repetition time (VTR) indicates the presence of multiple compartments with different T_1 relaxation times. Such compartments could be collagen bound water and free water, having different T_1 and T_2^* relaxation times. However, the overall influence of the different T_1 weightings on T_2^* was <15% of the mean T_2^* for all subjects and measurements.

Since the VTR and VFA techniques both resulted in comparable T_1 relaxation times in both tendons, future studies are likely to favor the

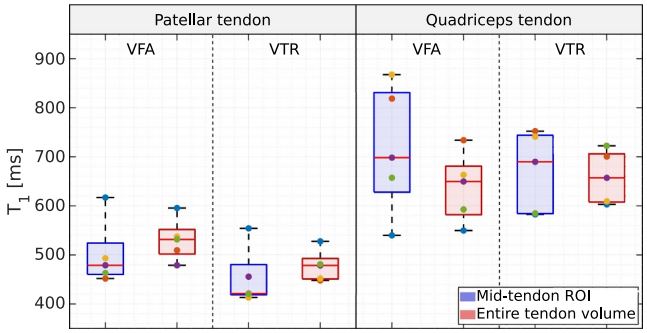

Fig. 9. Comparison between T_1 relaxation times obtained from VFA and VTR in the mid-tendon regions (blue) of the patellar (*left*) and quadriceps tendon (*right*) and the entire tendon volumes after segmentation (red).

VFA technique due to its shorter acquisition time. Due to the already long total acquisition time, we restricted the maximum TR in our study to 80 ms with the VTR technique. Considering that the T_1 relaxation times in both tendons are significantly longer, more extended TRs would have been necessary for optimal sampling of the T_1 saturation recovery curves with VTR. Consequently, the T_1 relaxation times obtained with the VTR technique in our study are most likely underestimated, especially since additional water compartments with longer T_1 relaxation times might exist in tendons. This assumption of underestimation is further supported by the fact that the VFA-based T_1 values were slightly longer for both tendons and all subjects than the VTR results. The VTR technique, on the other hand, could be of advantage when performing T_1 mapping on high field (preclinical) systems, for which the rf-pulse performance may be inferior regarding stability of flip-angles or B_1 inhomogeneity effects may be stronger. In the present study, B_1 inhomogeneities were not taken into account for several reasons. Mapping of B_1 in tendons or tissues with very short T_2^* relaxation times is generally challenging because standard B_1 mapping techniques [30–32] do not show signal in such tissues and calibrate their flip angles consequently on long T_2 tissues, or require very long TRs, which are impractical for isotropic 3D acquisitions. One promising approach for B_1 mapping is the actual flip angle imaging (AFI) method [33,34], which uses an interleaved acquisition with two different repetition times. This method has only recently been demonstrated to work with 3D UTE acquisition; however, with an anisotropic resolution [24,35]. A major limitation of UTE-AFI based B_1 mapping is a highly prolonged total acquisition time when applied with isotropic high resolution, as is advantageous for 3D segmentation and visualization. Because B_1 inhomogeneities were not corrected in this study, the obtained T_1 values of the patellar and quadriceps tendon could be over- or underestimated, where the over- or underestimation may also depend on blurring from surrounding tissues and chemical shift artifacts.

The only known reference data for T_1 values in the patellar and quadriceps tendons are 656 ± 43 ms and 800 ± 66 ms, respectively [24]. While comparable, these values are slightly higher than those found in the current study. As outlined above, these differences are likely due to the application of B_1 correction based on UTE-AFI in ref. [24], which could result in increased T_1 values. Another reason for the discrepancy may be ROI placement. As demonstrated by the 3D visualization (Fig. 10), T_1 varies within the tendons on the individual level, implying that placement and size of ROIs can affect the mean values. The differences in T_1 between both tendons could be due to the fact that the patellar tendon is a ligament connecting bone to bone (i.e., patella to tibia), whereas the quadriceps tendon connects bone to muscle (patella to quadriceps). Available 3D segmentation techniques, and thus 3D mapping of T_1 and T_2^* distributions, should enable future studies to investigate physiological influences, such as age, physical training or pathologies, on changes in these distributions of relaxation parameters over the entire tendon volume.

The bivariate histogram analysis of the relaxation time maps applied in the present work is limited by three major factors. First, only three echoes with short echo times (4.9 ms being the longest) were acquired, from which T_2^* was estimated. This could have resulted in underestimation of the values derived for tissues with longer T_2^* relaxation times, and therefore, caused the clusters in the histogram to be

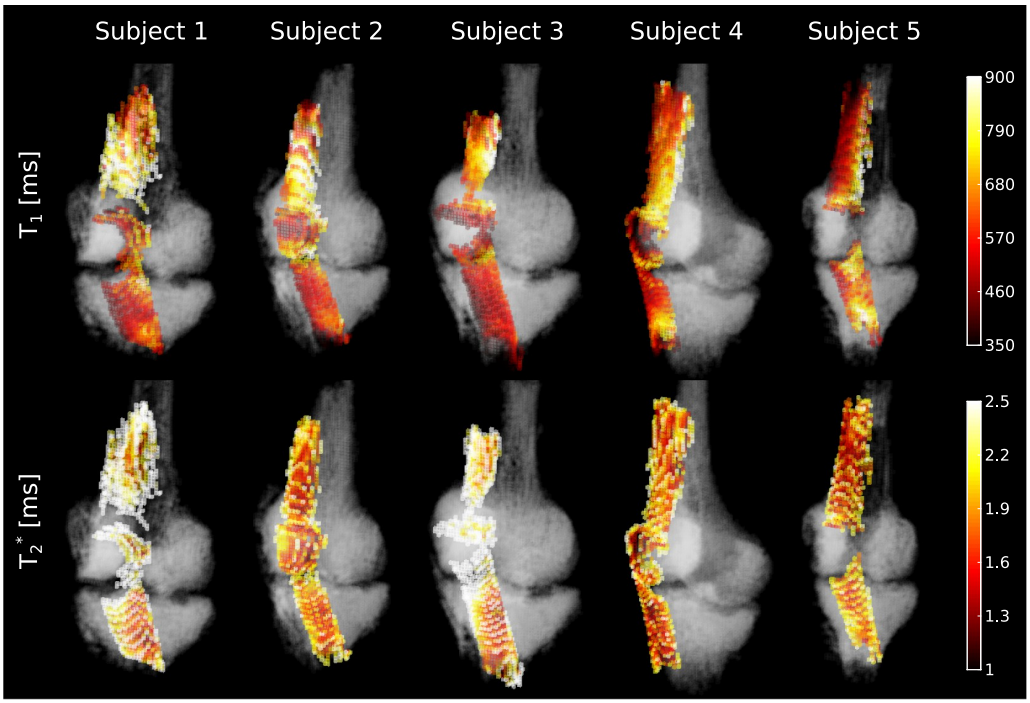

Fig. 10. Color-coded volumetric 3D renderings of T_1 (*top*) and T_2^* (*bottom*) for all five subjects. For geometrical reference, the segmented bones are also shown semi-transparently with gray levels.

compressed in the range along the T_2^* axis. Second, the spatial resolution of 2.0 × 2.0 × 2.0 mm^3 is relatively low, which is due to the fact that both VFA and VTR were acquired for comparing the T_1 mappings, and total measurement time was limited to approximately 1 h to reduce motion between separate scans with different flip angles and TRs. Future experiments should not only omit the VTR scan entirely, but should also combine the 3D-UTE acquisition and reconstruction with acceleration techniques, such as SENSE [36,37] or compressed sensing [38], to benefit from reduced scan time and increased spatial resolution. Lastly, by combining the VFA acquisition with B_1 mapping and inhomogeneity compensation, and using advanced shimming for B_0 homogenization, the extent of the T_1 and T_2^* clusters in the bivariate histogram may be reduced, potentially leading to a more robust and fully-automatic 3D segmentation.

By comparing the relaxation times obtained from the manually drawn mid-tendon ROIs with the values averaged over the segmented tendon volume, we could show that placement of ROIs is crucial for obtaining consistent and trustworthy results. Although the obtained relaxation times were comparable for both T_2^* and T_1, the inter-individual variations were reduced by averaging over the entire segmented tendon volumes. Variations in the mid-tendon ROIs might have been caused by partial volume effects, motion between the separate VFA and VTR scans or by errors in drawing the manual ROIs.

In conclusion, we have demonstrated similar T_1 relaxation parameters extracted from 3D-UTE VFA and VTR acquisitions for knee tendons, and contributed additional reference data to the currently sparse literature regarding relaxation times in the quadriceps and patellar tendons. Furthermore, by combining 3D isotropic T_1 and T_2^* mapping of the entire knee with a bivariate histogram analysis, we were able to segment the quadriceps and patellar tendons, and visualize the relaxation parameter distributions over the entire tendon volume.

Acknowledgments

This work was supported by the German Research Foundation (DFG, DU 298/25-1, RE 1123/22-1, ZA 592/4-1) and the Interdisciplinary Center for Clinical Research (IZKF, J64) in Jena, Germany. The authors have no relevant financial conflicts to disclose with regard to this study.

References

[1] Cook JL, Khan KM, Purdam CR. Conservative treatment of patellar tendinopathy. Phys Ther Sport 2001;2(2):54–65. https://doi.org/10.1054/ptsp.2001.0069.
[2] Fullerton GD, Rahal A. Collagen structure: the molecular source of the tendon magic angle effect. J Magn Reson Imaging 2007;25(2):345–61. https://doi.org/10.1002/jmri.20808.
[3] Jerban S, Nazaran A, Cheng X, Carl M, Szeverenyi N, Du J, et al. Ultrashort echo time T2 ∗ values decrease in tendons with application of static tensile loads. J Biomech 2017;61:160–7. https://doi.org/10.1016/j.jbiomech.2017.07.018.
[4] Grosse U, Springer F, Hein T, Grözinger G, Schabel C, Martirosian P, et al. Influence of physical activity on T1 and T_2^* relaxation times of healthy achilles tendons at 3T. J Magn Reson Imaging 2015;41(1):193–201. https://doi.org/10.1002/jmri.24525.
[5] Grosse U, Syha R, Hein T, Gatidis S, Grözinger G, Schabel C, et al. Diagnostic value of $T_{1\ 1}$ and T_2^* relaxation times and off-resonance saturation effects in the evaluation of achilles tendinopathy by MRI at 3T: MR evaluation of Achilles tendinopathy. J Magn Reson Imaging 2015;41(4):964–73. https://doi.org/10.1002/jmri.24657.
[6] Kijowski R, Wilson JJ, Liu F. Bicomponent ultrashort echo time T_2^* analysis for assessment of patients with patellar tendinopathy. J Magn Reson Imaging 2017;46(5):1441–7. https://doi.org/10.1002/jmri.25689.
[7] Robson MD, Gatehouse PD. Consequences of T2 relaxation during half-pulse slice selection for ultrashort TE imaging. Magn Reson Med 2010;64(2):610–5. https://doi.org/10.1002/mrm.22323.
[8] Josan S, Pauly JM, Daniel BL, Pauly KB. Double half RF pulses for reduced sensitivity to eddy currents in UTE imaging. Magn Reson Med 2009;61(5):1083–9. https://doi.org/10.1002/mrm.21879.
[9] Rahmer J, Börnert P, Groen J, Bos C. Three-dimensional radial ultrashort echo-time imaging with T2 adapted sampling. Magn Reson Med 2006;55(5):1075–82. https://doi.org/10.1002/mrm.20868.
[10] Rahmer J, Blume U, Börnert P. Selective 3D ultrashort TE imaging: comparison of "dual-echo" acquisition and magnetization preparation for improving short-T2 contrast. Magn Reson Mater Phys Biol Med 2007;20(2):83–92. https://doi.org/10.1007/s10334-007-0070-6.
[11] Krämer M, Motaal AG, Herrmann K-H, Löffler B, Reichenbach JR, Strijkers GJ, et al. Cardiac 4D phase-contrast CMR at 9.4 T using self-gated ultra-short echo time (UTE) imaging. J Cardiovasc Magn Reson 2017;19(1):39. https://doi.org/10.1186/s12968-017-0351-9.
[12] Herrmann K-H, Krämer M, Reichenbach JR. Time efficient 3D radial UTE sampling with fully automatic delay compensation on a clinical 3T MR scanner. Fan X, editor. PLOS ONE 2016;11(3):e0150371. https://doi.org/10.1371/journal.pone.0150371.
[13] Koff MF, Pownder SL, Shah PH, Yang LW, Potter HG. Ultrashort echo imaging of cyclically loaded rabbit patellar tendon. J Biomech 2014;47(13):3428–32. https://doi.org/10.1016/j.jbiomech.2014.08.018.
[14] Chang EY, Du J, Iwasaki K, Biswas R, Statum S, He Q, et al. Single- and Bi-component T_2^* analysis of tendon before and during tensile loading, using UTE sequences: T_2^* Analysis of Tendon With Tension. J Magn Reson Imaging 2015;42(1):114–20. https://doi.org/10.1002/jmri.24758.
[15] Zhu DC, Penn RD. Full-brain T1 mapping through inversion recovery fast spin echo imaging with time-efficient slice ordering. Magn Reson Med 2005;54(3):725–31. https://doi.org/10.1002/mrm.20602.
[16] Deichmann R, Hahn D, Haase A. Fast T1 mapping on a whole-body scanner. Magn Reson Med 1999;42(1):206–9. https://doi.org/10.1002/(SICI)1522-2594(199907)42:1<206::AID-MRM28>3.0.CO;2-Q.
[17] Ordidge RJ, Gibbs P, Chapman B, Stehling MK, Mansfield P. High-speed multislice T_1 mapping using inversion-recovery echo-planar imaging. Magn Reson Med 1990;16(2):238–45. https://doi.org/10.1002/mrm.1910160205.
[18] Fram EK, Herfkens RJ, Johnson GA, Glover GH, Karis JP, Shimakawa A, et al. Rapid calculation of T1 using variable flip angle gradient refocused imaging. Magn Reson Imaging 1987;5(3):201–8. https://doi.org/10.1016/0730-725X(87)90021-X.
[19] Springer F, Steidle G, Martirosian P, Syha R, Claussen CD, Schick F. Rapid assessment of longitudinal relaxation time in materials and tissues with extremely fast signal decay using UTE sequences and the variable flip angle method. Invest Radiol 2011;46(10):610–7. https://doi.org/10.1097/RLI.0b013e31821c44cd.
[20] Du J, Bydder GM. Qualitative and quantitative ultrashort-TE MRI of cortical bone. NMR Biomed 2013;26(5):489–506. https://doi.org/10.1002/nbm.2906.
[21] Wellen J, Helmer KG, Grigg P, Sotak CH. Spatial characterization of T1 andT2 relaxation times and the water apparent diffusion coefficient in rabbit Achilles tendon subjected to tensile loading. Magn Reson Med 2005;53(3):535–44. https://doi.org/10.1002/mrm.20361.
[22] Du J, Chiang AJ-T, Chung CB, Statum S, Znamirowski R, Takahashi A, et al. Orientational analysis of the Achilles tendon and enthesis using an ultrashort echo time spectroscopic imaging sequence. Magn Reson Imaging 2010;28(2):178–84. https://doi.org/10.1016/j.mri.2009.06.002.
[23] Wengler K, Tank D, Fukuda T, Paci JM, Huang M, Schweitzer ME, et al. Diffusion tensor imaging of human Achilles tendon by stimulated echo readout-segmented EPI (ste-RS-EPI). Magn Reson Med 2018;80(6):2464–74. https://doi.org/10.1002/mrm.27220.
[24] Ma Y-J, Zhao W, Wan L, Guo T, Searleman A, Jang H, et al. Whole knee joint T $_1$ values measured in vivo at 3T by combined 3D ultrashort echo time cones actual flip angle and variable flip angle methods. Magn Reson Med 2019;81(3):1634–44. https://doi.org/10.1002/mrm.27510.
[25] Zwart NR, Johnson KO, Pipe JG. Efficient sample density estimation by combining gridding and an optimized kernel. Magn Reson Med 2012;67(3):701–10. https://doi.org/10.1002/mrm.23041.
[26] Miller AJ, Joseph PM. The use of power images to perform quantitative analysis on low SNR MR images. Magn Reson Imaging 1993;11(7):1051–6. https://doi.org/10.1016/0730-725X(93)90225-3.
[27] Henkelman RM. Measurement of signal intensities in the presence of noise in MR images: technical reports: signal intensities in MR image noise. Med Phys 1985;12(2):232–3. https://doi.org/10.1118/1.595711.
[28] M. Krämer, B. Herzau, J.R. Reichenbach, Segmentation and visualization of the human cranial bone by T_2^* approximation using ultra-short echo time (UTE) magnetic resonance imaging. Z Med Phys; Epub ahead of print, https://doi.org/10.1016/j.zemedi.2019.06.003.
[29] Springer F, Steidle G, Martirosian P, Claussen CD, Schick F. Effects of in-pulse transverse relaxation in 3D ultrashort echo time sequences: analytical derivation, comparison to numerical simulation and experimental application at 3T. J Magn Reson 2010;206(1):88–96. https://doi.org/10.1016/j.jmr.2010.06.010.
[30] Klose U. Mapping of the radio frequency magnetic field with a MR snapshot FLASH technique. Med Phys 1992;19(4):1099–104. https://doi.org/10.1118/1.596828.
[31] Insko EK, Bolinger L. Mapping of the radiofrequency field. J Magn Reson A 1993;103(1):82–5. https://doi.org/10.1006/jmra.1993.1133.
[32] Chung S, Kim D, Breton E, Axel L. Rapid B1 + mapping using a preconditioning RF pulse with Turbo FLASH readout. Magn Reson Med 2010;64(2):439–46. https://doi.org/10.1002/mrm.22423.
[33] Yarnykh VL. Actual flip-angle imaging in the pulsed steady state: a method for rapid three-dimensional mapping of the transmitted radiofrequency field. Magn Reson Med 2007;57(1):192–200. https://doi.org/10.1002/mrm.21120.
[34] Nehrke K. On the steady-state properties of actual flip angle imaging (AFI). Magn Reson Med 2009;61(1):84–92. https://doi.org/10.1002/mrm.21592.
[35] Ma Y-J, Lu X, Carl M, Zhu Y, Szeverenyi NM, Bydder GM, et al. Accurate T $_1$ mapping of short T $_2$ tissues using a three-dimensional ultrashort echo time cones actual flip angle imaging-variable repetition time (3D UTE-Cones AFI-VTR) method. Magn Reson Med 2018;80(2):598–608. https://doi.org/10.1002/mrm.27066.
[36] Pruessmann KP, Weiger M, Scheidegger MB, Boesiger P. SENSE: sensitivity encoding for fast MRI. Magn Reson Med 1999;42(5):952–62. https://doi.org/10.1002/(SICI)1522-2594(199911)42:5<952::AID-MRM16>3.0.CO;2-S.
[37] Pruessmann KP, Weiger M, Börnert P, Boesiger P. Advances in sensitivity encoding with arbitrary *k* -space trajectories. Magn Reson Med 2001;46(4):638–51. https://doi.org/10.1002/mrm.1241.
[38] Lustig M, Donoho D, Pauly JM. Sparse MRI: the application of compressed sensing for rapid MR imaging. Magn Reson Med 2007;58(6):1182–95. https://doi.org/10.1002/mrm.21391.

5.2 Optimized gradient spoiling of UTE VFA-AFI sequences for robust T_1 estimation with B_1-field correction

Authors: M.B. Maggioni, M. Krämer , J.R. Reichenbach

Magnetic Resonance Imaging 82 (2021) 1–8

Contents lists available at ScienceDirect

Magnetic Resonance Imaging

journal homepage: www.elsevier.com/locate/mri

Optimized gradient spoiling of UTE VFA-AFI sequences for robust T_1 estimation with B_1-field correction

Marta B. Maggioni *, Martin Krämer, Jürgen R. Reichenbach

Medical Physics Group, Institute of Diagnostic and Interventional Radiology, Jena University Hospital – Friedrich Schiller University Jena, Germany

ARTICLE INFO

Keywords:
B_1 mapping
Actual Flip angle imaging
UTE
T_1 mapping
Variable Flip angle
Spoiling

ABSTRACT

Quantifying T_1 relaxation times is a challenge because inhomogeneities of the B_1 field have to be corrected to obtain proper values. It is a particular challenge in tissues with short T_2* values, for which conventional MRI techniques do not provide sufficient signal. Recently, a B_1-field correction technique called AFI (Actual Flip angle Imaging) has been introduced that can be combined with UTE (ultra-short echo-time) sequences, which have much shorter echo times compared to conventional MRI techniques, allowing quantification of signal in short T_2* tissues. A disadvantage of AFI is that it requires very long relaxation delays between repetitions to minimize the influence of imperfect spoiling of transverse magnetization on signal behavior. In this work, we propose a novel spoiling scheme for the AFI sequence that efficiently provides accurate B_1 correction maps with strongly reduced acquisition time. We validated the method with both phantom and preliminary *in vivo* results.

1. Introduction

With MRI being certainly one of the most versatile and powerful diagnostic imaging modalities, the evolution toward quantification has further increased its potential by enabling non-invasive quantitative mapping of various parameters [1]. Basic quantitative parameters include the relaxation time constants T_2, T_2* and T_1. Accurate mapping of these parameters and their subsequent careful analysis promises a possible assessment of early stages of degeneration in tissues [2,3]. This is of particular importance in the field of musculoskeletal MRI, for example in the diagnosis of osteoarthritis or anterior cruciate ligament injury, as changes in tissue composition may be manifested in these parameters prior to structural degradation [1–4], allowing early diagnosis and treatment.

In contrast to T_2/T_2* quantification of musculoskeletal tissues, for which there are a large number of methods in the literature, T_1 quantification has always been considered much more difficult, since inhomogeneities of the B_1 field (reflected in the flip angle estimates) are one of the major sources of uncertainty in T_1 estimation [5,6]. This is especially true for the often used VFA (Variable Flip Angle) method. While this method is time efficient [4], it is highly susceptible to inaccuracies in the excitation flip angles. This problem becomes even more relevant with clinical high-field MRI systems, for which B_1 variations can lead to T_1 estimation errors of up to 30% [5,6]. This, in turn, requires spatial B_1 field maps to correctly quantify T_1; however, there is no direct way to measure the B_1 field distribution for a given rf-excitation coil. Consequently, many "indirect methods" have been proposed, most of which are based on acquiring two consecutive measurements and calculating the B_1 field correction map from signal ratios. One of the simplest ideas is the so-called Double Angle Method (DAM) [7,8], where images with two different flip angles (ϑ and 2ϑ) are acquired and then combined. However, this method results in long acquisition times, high rf-power deposition, and potential registration problems between the two separately acquired images [9]. Other, phase-based, methods employ composite RF pulses [10] or apply off-resonance pulses to generate a phase shift with an associated phase accumulation that has been shown to encode the B_1 field [11,12].

However, most of these methods have shown a dependence on the T_1 value [13] and suffer from extremely long acquisition times, which often makes them unsuitable for clinical applications. Furthermore, all of these methods perform poorly when applied to tissues with short T_2* values, whose transverse relaxation times range from about 100 μs or less to a few ms at most. For echo-times of at least a few milliseconds, as used by the above techniques, the signal is almost completely decayed in short T_2*-tissues, such as tendons, ligaments or compact bone. Consequently, B_1 maps extracted from conventional B_1 mapping techniques contain missing or erroneous values for such tissues. With recent advances in ultrashort echo-time (UTE) imaging and its increasing use

* Corresponding author at: Medical Physics Group, IDIR, Jena University Hospital, Philosophenweg 3, D-07443 Jena, Germany.
E-mail addresses: marta.maggioni@uni-jena.de (M.B. Maggioni), Juergen.Reichenbach@med.uni-jena.de (J.R. Reichenbach).

https://doi.org/10.1016/j.mri.2021.06.011
Received 21 November 2020; Received in revised form 21 May 2021; Accepted 15 June 2021
Available online 18 June 2021

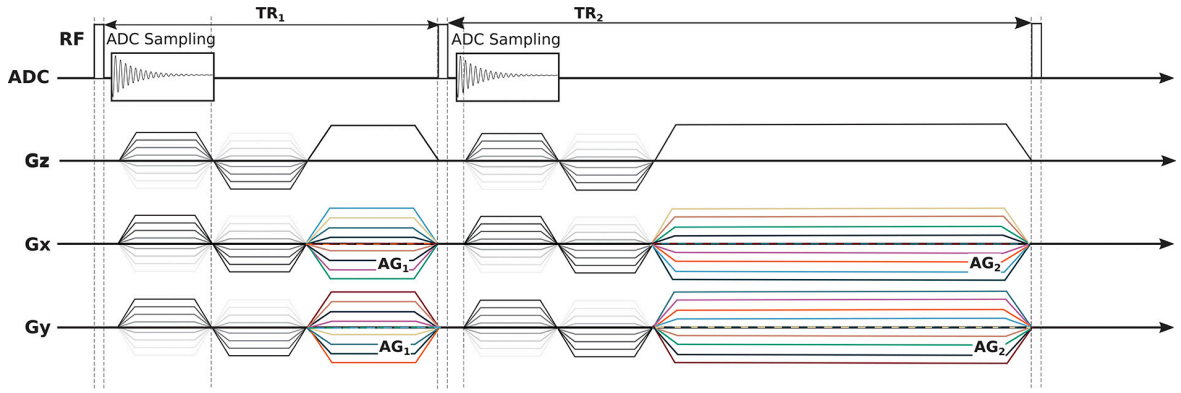

Fig. 1. Sequence diagram of the proposed AFI methods. A short delay is implemented between data acquisition and the ramping up of the gradients [26]. Note that the spoiling gradients in the z direction are kept constant [26], while the direction of the spoiling gradients in the x-y-plane is random (represented by the different line styles).

[14–16], a robust B_1-mapping technique that can be easily combined with UTE acquisition would greatly improve the applicability of T_1 mapping of short T_2* tissues.

One B_1 mapping technique that can be combined with UTE acquisition is the recently proposed Actual Flip angle Imaging (AFI) [17]. The AFI sequence [17,18] acquires two signals (S_1 and S_2) with different repetition times (TR_1 and TR_2) but constant flip angle in an interleaved manner and has been shown to be suitable for *in vivo* applications. One particular advantage of AFI is that it does not require preparation pulses or spin-echoes [19] and can therefore be combined with UTE imaging.

The main disadvantage of AFI is that it uses a pulsed steady-state signal that has been shown to be strongly affected by incomplete spoiling [18,20–23], potentially leading to incorrect B_1 correction factors. The latter can be improved by "perfect" spoiling of the residual transverse magnetization by combining large gradient spoiler areas [18] with optimized values of the radiofrequency phase increment [20–23]. RF spoiling is achieved by varying the phase of the RF pulse between each TR by a specific phase increment φ, for which different values have been proposed for different applications [17]. In the works of Yarnykh [17,18] and Nehrke [23] it has been discussed that a diffusional dephasing effect, caused by large gradient spoiler areas, contributes to the stabilization of the AFI method. This is beneficial to make the method more robust, as the dephasing of the residual transverse magnetization becomes less dependent on the actual, commonly fixed, value of the phase increment used by the vendors. The latter can differ due to differently implemented rf-spoiling schemes. Often these fixed values can only be modified by the user if there is access to the source code of the sequence. On the other hand, the large gradient spoiler areas associated with the additional dephasing can lead to prohibitively long acquisition times, since a long TR is required to accommodate the gradient spoilers in the sequence. Long acquisition times can further lead to substantial heating of the gradient system, which in turn can cause B_0-drifts [24] during the AFI measurement.

In the present study, an alternative gradient spoiling scheme for a UTE-AFI sequence is proposed that allows smaller gradient spoilers by introducing randomization of the direction of the spoiler gradients in the x-y plane. The method is applied to UTE based Variable Flip Angle T_1 quantification, compared with current literature, and validated with a comprehensive phantom analysis and an *in vivo* example.

2. Materials and methods

2.1. Theory of AFI

Consider an MRI gradient echo sequence characterized by identical RF pulses and two alternating repetition times TR_1 and TR_2; assuming that the latter are short compared to T_1 of the tissue under study, a pulsed-steady-state condition is reached. In the pulsed steady state, the longitudinal magnetizations $M_{z1,\ 2}$ before the next pulse are obtained from a consecutive solution of the Bloch equations [25], as shown by Yarnykh [17]:

$$M_{z1} = M_0 \frac{1 - E_2 + (1 - E_1)E_2 cos\vartheta_{actual}}{1 - E_1 E_2 cos^2\vartheta_{actual}} \tag{1}$$

$$M_{z2} = M_0 \frac{1 - E_1 + (1 - E_2)E_1 cos\vartheta_{actual}}{1 - E_1 E_2 cos^2\vartheta_{actual}} \tag{2}$$

$E_{1,\ 2}$ stands for $e^{\frac{-TR_{1,2}}{T_1}}$, respectively, and the two signals S_1 and S_2 can be expressed as follows:

$$S_{1,2} = M_{z1,2} e^{\frac{-TE}{T_2^*}} sin\vartheta_{actual} \tag{3}$$

A B_1 field correction map can be calculated from the ratios r and n between the two signals S_1 and S_2 and the repetition times TR_1 and TR_2 as follows:

$$r = \frac{S_2}{S_1} = \frac{1 - E_1 + (1 - E_2)E_1 cos\vartheta_{actual}}{1 - E_2 + (1 - E_1)E_2 cos\vartheta_{actual}} \tag{4}$$

$$n = \frac{TR_2}{TR_1} \tag{5}$$

Assuming that TR_1 and TR_2 are short compared to the measured T_1, the term r can be simplified applying a first order exponential approximation:

$$r = \frac{1 + n cos\vartheta_{actual}}{n + cos\vartheta_{actual}} \tag{6}$$

from which ϑ_{actual} can be derived

$$\vartheta_{actual} = arccos\frac{r \cdot n - 1}{n - r} \tag{7}$$

ϑ_{actual} is the actual flip angle that deviates from the nominally selected flip angle, $\vartheta_{nominal}$, due to B_1 inhomogeneities. Consequently, a map of the B_1-field correction factor can be calculated for each voxel:

$$B_{1\ corr.fact.} = \vartheta_{actual} / \vartheta_{nominal} \tag{8}$$

From Eqs. (6)–(7) it can be seen that increasing n translates to increased variability of r, allowing smaller changes in flip angle to be measured (higher dynamic range). However, there is a trade-off between increasing n and acquisition time constraints. In the literature [17], values for n between 4 and 6 have been found to be optimal when coupled with a nominal flip angle ($\vartheta_{nominal}$) range between 40°-80° for

Table 1
List of scans acquired during the first phantom experiment. The first column denotes the scan number (same Roman numbering is used in Fig. 2), the second lists the common settings of some of the sequences, while the last column contains the areas of the spoiling gradients (note that the values of the gradient areas AG_1 and AG_2 are the same for the spoiling gradient in z-direction and in the randomized direction in the x-y-plane for a selected scan). The TRs are in ms and the areas of the gradients are in mT·ms/m.

Scan	Sequence characteristics	Spoiler gradient areas
I	z_{const}, $TR_1/TR_2 = 20/100$	447/2236
II		55/280
III	z_{const}, xy_{rand} $TR_1/TR_2 = 20/100$	447/2236
IV		55/280
V		27/130
VI		11/60
VII		5/33
VIII	z_{const}, xy_{rand} $TR_1/TR_2 = 15/75$	55/280
IX		27/130
X		11/60
XI		5/33
XII	z_{const}, xy_{rand} $TR_1/TR_2 = 10/50$	55/280
XIII		27/130
XIV		11/60
XV		5/33

AFI acquisition.

2.2. Imaging sequence

The AFI sequence was implemented by adding two adjustable interleaved TRs to a 3D radial center-out UTE sequence with hard pulse excitation [27]. Further modifications included the introduction of gradient spoilers in all three spatial directions with adjustable gradient areas for TR_1 and TR_2. While in the z-direction the gradient spoilers were played out alternately with the two different preselected gradient areas, the direction of the gradient spoilers in the x- and y-plane was additionally randomized for each TR. A sequence diagram is shown in Fig. 1. The randomized x-y spoiling was achieved by using the *rand()* function of the C++ standard library to choose a random rotation angle of the spoiling gradient between 0 and 360° in the x-y-plane. This randomization yields different rotation angles for each run of the sequence. The goal of changing the direction of the x-y spoiling with each TR was to scramble the residual transverse magnetization to stabilize the steady-state of the sequence. To investigate the influence of the RF phase increment φ on the AFI derived B_1 maps and its dependence on the gradient spoiling, the sequence also allowed repetition of data acquisition for different values of φ (sweep from 0° to 180° in steps of 4°), thus ensuring that a full RF phase increment sweep was performed in a single sequence run without intermediate scanner readjustments. All measurements were performed on a clinical 3 T whole-body MRI scanner (Magnetom PRISMA, Siemens Healthineers, Erlangen, Germany) using the vendor supplied single channel transmit and receive knee coil. The proposed method, characterized by constant z-spoiling and additional randomized gradient spoilers in the x- and y-direction, was optimized and validated with both phantom and *in vivo* experiments on two phantoms. One phantom consisted of two cylindrical tubes (diameter: Ø 2 cm), while the other one was composed by a roll of adhesive tape (known to be a short T_2* material [28]) and four cylindrical tubes. The tubes were filled with agar and aqueous solutions with different Gadovist concentrations (0.6 mM, 0.5 mM, 0.19 mM, 0.04 mM) to mimic typical T_1 values of *in vivo* tissues (estimated nominal T_1 of 450 ms, 550 ms, 1200 ms and 2800 ms, respectively). In addition, T_1 quantification in the knee of a healthy volunteer (f., 27 y) was performed as an *in vivo* application of the proposed method.

2.3. Optimization of the proposed method

A phantom experiment was performed to explore the influence of TR, spoiler gradient area (AG) and RF phase increment value on the extracted T_1 values after B_1 correction to optimize the proposed method. A total of 15 AFI measurements were acquired with different TR_1/TR_2 and AG_1/AG_2 combinations (see Table 1). Each measurement was repeated with a sweep of the RF phase increment (ranging from 0° to 180° in steps of 4°) to investigate the effect on the final T_1 maps. Each AFI B_1-field correction map (see Eq. (8)) was used to correct the T_1 maps of the same phantom obtained from a VFA acquisition [27] with a set of different flip angles (5°, 9°, 11°, 15°, 22°, 25°, 30°, 35°, 40°) and three different TRs of 20 ms, 15 ms and 10 ms to match the TR_1 of the corresponding AFI scan (Table 1). The acquisition time of the AFI measurement (for a single φ value) was 6.58 min, 5.12 min and 3.29 min for TR of 20 ms, 15 ms and 10 ms, respectively.

Table 2
Summary of AFI-based B_1 correction methods from the literature tested against the proposed method, with the corresponding references and the abbreviations and Roman numerals used to refer to them in the text.

Sequence characteristics	Abbreviations	References
Constant z-spoiling (I)	z_{const}	[Yarnyk] [18]
Constant z-spoiling & random rf phase (II)	z_{const}, ϕ_{rand}	[Zur et al.] [Freeman and Hill] [30,31]
Random z-spoiling (III)	z_{rand}	[Darrasse et al.] [32]
Random z-spoiling & random rf phase (IV)	z_{rand}, ϕ_{rand}	[Lin and Song] [33]
Constant z-spoiling & randomized x-y-spoiling (V)	z_{const}, xy_{rand}	Proposed method

2.4. Comparison with other B_1-mapping techniques

To test the validity of the proposed method and to demonstrate its ability to retrieve signal in short T_2* species, an experiment was performed on a "short T_2* phantom". Three different AFI measurements were acquired: one with the parameters proposed by Yarnykh [18] and two with the proposed method with TR_1/TR_2 of 10/50 ms and gradient areas of 27/130 ms·mT/m and 55/280 ms·mT/m, respectively. The AFI measurements were used to correct a UTE VFA-based T_1 quantification. For comparison, a vendor supplied gradient echo sequence was used to implement a VFA-based T_1 mapping, which was corrected with a vendor supplied TurboFLASH B_1 mapping sequence [29]. The flip angles used were (5°, 8°, 11°, 15°, 20°, 24°) and the TR was 10 ms for both the UTE and standard GRE sequence. The TurboFLASH B_1 mapping method is characterized by a slice-selective preconditioning pulse that precedes the FLASH acquisition. This slice-selective pre-pulse was acquired with a nominal flip angle of 80°, whereas the FLASH acquisition used a flip angle of 8°. Other acquisition parameters that were kept consistent between the VFA, AFI and Cartesian GRE acquisition were $(2 \times 2 \times 2)$ mm^3 isotropic resolution with an acquisition matrix size of $64 \times 64 \times 64$.

2.5. Comparison with literature

In a subsequent phantom experiment using the tubes with nominal T_1 values of 450 ms and 1200 ms, those combinations of TRs and spoiler gradients that had provided the most stable quantitative T_1 results in the previous AFI measurements were compared with existing methods proposed in the literature. These methods included: (I) constant spoiling in z-direction and TR_1/TR_2 of 20/100 ms to accommodate the large gradient areas of 447/2236 ms·mT/m [18,22]; (II) randomized RF phase and constant spoiling along the z-direction [30,31], (III) random spoiling along the z-direction [32], and (IV) randomized RF phase with additional randomized spoiling along the z-direction [33]. Table 2 summarizes these methods and the abbreviations used to refer to them in the following. The implementation of the methods (III) and (IV) required additional sequence modifications to allow for both randomized spoiling along the z-direction and a random RF phase value at the end of each TR. Furthermore, the measurements with method (IV) were

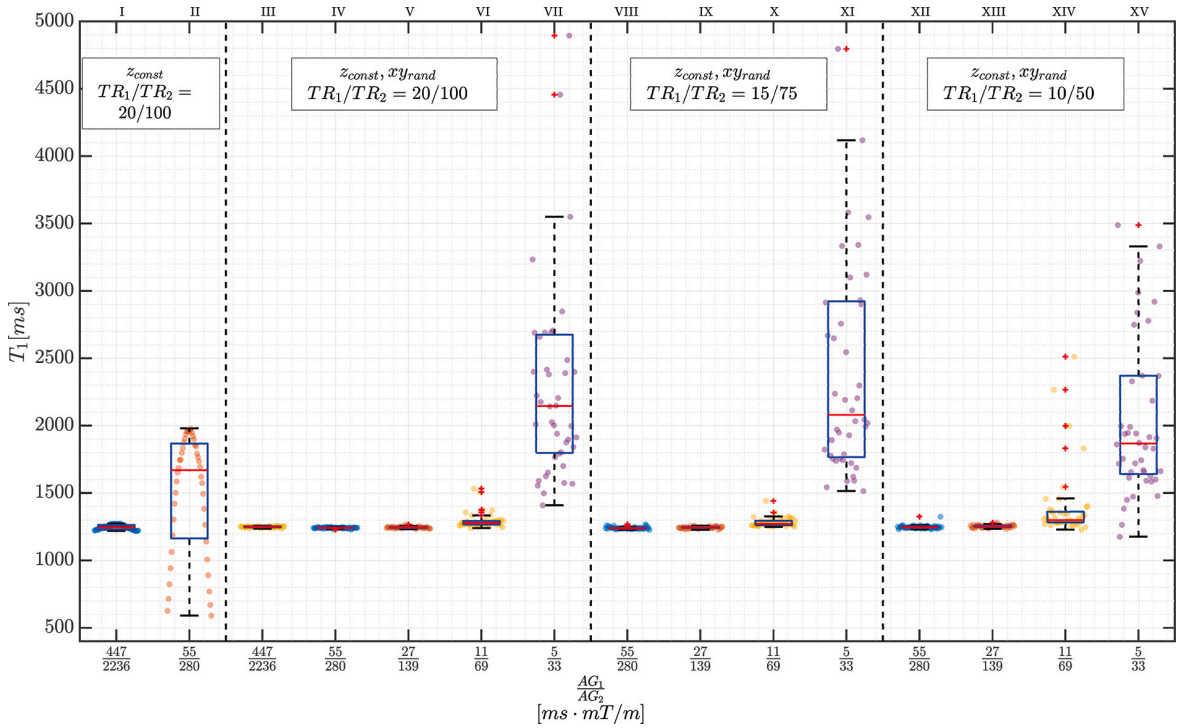

Fig. 2. Boxplots of the estimated T_1 relaxation times for different repetition time combinations (TR_1/TR_2) and gradient spoiling schemes (AG_1/AG_2). The different values for the RF phase increment (ranging from 0° to 180° with a step size of 4°) are visualized as horizontal spread within each block. Results are shown for the tube with water doped with a concentration of 0.19 mM Gadovist (nominal T_1 = 1200 ms). The dashed vertical black lines separate the different measurements by grouping them according to the spoiling scheme and the TRs used for the acquisition (see also Table 1).

repeated 45 times in order to test the robustness and repeatability of the RF phase randomization. Both the proposed method (V) and the methods from the literature (I–IV) were used to acquire AFI maps and correct VFA-based T_1 quantification performed with the corresponding TRs and acquisition parameters as described before using the same phantom.

Further sequence parameters, specific for all AFI phantom experiments, were $n = TR_2/TR_1$ of 5, FA of 45° and 600 dummy cycles. For both the AFI and VFA acquisitions, an isotropic spatial resolution of (2.5 × 2.5 × 2.5) mm^3 with an acquisition matrix size of 48 × 48 × 48, 1200 Hz/pixel bandwidth, and 100 μs pulse duration was chosen.

For comparison, 2D multi-slice inversion recovery data were acquired using a vendor-supplied Cartesian sequence to generate T_1 maps of the phantom as ground truth. The inversion times used were: 50 ms, 100 ms, 200 ms, 300 ms, 400 ms, 500 ms, 800 ms, 1200 ms, 1800 ms, 2500 ms, 3000 ms, 3900 ms. Other acquisition parameters were (0.6 × 0.6 × 1) mm^3 anisotropic resolution and TR of 16 s.

2.6. In vivo experiment

As a proof of concept, an AFI-based B_1 correction map was created to correct the VFA-based T_1 estimates in the knee of a 27-year-old healthy volunteer with no known pathologies after the subject provided written informed consent following the institutional ethics committee guidelines. The knee is a good candidate for validation of our proposed method because it contains tissues with a wide range of T_1 values originating from short T_2* species that can only be quantified with UTE, such as tendons and cortical bone, but also from longer T_2* tissues such as muscle, fatty tissue and bone marrow. A vendor supplied gradient echo sequence was used for VFA-based T_1 mapping as a comparison of the proposed UTE AFI method, and a TurboFLASH B_1 map with the same acquisition parameters as in the "short T_2* phantom" experiment was used to correct the standard GRE VFA acquisition. The VFA dataset was acquired with 6 different flip angles (5°, 8°, 12°, 14°, 22°, 25°) and TR = 10 ms, while the AFI-sequence parameters were TR_1/TR_2 = 10/50 ms (*i.e.*, n = 5), flip angle = 45°, and dummy cycles = 600. All datasets were acquired with the same anisotropic resolution of (1.8 × 1.8 × 3.8) mm^3.

3. Results

3.1. Phantom experiments

Boxplots of T_1 relaxation times for the tube with a nominal T_1 value of 1200 ms are shown in Fig. 2 for the different TR combinations, gradient spoiling schemes and RF phase increment values. With the largest values for AG_1 and AG_2 of 447 mT·ms/m and 2236 mT·ms/m, respectively, and TR_1/TR_2 of 20/100 ms (ratio n = 5), as suggested by Yarnykh [18], a small residual dependence of T_1 on the RF phase increment was observed (I). As expected and known from literature, a reduction of the gradient area values (with almost unchanged ratio) led to a significantly stronger dependence of T_1 on the RF phase increments (II). With additional randomized spoiling in x- and y-direction, this phase increment dependence was effectively eliminated, resulting in a consistent T_1 estimation independent of φ (III). Most importantly, this observation persisted as AG_1 and AG_2 were progressively reduced to 27 mT·ms/m and 139 mT·ms/m (IV & V). The latter values are a factor of 16 smaller than the original spoiling values suggested by Yarnykh [18] (I). With further reduction of the gradient pulse areas down to 11 mT·ms/m and 69 mT·ms/m (VI) or even lower (VII), the variations in T_1 again became strongly dependent on the RF spoiling phase increment. When reducing the repetition times TR_1 and TR_2 to values of 15 ms and 75 ms (VIII to XI) or 10 ms and 50 ms (XII to XV) while applying the same spoiling gradients as in scans IV to VII, the same effects in T_1 variation were observed. These results suggest that TR_1 and TR_2 in the AFI-sequence can be reduced to 10 ms and 50 ms and the spoiling gradient pulse areas to 27 mT·ms/m and 139 mT·ms/m, respectively,

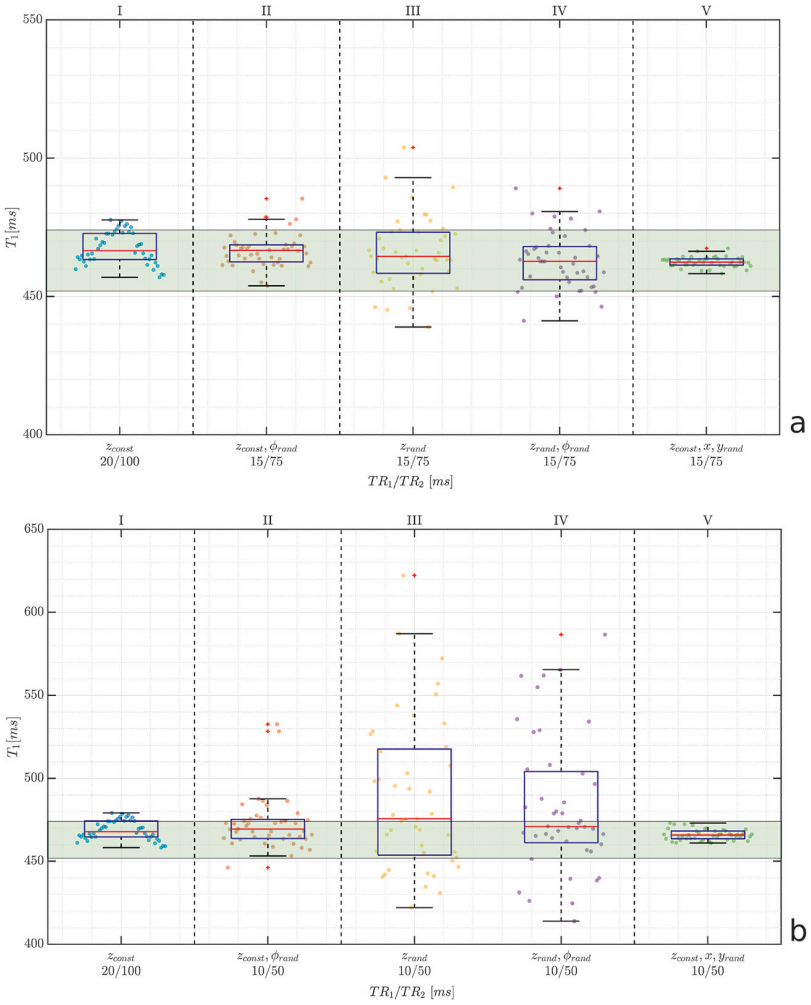

Fig. 3. Estimated T_1 relaxation times for TR_1/TR_2 and AG_1/AG_2 ratios of (a) 15/75 ms and 55/280 mT·ms/m and (b) 10/50 ms and 22/111 mT·ms/m, along with the reference with TR_1/TR_2 and AG_1/AG_2 ratios of 20/100 ms and 447/2236 mT·ms/m. Results shown are calculated for the tube containing 0.6 mM Gadovist (nominal T_1 = 450 ms). From left to right are shown different spoiling schemes as proposed in the literature (the rightmost panel presents the results of the method proposed in this work). The different values for the RF phase increment (ranging from 0° to 180° with a step size of 4°) or the repeated acquisitions for the measurements with random RF phase are visualized as horizontal spread within each block. The green colored area in (a) and (b) indicates the reference T_1 value obtained from the inversion recovery sequence including a single standard variation over the used ROI as width. (For interpretation of the references to colour in this figure legend, the reader is referred to the web version of this article.)

Table 3
Summary of T_1 estimates after AFI B_1 correction for the tubes of the phantom for the different methods used. Each column corresponds to a method (see Table 2), with the rightmost column showing the results of the inversion recovery method used as ground truth. The results are given as mean value ± std. (in ms) derived from corresponding regions-of-interest (ROIs). The upper part of the table refers to the experiment with TR_1/TR_2 and AG_1/AG_2 ratios of 15/75 and 55/280 (see Fig. 3a), while the lower part refers to the experiment with TR_1/TR_2 and AG_1/AG_2 of 10/50 and 22/111 (see Fig. 3b).

TR_1/TR_2 = 15/75, AG_1/AG_2 = 55/280						
Method tube	I z_{const}	II z_{rand}, ϕ_{rand}	III z_{rand}	IV z_{const}, ϕ_{rand}	V z_{const}, xy_{rand}	Inv-Rec
1	467 ± 6	465 ± 6	465 ± 12	462 ± 9	462 ± 2	463 ± 7
2	1174 ± 18	1193 ± 27	1185 ± 80	1165 ± 57	1165 ± 6	1176 ± 18
TR_1/TR_2 = 10/50, AG_1/AG_2 = 22/111						
Method Tube	I z_{const}	II z_{rand}, ϕ_{rand}	III z_{rand}	IV z_{const}, ϕ_{rand}	V z_{const}, xy_{rand}	Inv-Rec
1	468 ± 6	472 ± 15	488 ± 44	482 ± 40	465 ± 3	463 ± 7
2	1167 ± 18	1203 ± 42	1279 ± 120	1298 ± 117	1174 ± 12	11 76 ± 18

while maintaining the independence of the T_1 estimate from the RF phase increment and providing results comparable to the highest gradients amplitudes and longest TR values. Ultimately, this leads to significantly shorter total acquisition times (a scan acquired with TR 20 ms takes 6.58 min, whereas a scan acquired with TR 10 ms requires only 3.29 min). We also tested sequences with lower gradient areas and different TR combinations (see VI, VII, X, XI, XIV, XV), but these were considered too unstable due to the large fluctuation in the estimation of the T_1 values.

Fig. 3 displays the T_1 results for the different spoiling methods reported in the literature for the phantom tube with a nominal T_1 value of 450 ms for two different combinations of AG_1/AG_2 and TR_1/TR_2 (Fig. 3a and b; see also Table 3 for a summary of the results for both phantom tubes). Both parameter combinations were compared with the reference [18] (first panel in Fig. 3). The methods (II, IV) with randomized RF phase increments, ϕ_{rand}, still show significant fluctuations of T_1 between the different repetitions of the measurements, which is more pronounced for the lower gradient pulse areas in Fig. 3b and reflected in the increased standard deviation of the estimated T_1 values (Table 3) compared to the corresponding values in Fig. 3a. In contrast, the proposed z_{const}, xy_{rand} method with constant spoiling in randomized directions in the x-y-plane (V) not only effectively eliminated the RF phase increment dependence of the T_1 estimation, but also provided quantitative results with a maximum error of 2%. Furthermore, the results obtained by the proposed method (V) were in good agreement with the T_1 values of the conventional inversion recovery sequence used as

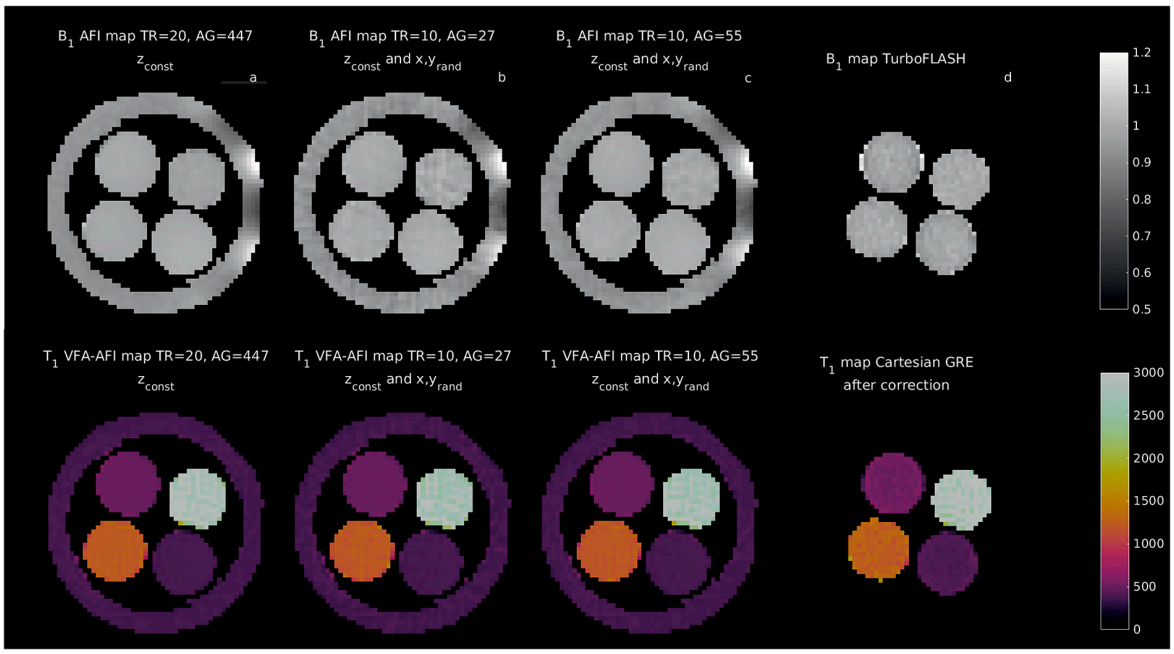

Fig. 4. *Top row*: B_1 maps of the "short T_2* phantom". The first three maps (a-c) are based on a UTE AFI sequence, while the last map (d) was derived from a conventional GRE acquisition. *Bottom row*: Corresponding T_1 maps derived from the UTE and GRE acquisitions. The UTE AFI maps were acquired with (a) z_{const}, $TR_1/TR_2 = 20/100$ ms and $AG_1/AG_2 = 447/2236$ mT·ms/m; (b) z_{const}, xy_{rand}, $TR_1/TR_2 = 10/50$ ms and $AG_1/AG_2 = 27/130$ ms·mT/m; and (c) z_{const}, xy_{rand}, $AG_1/AG_2 = 55/280$ ms·mT/m, respectively.

Table 4
Summary of T_1 values extracted from different ROIs in the "short T_2* phantom" after B_1-field correction for both the AFI method and standard Cartesian GRE. All the results are quoted as mean ± std. dev. and provided in ms.

Tissue	UTE T_1 VFA-AFI $\mathbf{z_{const}}$, AG_1/AG_2 = 447/2236	UTE T_1 VFA-AFI $\mathbf{z_{const}}$, $\mathbf{xy}_{rand}$ AG_1/AG_2 = 27/130	UTE T_1 VFA-AFI $\mathbf{z_{const}}$, $\mathbf{xy}_{rand}$ AG_1/AG_2 = 55/280	GRE T_1 VFA After B_1 correction
Tube 1 (0.5 mM)	497 ± 3	496 ± 5	496 ± 3	505 ± 32
Tube 2 (0.04 mM)	2868 ± 157	2852 ± 189	2840 ± 152	2851 ± 347
Tube 3 (0.6 mM)	388 ± 3	387 ± 4	387 ± 3	385 ± 13
Tube 4 (0.19 mM)	1224 ± 22	1212 ± 32	1218 ± 24	1234 ± 50
Tape	378 ± 12	375 ± 16	374 ± 12	–

ground truth. This is true for both gradient and TR combinations chosen according to the optimization experiment.

3.2. Comparison with other B_1-mapping techniques

Fig. 4 shows, in the top row, the B_1 maps for the "short T_2* phantom". The first three B_1 maps were obtained using the UTE AFI method. Here, the implementation proposed by Yarnykh [18] is compared with two different gradient combinations of our proposed method (27/130 ms·mT/m and 55/280 ms·mT/m, respectively). The AFI maps were smoothed with a Gaussian filter of 2×2 mm^2 [34]. The last map is the result from a vendor supplied TurboFLASH B_1 mapping sequence. The bottom row shows the B_1 corrected T_1 maps for both the AFI and regular GRE acquisition. For both the B_1 and T_1 maps, it is apparent that UTE sequences, while able to retrieve signals in short T_2* species (in this case, the circular roll of tape around the tubes) where standard GRE acquisition fails, still provide robust T_1 quantification in agreement with more conventional sequences. Results for T_1 quantification in each tube can be found in Table 4. A comparison of the two B_1 maps obtained with the proposed implementation of the AFI method reveals slightly higher level of noise for the map obtained with a lower gradient combination (27/130 ms·mT/m), which is reflected in the slightly increased standard deviation values for the calculated T_1. Although this does not significantly affect the B_1 correction and subsequent T_1 quantification, it can be speculated that this reduction of SNR stems from the reduction in the acquisition TRs.

3.3. In vivo experiment

Fig. 5 shows T_1 maps (before and after B_1 correction) of a midsagittal slice of the knee together with the corresponding B_1 maps of the same slice. The top row shows the result from a conventional acquisition, while the bottom row represents the UTE results corrected by the proposed method. The lower T_1 values toward the edge of the FoV in the uncorrected maps (*left*) are corrected by applying the B_1 correction (*center*) for both the standard and UTE acquisition. However, it is visible that the conventional acquisition contains erroneous values for the B_1 map in the short T_2* tissues (such as tendons and cortical bone), whose values appear abnormally high, resulting in an incorrect estimate of the T_1 of such tissues. T_1 values were determined in several selected regions-of-interest (ROIs) and are listed in Table 5 and compared with literature values.

4. Discussion and conclusion

The addition of randomized x-y-spoiling to the AFI-sequence resulted in a more consistent T_1 estimate independent of the RF phase increment compared to other methods previously presented in the literature. At the same time, smaller spoiling gradients could be used, which allowed us to reduce TR, which is not possible with the very large spoiling gradients proposed by Yarnykh [18]. This resulted in a significant reduction of

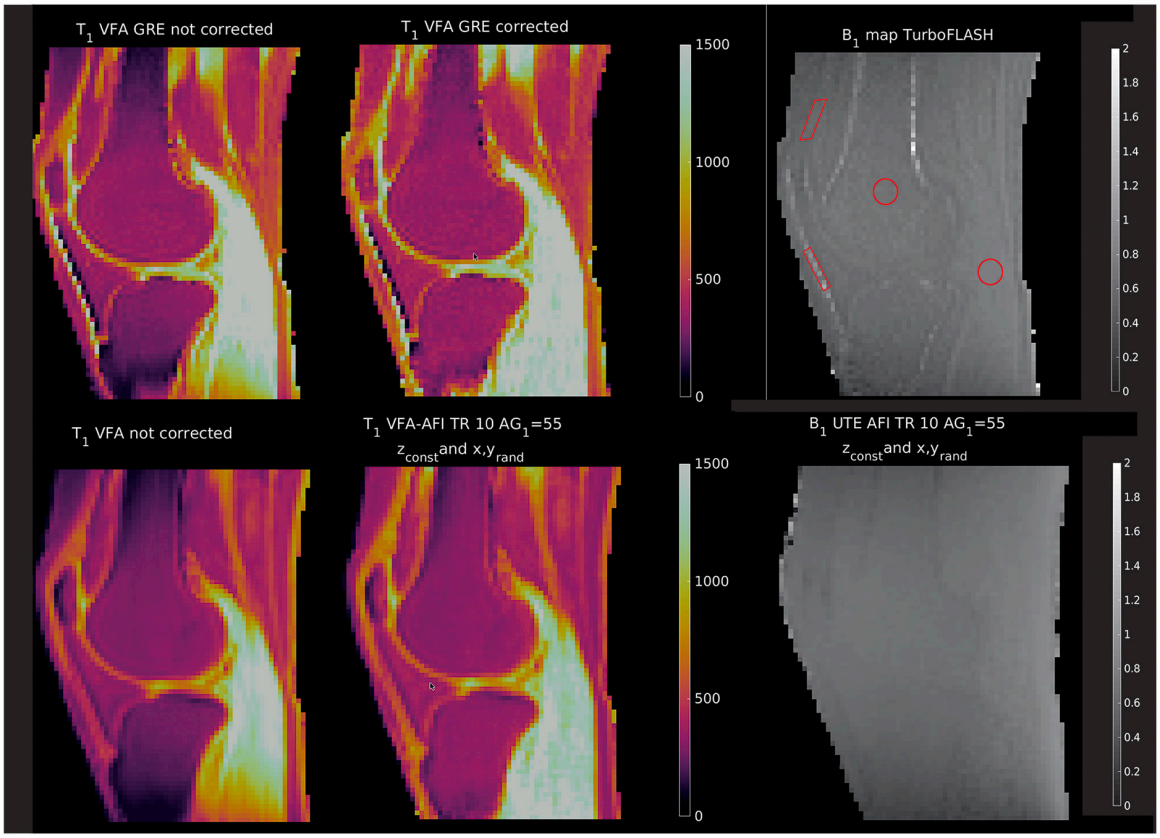

Fig. 5. *Left*: T_1 maps before B_1 correction of a VFA knee image of a 27-year-old volunteer (conventional acquisition in the top row, UTE-based acquisition in the bottom row). *Center*: T_1 maps after B_1 correction (scaled between 0 ms and 1500 ms). *Right:* B_1 correction maps acquired with vendor supplied TurboFLASH acquisition *(top row)* and with the proposed z_{const}, xy_{rand}AFI method acquired with $TR_1/TR_2 = 10/50$ ms and $AG_1/AG_2 = 55/280$ ms·mT/m *(bottom row)*. ROIs used to extract representative T_1 values are superimposed on the TurboFLASH B_1 map.

Table 5
Summary of T_1 values extracted from different ROIs in the knee of a volunteer before and after B_1-field correction. All values are quoted as mean ± std. dev. and given in ms.

Tissue	UTE T_1 VFA	UTE T_1 VFA-AFI	GRE T_1 VFA	GRE T_1 VFA	T_1 from literature
	Before AFI correction	$\mathbf{z_{const}}$, $\boldsymbol{xy}_{rand}$ $TR_1/TR_2 = 10/50$	Before B_1 correction	After B_1 correction	
Patellar tendon	600 ± 59	640 ± 56	1103 ± 620	1135 ± 950	~ 637 [34]
Quadriceps tendon	592 ± 30	768 ± 38	766 ± 189	908 ± 223	~ 779 [34]
Bone marrow	313 ± 5	337 ± 8	332 ± 16	335 ± 21	~ 135 [35] – 381 [36]
Muscle	1424 ± 112	1411 ± 156	1544 ± 162	1442 ± 138	~1256 [36] – 1420 [37]

acquisition time by a factor of up to two, while the estimation accuracy of T_1 still remained in an acceptable range (below 2% error).

The reason why our proposed method is more stable is due to both the specific acquisition scheme and the additional randomization implemented in the x-y-plane spoiling. In the literature, only constant and random z-spoiling have been previously combined with either constant or random RF phase increments [30–33]. This differs from our method proposed here, where constant z-spoiling acting in one spatial direction was combined with additional randomized spoiling in the x-y-plane to effectively destroy residual transverse magnetization. One difference from other studies using randomized spoiling [32,33] is that in our work only the direction, but not the strength of the spoiling gradients was randomized. We implemented and tested the proposed randomized x-y-gradient spoiling for a 3D radial center-out UTE acquisition. Although it seems plausible that the proposed method also works for Cartesian sequences, it has been shown [33] that the center-out implementation of the 3D-UTE sequence is beneficial for the added randomized x-y spoiling and thus could contribute to the stability of the method. This is because from radially acquired data, the reconstructed k-space is obtained by combining data from readouts that all pass through the center of k-space, effectively averaging smaller signal fluctuations. This potentially adds increased protection to the 3D AFI-based B_1-field correction against artifacts that could have resulted from the additional randomization due to x-y-spoiling.

Our method of AFI-based B_1-field correction was also applied to knee data *in vivo*, where the effect of the correction was clearly seen. The corrected T_1 values were quantitatively consistent with current literature [34–38], including short T_2* tissues such as tendons and ligaments. Since UTE-AFI has emerged as one of the few methods capable of providing B_1 correction for short T_2* species *in vivo* [34], the ability to reduce acquisition time while maintaining the accuracy of T_1 estimation may lead to wider application of UTE-based T_1 quantification sequences.

In conclusion, the proposed method is able to achieve stable B_1 mapping to correct VFA-based T_1 estimation and outperforms alternative methods in the literature in terms of acquisition time. In our setting, we were able to reduce the latter by half. Further studies are needed and

should be performed to explore the scope of the method and to better understand the relationship between randomized x-y-spoiling and 3D radial radial-out k-space acquisition.

Acknowledgements

This work was supported by a graduate scholarship from the Friedrich-Schiller-University Jena and the state of Thuringia (Landesgraduiertenstipendium) and the German Research Foundation (DFG, RE 1123/22-1).

References

[1] Chan DD, Neu CP. Probing articular cartilage damage and disease by quantitative magnetic resonance imaging. J R Soc Interface 2013;10. https://doi.org/10.1098/rsif.2012.0608.
[2] Carlier PG, Azzabou N, de Sousa PL, Hicks A, Boisserie J-M, Amadon A, et al. Skeletal muscle quantitative nuclear magnetic resonance imaging follow-up of adult Pompe patients. J Inherit Metab Dis 2015;38:565–72. https://doi.org/10.1007/s10545-015-9825-9.
[3] Mittal S, Pradhan G, Singh S, Batra R. T_1 and T_2 mapping of articular cartilage and menisci in early osteoarthritis of the knee using 3-tesla magnetic resonance imaging. Pol J Radiol 2019;84:e549–64. https://doi.org/10.5114/pjr.2019.91375.
[4] Ramos-Llordén G, Vegas-Sánchez-Ferrero G, Björk M, Vanhevel F, Parizel PM, San José Estépar R, et al. NOVIFAST: a fast algorithm for accurate and precise VFA MRI T_1 mapping. IEEE Trans Med Imaging 2018;37:2414–27. https://doi.org/10.1109/TMI.2018.2833288.
[5] Boudreau M, Tardif CL, Stikov N, Sled JG, Lee W, Pike GB. B_1mapping for bias-correction in quantitative T_1 imaging of the brain at 3T using standard pulse sequences. J Magn Reson Imaging 2017;46:1673–82. https://doi.org/10.1002/jmri.25692.
[6] Stikov N, Boudreau M, Levesque IR, Tardif CL, Barral JK, Pike GB. On the accuracy of T_1mapping: searching for common ground. Magn Reson Med 2015;73:514–22. https://doi.org/10.1002/mrm.25135.
[7] E.K. Insko, L. Bolinger,. Mapping of the radiofrequency field. J Magn Reson A n.d.; 103:82–5. doi:https://doi.org/10.1006/jmra.1993.1133.
[8] Cunningham CH, Pauly JM, Nayak KS. Saturated double-angle method for rapid B_1+ mapping. Magn Reson Med 2006:1326–33.
[9] Stollberger R, Wach P. Imaging of the active B_1 field in vivo. Magn Reson Med 1996;35:246–51. https://doi.org/10.1002/mrm.1910350217.
[10] Morrell GR. A phase-sensitive method of flip angle mapping. Magn Reson Med 2008;60:889–94. https://doi.org/10.1002/mrm.21729.
[11] Sacolick LI, Wiesinger F, Hancu I, Vogel MW. B1 mapping by Bloch-Siegert shift. Magn Reson Med 2010;63:1315–22. https://doi.org/10.1002/mrm.22357.
[12] Corbin N, Acosta-Cabronero J, Malik SJ, Callaghan MF. Robust 3D Bloch-Siegert based B_1+ mapping using multi-echo general linear modeling. Magn Reson Med 2019;82:2003–15. https://doi.org/10.1002/mrm.27851.
[13] Wang J, Qiu M, Constable RT. In vivo method for correcting transmit/receive nonuniformities with phased array coils. Magn Reson Med 2005;53:666–74. https://doi.org/10.1002/mrm.20377.
[14] Robson MD, Bydder GM. Clinical ultrashort echo time imaging of bone and other connective tissues. NMR Biomed 2006;19:765–80. https://doi.org/10.1002/nbm.1100.
[15] Jerban Saeed, Ma Yajun, Wong Jonathan H, Nazaran Amin, Searleman Adam, Wan Lidi, et al. Ultrashort echo time magnetic resonance imaging (UTE-MRI) of cortical bone correlates well with histomorphometric assessment of bone microstructure. Bone 2019;123:8–17. https://doi.org/10.1016/j.bone.2019.03.013.
[16] Krämer M, Herzau B, Reichenbach JR. Segmentation and visualization of the human cranial bone by T_2* approximation using ultra-short echo time (UTE) magnetic resonance imaging. Z Med Phys 2020;30:51–9. https://doi.org/10.1016/j.zemedi.2019.06.003.
[17] Yarnykh VL. Actual flip-angle imaging in the pulsed steady state: a method for rapid three-dimensional mapping of the transmitted radiofrequency field. Magn Reson Med 2007;57:192–200. https://doi.org/10.1002/mrm.21120.
[18] Yarnykh VL. Optimal radiofrequency and gradient spoiling for improved accuracy of T_1 and B_1 measurements using fast steady-state techniques. Magn Reson Med 2010;63:1610–26. https://doi.org/10.1002/mrm.22394.
[19] Nehrke K, Börnert P. DREAM—a novel approach for robust, ultrafast, multislice B1 mapping. Magn Reson Med 2012;68:1517–26. https://doi.org/10.1002/mrm.24158.
[20] Yarnykh VL. Effect of the phase increment on the accuracy of T_1 measurements by the variable flip angle method using a fast RF spoiled gradient echo sequence. In: Proceedings of the 15th Annual Meeting of ISMRM, Berlin, Germany; 2007 (Abstract 1796) n.d.:1.
[21] Yarnykh VL. Improved accuracy of variable flip angle T_1measurements using optimal radiofrequency and gradient spoiling. In: Proceedings of the 16th Annual Meeting of ISMRM, Toronto, Ontario, Canada; 2008 (Abstract 234) n.d.:1.
[22] Yarnykh VL. Optimal spoiling of the transverse magnetization in the Actual Flip-angle Imaging (AFI) sequence for fast B1 field mapping. In: Proceedings of the 16th Annual Meeting of ISMRM, Toronto, Ontario, Canada; 2008 (Abstract 3090) n.d.:1.
[23] Nehrke K. On the steady-state properties of actual flip angle imaging (AFI). Magn Reson Med 2009;61:84–92. https://doi.org/10.1002/mrm.21592.
[24] Benner T, van der Kouwe AJW, Kirsch JE, Sorensen AG. Real-time RF pulse adjustment for B0 drift correction. Magn Reson Med 2006;56:204–9. https://doi.org/10.1002/mrm.20936.
[25] Bloch F. Nucl Induct Phys Rev 1946;70:460–74. https://doi.org/10.1103/PhysRev.70.460.
[26] Krämer M, Motaal AG, Herrmann K-H, Löffler B, Reichenbach JR, Strijkers GJ, et al. Cardiac 4D phase-contrast CMR at 9.4 T using self-gated ultra-short echo time (UTE) imaging. J Cardiovasc Magn Reson 2017:19. https://doi.org/10.1186/s12968-017-0351-9.
[27] Krämer M, Maggioni MB, Brisson NM, et al. T_1 and T_2* mapping of the human quadriceps and patellar tendons using ultra-short echo-time (UTE) imaging and bivariate relaxation parameter-based volumetric visualization. Magn Reson Imaging 2019:29–36. https://doi.org/10.1016/j.mri.2019.07.015.
[28] Kirsch S, Schad LR. Single-slice mapping of ultrashort T2. J Magn Reson 2011;210:133–6. https://doi.org/10.1016/j.jmr.2011.02.003.
[29] Chung S, Kim D, Breton E, Axel L. Rapid B1+ mapping using a preconditioning RF pulse with TurboFLASH readout. Magn Reson Med 2010;64:439–46. https://doi.org/10.1002/mrm.22423.
[30] Freeman R, Hill HDW. Phase and intensity anomalies in Fourier transform NMR. J Magn Reson 1971:366–83. https://doi.org/10.1016/0022-2364(71)90047-3.
[31] Zur Y, Wood ML, Neuringer LJ. Spoiling of transverse magnetization in steady-state sequences. Magn Reson Med 1991;21:251–63. https://doi.org/10.1002/mrm.1910210210.
[32] Darrasse H, Mao L, Darrasse L. Steady-state management in fast low-angle imaging. In: Proceedings of the 5th Annual Meeting of ISMRM, Toronto, Montreal, Canada; 1986 (Abstract 234) n.d.:1.
[33] Lin W, Song HK. Improved signal spoiling in fast radial gradient-echo imaging: applied to accurate T_1 mapping and flip angle correction. Magn Reson Med 2009;62:1185–94. https://doi.org/10.1002/mrm.22089.
[34] Ma Y-J, Zhao W, Wan L, Guo T, Searleman A, Jang H, et al. Whole knee joint T_1 values measured in vivo at 3T by combined 3D ultrashort echo time cones actual flip angle and variable flip angle methods. Magn Reson Med 2019;81:1634–44. https://doi.org/10.1002/mrm.27510.
[35] Wang G, El-Sharkawy AM, Edelstein WA, Schär M, Bottomley PA. Measuring T_2 and T_1 and imaging T_2 without spin echoes. J Magn Reson 2012;214:273–80. https://doi.org/10.1016/j.jmr.2011.11.016.
[36] Jordan CD, Saranathan M, Bangerter NK, Hargreaves BA, Gold GE. Musculoskeletal MRI at 3.0T and 7.0T: a comparison of relaxation times and image contrast. Eur J Radiol 2013;82:734–9. https://doi.org/10.1016/j.ejrad.2011.09.021.
[37] Gold GE, Han E, Stainsby J, Wright G, Brittain J, Beaulieu C. Musculoskeletal MRI at 3.0 T: relaxation times and image contrast. Am J Roentgenol 2004;183:343–51. https://doi.org/10.2214/ajr.183.2.1830343.
[38] Stanisz GJ, Odrobina EE, Pun J, Escaravage M, Graham SJ, Bronskill MJ, et al. T_1, T_2 relaxation and magnetization transfer in tissue at 3T. Magn Reson Med 2005;54:507–12. https://doi.org/10.1002/mrm.20605.

5.3 Assessment of training-induced changes of the lumbar back muscle using a multiparametric MRI protocol

Authors: M.B. Maggioni, R. Sibgatulin, M. Krämer, D. Güllmar, J.R. Reichenbach

Submitted for review to *NMR in Biomedicine*.

Assessment of training-induced changes of the lumbar back muscle using a multiparametric MRI protocol

Marta B. Maggioni[1], Renat Sibgatulin[1], Martin Krämer[1,2], Daniel Güllmar[1], Jürgen R. Reichenbach[1,]

[1] Medical Physics Group, Institute of Diagnostic and Interventional Radiology, Jena University Hospital – Friedrich-Schiller-University Jena, Germany
[2] Institute of Diagnostic and Interventional Radiology, Jena University Hospital – Friedrich Schiller University Jena, Germany

Total word Count=5177 (including abstract and appendix)

Abstract

Adaptations in muscle physiology due to long-term physical training have been monitored using a variety of methods: ranging from invasive techniques, such as biopsy, to less invasive approaches such as electromyography (EMG), to a variety of quantitative magnetic resonance imaging (qMRI) parameters. Typically, these latter parameters are assessed immediately after exercise. In contrast, this work assesses such adaptations in a set of qMRI parameters obtained at rest in the muscles of the lumbar spine.

To this end, we developed a multiparametric measurement protocol to extract quantitative values of relaxation time constants T_2 and T_1, fat fraction, and IVIM diffusion parameters in the lumbar back muscle from the acquired data. The protocol was applied to 31 subjects divided into three differently trained cohorts: two groups of athletes (endurance athletes and powerlifters) and a control group with a relatively inactive lifestyle.

Significant differences in T_2, fat content, and perfusion fraction were found between the trained and untrained cohorts, while the components of the diffusion tensor provided additional differentiation between the two groups of athletes. The observed decrease in the axial diffusion and the trend of increasing radial diffusion in the strength-trained cohort, compared to the endurance-trained athletes, may be indicative of muscle hypertrophy.

In conclusion, the use of multiparametric information helps to provide new insights into the potential of quantitative MR parameters to detect and quantify long-term effects in differently trained cohorts, even at rest.

Keywords

qMRI, training, lumbar back muscle, diffusion, Bayesian estimation

Introduction

Physical activity and muscle training have several positive effects, such as improving cardiovascular health [1], increasing muscle resistance to fatigue [2], and reducing the risk of

developing diseases such as type II diabetes [3] or colorectal cancer [4]. The fact that consistent physical activity modifies skeletal muscle morphology is widely accepted [5], but assessing and quantifying these modifications usually requires invasive techniques such as biopsies. Biopsy-based studies have demonstrated significant adaptation of muscle tissue to long-term physical activity, including changes in muscle fiber type and size [6,7]. They have also successfully demonstrated distinct effects of different training regimens on muscle tissue [5,8].

A prominent non-invasive tool for studying the activation of muscle tissue is electromyography (EMG). EMG records the electrical activity that leads to muscle contraction [9] and has been shown to aid in both diagnosis and the study of muscle function, although caution should be exercised in interpreting it in terms of muscle force or timing of contraction [10]. A recent surface electromyography (SEMG) study observed a significant difference in muscle activation in subjects with different exercise routines [11]. In this study, both endurance athletes and controls performed better than strength athletes in a 10-minute back muscle endurance test at a load of 50% of upper body weight.

Possible long-term effects of regular training, detectable by EMG or biopsy, are less well-researched with quantitative magnetic resonance imaging (qMRI). There are only a few MRI-based studies on this topic [12–14], each generally focusing on only a few parameters, but highlighting the possible impact of exercise-induced muscle damage, affecting the transverse relaxation time T_2 and significant changes in the fat fraction between the trained and untrained cohorts [15].

T_2 has been shown to increase after exercise, and the origin of this phenomenon has been linked to an accumulation of osmolytes as a result of increased fluid influx [16,17]. Apparent diffusion coefficients (ADC) have also been shown to increase after exercise [18,19], which is thought to be due to the increase in fluid in muscles during and after a strenuous exercise session. Other studies, using Intra Voxel Incoherent Motion (IVIM) MRI sequences, have also demonstrated increased blood flow after exercise [20–22].

Two other MRI parameters that have been used to characterize muscle tissue morphology are fat content and T_1 relaxation time constant. Changes in T_1 immediately after exercise have been associated with increased blood perfusion and temperature [23,24], but the origin of this phenomenon is not fully understood. Furthermore, increased fat content has been associated with reduced power output per muscle unit and low back pain [25,26]. The level of fat infiltration into muscle tissue can be quantitatively assessed by MRI, exploiting the chemical shift between the proton signals of fat and water.

Most of the qMRI literature on skeletal muscle has focused on measuring changes in some well-established MRI quantitative parameters such as T_2 and diffusion immediately after a strenuous exercise session [17,18]. However, the long-term effects of regular physical activity on qMRI parameters appear to be relatively understudied [27].

To bridge this gap, we developed a multi-parametric protocol to comprehensively characterize back muscle morphology and to investigate whether the effects of long-term physical activity and type of training are reflected and detectable in changes in quantitative MRI parameters.

This protocol included both well-established parameters, such as T_2 and fat fraction, which have been used before to characterize skeletal muscle (even at rest), as well as less well-studied parameters such as T_1 and diffusion-related parameters.

The protocol was applied to the muscles of the lumbar spine rather than the more commonly investigated skeletal muscles of the calf and thigh. This choice was made because the lumbar back muscles are involved in nonspecific low back pain (NSLBP), which is one of the most common causes of disability worldwide [28]. The exact causes behind this condition are not yet fully understood, and although physical activity has been shown to be a viable treatment, there is still debate about which type of physical activity is most beneficial [29]. Evaluating long-term effects of training in healthy cohorts and at rest using the proposed protocol may pave the way for treatment monitoring in low back pain.

In this work, we show that although parameters such as T_2 and fat fraction can capture differences between trained and untrained cohorts even at rest, additional insights from diffusion coefficients and perfusion fraction values help to differentiate between different types of training.

Materials and methods

Participants

Three cohorts of male subjects were studied: Endurance athletes (long-distance runners and cyclists n=10), strength athletes (powerlifters, n=11), and a control group (n=10) with a non-athletic lifestyle. All subjects were between 20 and 30 years of age. The study was approved by the institutional ethics committee. All participants provided written informed consent. Athletes were recruited through advertisements in local sports clubs and gyms. They were considered eligible to participate if they trained at least four times per week. Control participants were not expected to exercise regularly and had largely inactive lifestyles that did not exceed normal daily activities. MRI scans were performed at rest and at least 48 hours after the last exercise session to exclude exercise-related parameter changes. Subjects underwent MRI examinations in supine position for approximately one hour.

MRI Protocol

The MRI protocol included sequences that allowed the determination of relaxation parameters (i.e., T_2 and T_1), fat content and IVIM parameter values. Quantitative T_2 values were determined using a turbo spin echo (TSE) sequence with 32 echo times ranging from 7 ms to 218 ms, while the T_1 relaxation time constants were determined using a variable flip angle (VFA) gradient echo sequence [30] with five different flip angles (5°, 11°, 18°, 24°, 32°). For accurate VFA-based T_1 determination, especially at higher field strengths and in areas where the RF signal is attenuated (e.g., lower lumbar and abdominal regions), correction of the B_1-field is essential, which was performed here by acquiring an additional B_1 calibration scan

using the Bloch-Siegert method [31]. Fat content was determined using a 2-point Dixon sequence [32] with echo times (TE) of 2.46 and 3.69 ms. The in-plane spatial resolution was (1.5 ×1.5) mm^2 for all sequences and the slice thickness was 3 mm (except for the TSE sequence, which used a slice thickness of 6 mm).

Diffusion-weighted images (DWI) were acquired with a multi-slice spin-echo EPI (echo planar imaging) sequence with TR/TE=1600/63 ms using four averages and three orthogonal directions of diffusion encoding aligned with the right-handed RAS system (each direction was repeated twice with opposite polarities). For each direction, the following 19 b-values were used: 0, 5, 15, 20, 30, 40, 45, 55, 60, 70, 75, 90, 105, 120, 135, 150, 300, 450, 600 s/mm^2. The resolution for the DWI data was (2.3 × 2.3 × 8) mm^3. SPectral Attenuated Inversion Recovery (SPAIR) fat saturation was used.

Multi-slice images (from L4 to L5) were acquired in axial orientation. The muscles included in the field of view were multifidus (MF), erector spinae (ES), psoas major, and quadratus lumborum. However, the latter two muscles could not be evaluated consistently due to artifacts caused by respiration and bowel motion and were excluded from the analysis. All measurements were performed with the vendor's spine coil on a 3T Magnetom Prisma fit scanner (Siemens Healthineers, Erlangen, Germany). The total acquisition time was 45 minutes. All relevant acquisition parameters can be found in Table 1 in the Appendix.

MRI data processing and analysis

Regions of interest (ROIs) were manually drawn to segment the multifidus and erector spinae muscles based on apparent diffusion coefficient (ADC) maps for each individual subject, avoiding fascia, connective tissue and subcutaneous fat. Given the absence of noticeable differences between the left and right sides across all participants, the voxels from both sides were pooled together.

The T_1, T_2 and fat fraction maps were calculated by fitting the expected physical signal model to the measured signals. For T_1 quantification, the values of the input flip angles were corrected using the B_1 maps prior to fitting [31]. Differences in T_1, T_2 and fat fraction between the sedentary, endurance and strength cohorts were tested using a non-parametric Wilcoxon signed-rank test. Statistical significance was considered at $p < 0.05$.

Preprocessing of the IVIM diffusion data included denoising (using Mrtrix3 [31]), averaging of the repetitions and geometric averaging of the opposite polarities of the diffusion gradients to correct for cross-terms between the imaging and diffusion gradients [32,35]. No corrections were made for susceptibility-induced distortions or eddy currents. Importantly, neither the full rank-2 diffusion tensor nor its eigenvectors could be reconstructed using the three orthogonal diffusion gradient directions. Instead, we considered the diagonal components of the diffusion tensor in the base spanned by the three applied gradient directions: anterior-posterior (AP), left-right (LR) and inferior-superior (IS). Although these three directions do not generally coincide with the eigenvectors of the diffusion tensor, we chose to use them in this work due to the predominant orientation of the muscle fibers in the back, to report the component associated

with the IS axis (D_z) as the *axial diffusion coefficient* (by analogy with the axial diffusivity defined through the principle eigenvalue of DTI, λ_1) and an average of the components associated with the AP axis (D_x) and the LR axis (D_y) as the *radial diffusion coefficient* $D_\perp = \left(D_x + D_y\right)/2$ (cf. radial diffusivity). To pool the data across the gradient encoding directions, we used the IVIM signal model, which assumes isotropic perfusion and anisotropic diffusion [36]:

$$S(b_i) = S_0 \left[f \ exp\left(-b_i D^*\right) + (1-f)\, exp\left(-b_i \, \underline{g_i}^T \, \widehat{D} \, \underline{g_i}\right) \right] \quad (1),$$

where $S(b_i)$ and S_0 are the signal intensities at the *i*th *b*-value and *b*=0, respectively, f is the perfusion fraction, D^* is the scalar perfusion coefficient, $\widehat{D}$ is the diffusion tensor, and $\underline{g_i}$ represents the direction of the *i*th diffusion gradient encoding. Given the choice of the gradient scheme in this study, the product $\underline{g_i}^T \, \widehat{D} \, \underline{g_i}$ reduces to either D_x, D_y or D_z component (cf. eq. A2).

IVIM fitting in back muscle and skeletal muscles in general is challenging due to the low perfusion fraction (<10%) [22]. For this reason, fitting of the IVIM signal model (Eq. 1) was performed after averaging the signal over each ROI, resulting in only one set of IVIM parameters per muscle and subject. Furthermore, we used partial pooling of data across subjects within each cohort using a multilevel Bayesian model [37–39]. $D_{x/y/z}$ were assigned cohort-level priors, which were also estimated from the data. This structure allowed data fitting procedures at the individual subject level to simultaneously benefit from the fitting of other subjects in the same cohort and inform a global posterior distribution at the cohort-level. Additionally, estimating such cohort-level posterior allows cohort comparisons to be performed simultaneously with model fitting.

The scalar perfusion coefficient, D^*, being the most challenging parameter to estimate reliably from the selected set of *b*-values, was pooled across all subjects without group discrimination. In contrast, S_0 as the intercept of a nonlinear regression proved to be sufficiently well-conditioned not to require hyper-priors. The full hierarchical model, together with the prior parameters, is given in equations A1–11 in Appendix A, where some of the methodological choices are explained in more detail.

It is worth noting that a number of publications have successfully applied hyper-priors (also known as shrinkage priors, as they can reduce the dispersion of individual estimates around the group mean) to regularize IVIM estimation, albeit at different levels, but mainly to regularize the fit per voxel within individual subjects [40–43]. The Bayesian model used in this work was defined in numpyro (0.13.0 [44]) and fitted using MCMC (see Appendix A for details). To compare IVIM parameters between groups, the effect size $\eta = (\mu_{cohort} - \mu_{control}) \,/\, \sqrt{(\sigma^2_{cohort} + \sigma^2_{control})/2}$ [45] was computed using samples from the posterior, and its marginal distribution was reported together with its 95% highest density interval (HDI) as a means of assessing significance consistently at the $\alpha = 5\%$ level mentioned above. Specifically, effects, for which more than 97.5 % of the posterior probability lies on one side of 0 are considered significant, by analogy with the two-sided t-test [45].

Results

Figure 1 shows example images and parameter maps from a single subject for all analyzed qMRI parameters of the proposed multi-parametric MR protocol. As shown in the top row of the figure, application of the B_1-field inhomogeneity correction removed large inhomogeneities in the T_1 map that might otherwise mask true T_1 differences between subjects. Despite such precautions, however, even after implementing B_1 correction, no significant difference in T_1 relaxation times was found between the cohorts (see Figure 2).

Figure 2 summarizes the results of the quantitative ROI analyses for both muscles and all cohorts, including the transverse and longitudinal relaxation parameters T_2 and T_1, as well as the fat percentage calculated using the 2-point Dixon approach. For both the multifidus and erector spinae muscles, control subjects had significantly higher T_2 values, whereas both athlete cohorts had significantly lower fat percentages compared to the control group, with particularly low fat percentages in the multifidus of the endurance cohort. The mean values of all quantified parameters for each group are shown in Table 2 in the Appendix.

Figure 3 shows the marginal posterior distributions of the cohort means of f and $D_{y/z}$ and the pooled D^*. The estimated perfusion fraction in both training cohorts ($f \approx 5-6\%$) was higher than that in controls ($f \approx 2-3\%$), with the erector spinae (ES) consistently showing higher perfusion than the multifidus (MF). Such a difference is most confidently identified between strength training and controls, as indicated by non-overlapping posterior maximum (maximum-a-posteriori, MAP) estimates and HDIs, and reflected in the effect sizes in Figure 4. Finally, the fact that the axial diffusion coefficient (D_z) reported in this work is still consistently higher than the radial diffusion coefficient, is consistent with the natural orientation of muscle fibers [46]. Note that while axial diffusivity $\lambda_1$is greater than the radial diffusivity $(\lambda_2 + \lambda_3)/2$ by definition, due to the sorting of the diffusion tensor eigenvalues, no such sorting takes place with regard to the diffusion coefficients D_z and $D_\perp$.

It should be emphasized that the spread of the distributions in Figure 3 represents the uncertainty in the estimation of the group means using the Bayesian statistical procedure employed. To place these group means in the context of the spread observed in each cohort, Figure 4 presents the effect sizes associated with each of the training cohorts for the perfusion fraction as well as the radial and axial diffusion coefficients. Based on the marginal posterior distribution of the effect sizes, it is reasonable to assume that perfusion fraction and the axial diffusion coefficient were significantly different in the strength cohort compared to the control cohort. Besides, the perfusion fraction showed an increase (although not statistically significant) in both muscles and cohorts with a substantial MAP effect size of 0.7–1.0. Both radial and axial diffusion coefficients show consistent trends in both regions of interest. The radial diffusion coefficient tends to be increased in the strength training cohort compared to both the controls and the endurance athletes (the two of which show approximately the same $D_\perp$ values). The axial diffusion coefficient, on the other hand, when compared to controls

shows different trends in the two athlete cohorts: the endurance cohort shows an increase in D_z (with an effect size of 0.3–0.8 [-0.6, 1.7]), whereas the strength cohort shows a decrease, which is especially evident in the erector spinae (η_{D_z} of -1 [-2.3, -0.3] in ES).

Discussion

Among the numerous musculoskeletal studies using MRI, our study appears to be the first, to the best of our knowledge, to use a comprehensive multiparametric MRI protocol to investigate the long-term effects of different exercise conditions on MRI parameters determined in the lumbar spine at rest. There are a limited number of studies conducted at rest, but they have either focused on only selected parameters at a time, such as T_2 and diffusion or T_1 and T_2, or on athlete cohorts without including a control group [14], or by considering only a single athlete group [13,27] without including a differently trained cohort. Based on the synopsis and analysis of the different parameters (i.e., T_1 and T_2 relaxation times, fat fraction and IVIM-based diffusion parameters), our results suggest that these parameters, with the exception of the longitudinal relaxation time constant T_1, can be used to identify physiological and tissue differences of the lumbar back muscle under different regular training conditions.

Although transverse relaxation time T_2 and fat fraction alone could not distinguish between the two differently trained cohorts, the addition of the IVIM-based parameters perfusion fraction and diffusion coefficient helped to highlight differences between the two cohorts of athletes. In contrast, as mentioned above, no differences in T_1 relaxation time were found between the three groups. The control group showed a slightly (although not significantly) shorter T_1 value, which could be explained by the higher fat content of this cohort, as the T_1 relaxation time of fat is significantly shorter than that of muscle. Thus, the discriminative power of the T_1 parameter between the different conditions may not be sufficient to detect training-induced changes in healthy lumbar muscles under resting conditions.

The observation of lower T_2 values in the athletes is consistent with the findings of Le Rumeur *et al*. [11] and Sun *et al*. [12], but contradicts those of Keller *et al*. [27] who examined the calf muscle of sedentary controls and compared them to triathletes at rest (and after exercise). They reported higher T_2 values in the endurance athletes at rest. However, it should be emphasized that all these results were obtained in leg skeletal muscles, which tend to have a lower fat content than the back muscles studied in this work [15].

The higher fat content in the control cohort is in line with the work of Emanuelsson *et al*. [15] who evaluated the multifidus and erector spinae as a single ROI. It is worth noting that such a difference in fat content may affect other parameters such as T_2, as higher fat content has been shown to correlate with higher T_2 in other types of skeletal muscle [47] and is expected to increase the apparent T_2 in a multi-compartment model [48].

IVIM parameters were fitted using a hierarchical Bayesian model that pooled data from individual subjects within their respective groups by imposing learnable hyper-priors. Such a design allowed to regularize the individual subject fits and to perform the group comparison at

the same time. Both athlete cohorts showed an increasing trend in perfusion fraction f, consistent with previous results in leg muscles [49] and suggesting increased capillary density and perfusion as a long-term consequence of training. Notably, the perfusion fraction in the strength cohort appears to be consistently higher across both ROIs, which may be a consequence of the targeted repeated exercises that powerlifters perform with the lumbar back muscle. Interestingly, the endurance cohort also shows an increase in f in each ROI, corresponding to the effect size of 0.7 [-0.3, 1.8]. Although this result is not significant (in the sense defined above), it suggests a possible effect of non-targeted training on perfusion and appears to be in agreement with Hoier *et al.* [50].

Strength athletes consistently showed increased perfusion fraction and T_2 values for both muscles compared to endurance athletes. This trend of correlation between T_2 and perfusion fraction has frequently been shown in post-exercise results [22,51] and has been attributed to an accumulation of osmolytes as a result of increased fluid influx [16,17]. However, the fact that these results were obtained at rest suggests that this explanation may not fully capture the biological processes behind this phenomenon. In contrast, the sedentary subjects had elevated T_2 values and lower values of *f*, suggesting that the T_2 values in this group may have been influenced by the higher fat content in particular. The athlete cohorts, on the other hand, had comparable fat content, which allowed to highlight the aforementioned positive correlation between T_2 and *f*.

The two diffusion coefficients paint a more nuanced picture of different effects across cohorts and muscles. Specifically, while $D_\perp$ shows an increasing trend that is most pronounced in the strength-training group, D_z shows effects of different sign in the two cohorts. In general, DWI has been shown to be sensitive to microstructural alterations and adaptations in muscle tissue [52], although the full extent of how various muscle features affect DWI is not fully understood. Flück *et al.* [5] performed a thorough analysis of very similar cohorts, but their focus was on biopsies of a muscle group in the thigh (*vastus lateralis*). They reported an increase in the myofibrillar volume density and muscle fiber cross-sectional area (MCSA) in their powerlifter cohort. Monte-Carlo simulations have revealed that muscle fiber diameter has the highest impact on diffusion anisotropy and mean diffusivity [53]. Thus, it could be speculated that the muscle hypertrophy observed by Flück *et al.* [5] in the strength-training cohort is due to larger muscle fiber diameters, which in turn contributes to the increase in transverse diffusion $D_\perp$ when compared to the control group and the endurance cohort. Similarly, the observed decrease in the value of the longitudinal diffusion coefficient D_z in the strength cohort could be attributed to the higher macromolecular content (also due to hypertrophy), a factor not present in the endurance cohort [54].

Finally, previous studies have indicated that the value of the pseudo-diffusion coefficient $\boldsymbol{D^*}$ in muscles has very limited reliability due to the low perfusion and low signal-to-noise ratio of these tissues [22,55]. This may explain the wide range of reported $\boldsymbol{D^*}$ estimates in paraspinal muscles alone, spanning $\mathbf{10 - 50 \times 10^{-3}}$ mm²/s with large uncertainties. A Bayesian approach is well suited for parameter estimation under such constraints and was able to demonstrate a marginal posterior of the pooled $\boldsymbol{D^*}$, which appears to be consistent with results in the literature [56,57].

Limitations

Our study has several limitations in that only male subjects were analyzed and the size of each cohort was relatively small, which affects statistical power. Although subjects were all measured at the same time of the day and were asked not to train for 48 hours before the measurements, some studies have indicated [58,59] that the effect of strenuous exercise sessions could alter qMRI parameters to some extent for up to 72 hours after the session. However, such a long rest period was not feasible due to the tight training schedule of the athlete cohorts.

The limited diffusion gradient scheme in our DWI acquisition did not allow the extraction of diffusion tensor eigenvalues, and instead a limited set of diffusion components in the scanner coordinate system was used as an approximation to the diagonal components in the fiber coordinate system. All regions of interest were hand-drawn with care to exclude fat infiltrations, which are often present in the back muscle. Nevertheless, partial volume effects may have affected some voxels, especially in the case of TSE and DWI acquisitions due to their low spatial resolution in the inferior-superior (IS) direction.

Conclusion and outlook

To the best of our knowledge, this study is the first to analyze the long-term effects of exercise on the lumbar back muscle using multiparametric MRI. For this purpose, a comprehensive protocol was designed that provided a variety of parameters, including T_1 and T_2 relaxation times, fat fraction and IVIM-based diffusion parameters. Application of this protocol to a population of athletes revealed significant differences in T_2 and perfusion fraction, which we believe represents a valuable contribution to a growing (and at times discrepant) body of qMRI results reflecting long-term effects of exercise in skeletal muscles. Furthermore, the diffusion tensor components reported in this work, despite the limitations of the DWI protocol employed, suggest a viable route to further evaluate differences caused by long-term effects of different types of training, potentially reflecting underlying microstructural changes. Given that T_1 mapping, carefully corrected for possible B_1 contamination, appears to provide little insight into the effects of exercise, it may be interesting for future research to abandon the VFA approach used in this protocol and employ more advanced diffusion models of microstructure (e.g. NODDI or HARDI, as shown in the preliminary results of Adluru *et al*. [60]). Alternatively, future research efforts could focus on exploring additional parameters such as $T_{1\rho}$. $T_{1\rho}$ values have been shown to be significantly influenced by macromolecular concentration and may be related to intervertebral disc degeneration, which is also implicated in non-specific low back pain. Finally, the ability of the proposed protocol to capture adaptations at rest may offer new perspectives in the evaluation of training-induced changes in skeletal muscle and may aid in the treatment monitoring of NSLBP patients who may not be able to undergo examinations after a strenuous exercise session.

Acknowledgments

This work was supported by a graduate scholarship from the Friedrich-Schiller-University Jena and the state of Thuringia (Landesgraduiertenstipendium) (to Marta B. Maggioni), the Competence Center for Interdisciplinary Prevention (KIP) at the Friedrich Schiller University Jena, the German Professional Association for Statutory Accident Insurance and Prevention in the Foodstuffs Industry and the Catering Trade (BGN) (projects 1.1.7.22 & 1.1.7.23) and the German Research Foundation (Deutsche Forschungsgemeinschaft; KR 4783/2-1).

Figures

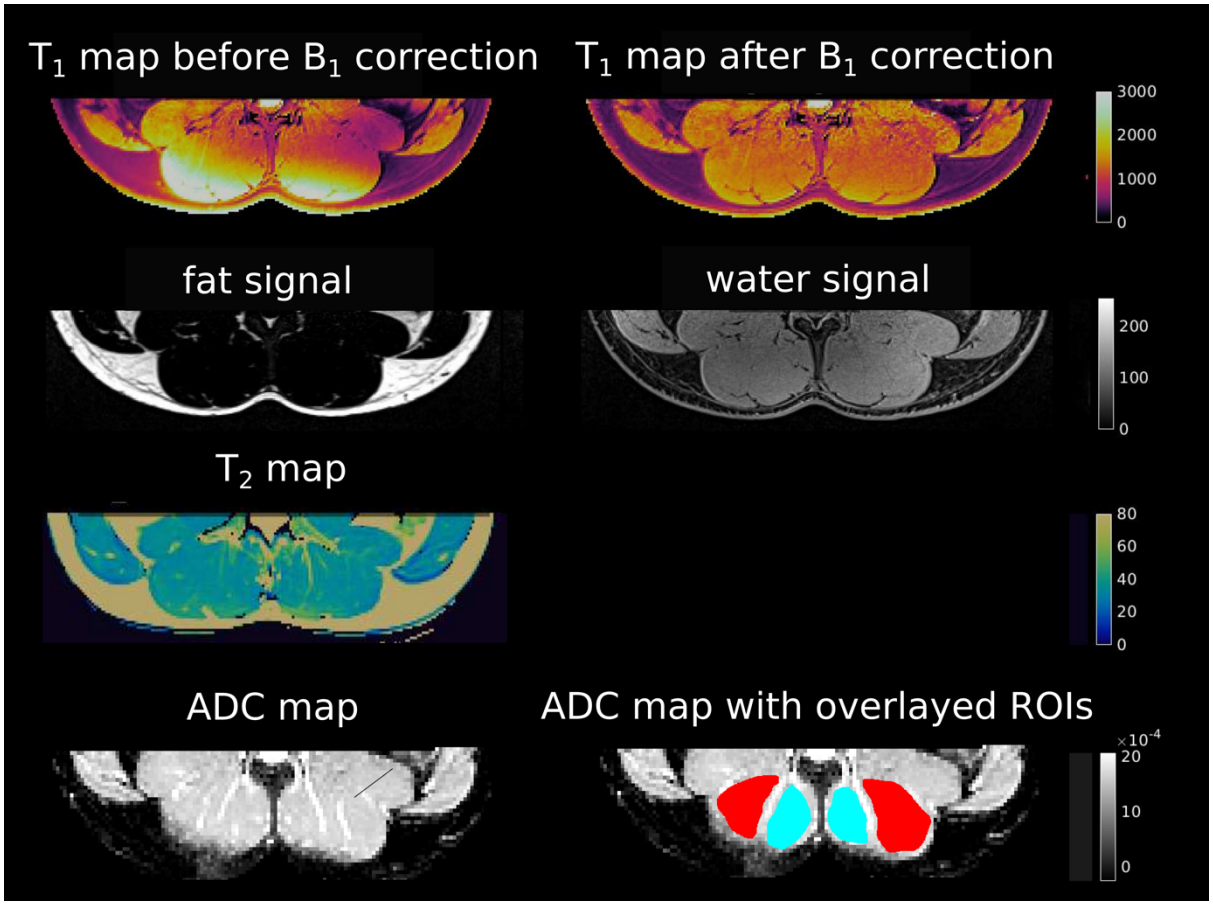

Figure 1. Example images and parameter maps from one subject of the endurance cohort. In the corrected T_1 relaxation time map, the successful B_1-field inhomogeneity correction is clearly visible compared to the uncorrected map (*top row*). Both maps are scaled between 0 and 3000 ms. Images of the fat and water distribution resulting from the Dixon sequence are shown in the second row. The T_2 map (*third row*) is scaled between and 0 and 80 ms. The bottom row shows the ADC map (*left*) scaled between 0 and $20x10^{-4}mm^2/s$ and with superimposed ROIs in the multifidus (blue) and erector spinae (red) muscles used for quantitative analysis (*right*).

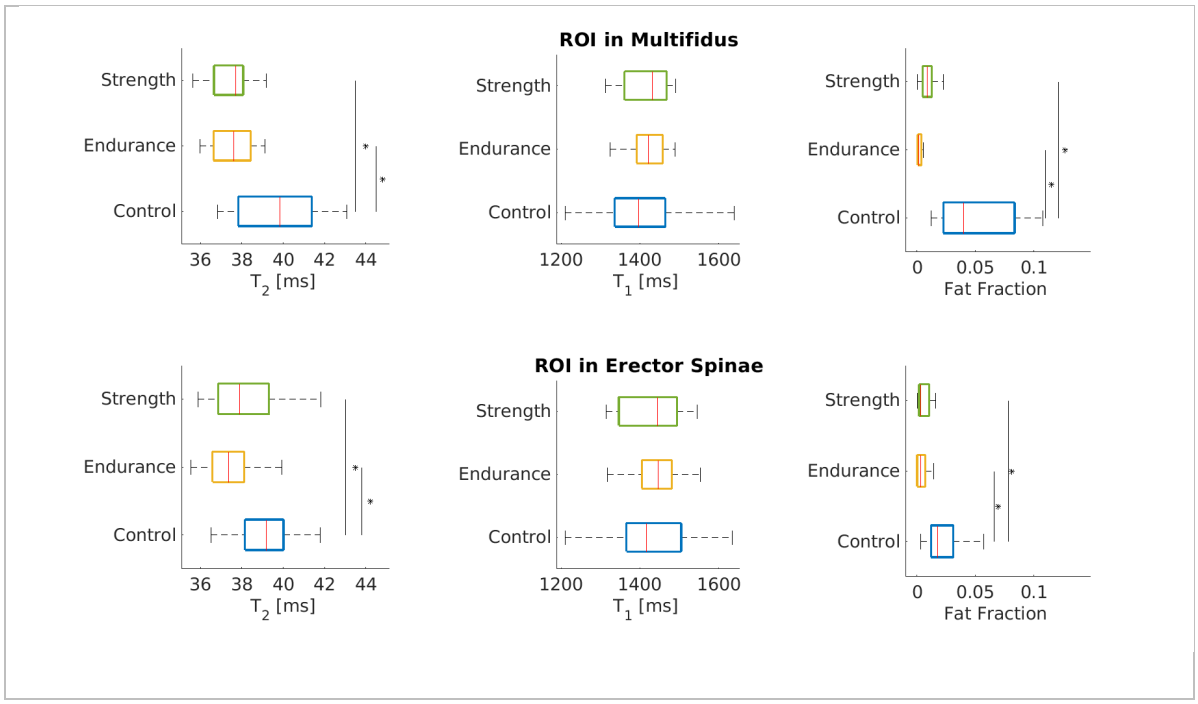

Figure 2. Boxplots of T_2, fat fraction, and T_1 in the multifidus (*top row*) and erector spinae (*bottom row*) muscles of the three cohorts analyzed in this work. * indicates significance at $p<0.05$ between indicated cohorts.

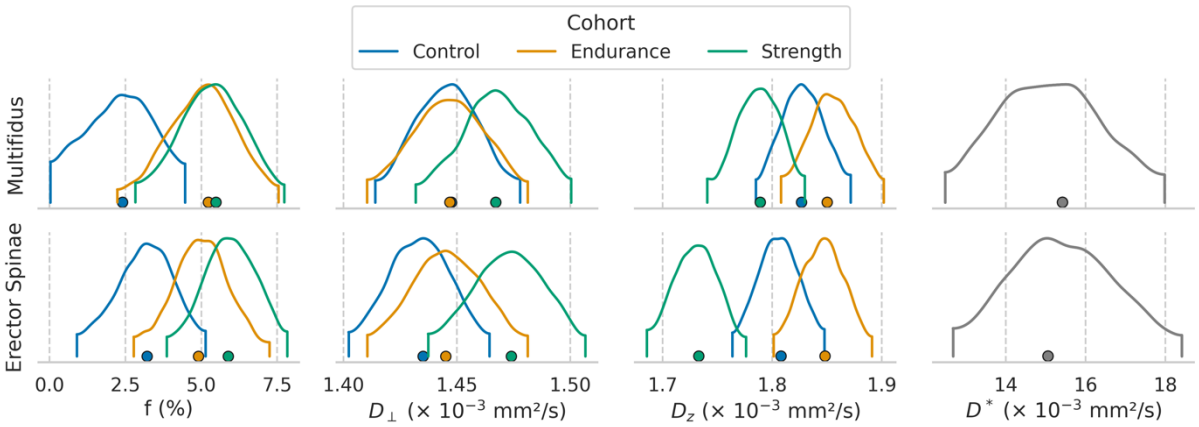

Figure 3. Marginal posterior distributions of the cohort means $f, D_{\perp}, D_z$ and D^* in the multifidus (*top row*) and erector spinae (*bottom row*; all subplots in each column have the same axis scale). Posterior probabilities are cropped to their 95% intervals, dots at the bottom of each plot indicate the maximum of the corresponding posterior (MAP).

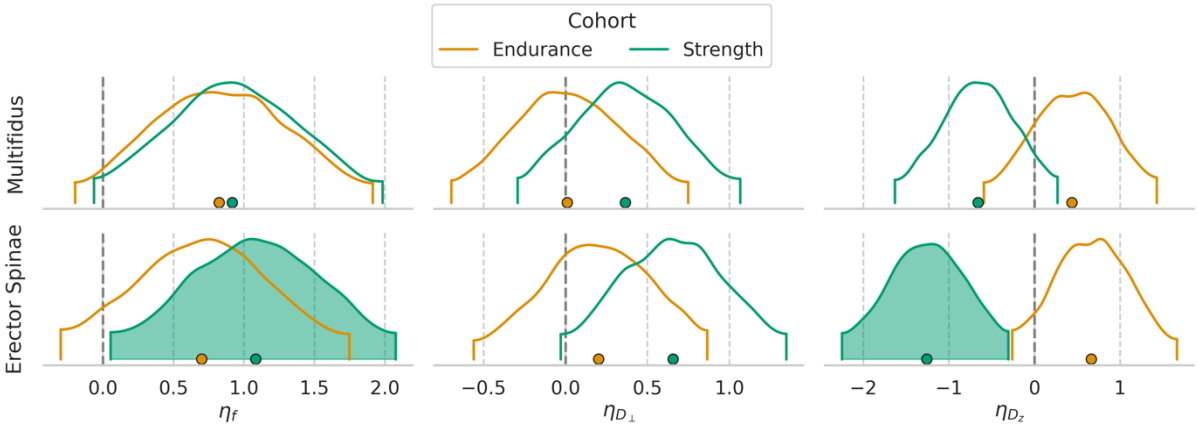

Figure 4. Marginal posterior distribution of effect sizes associated with cohort-level differences. The vertical dashed lines indicate the effect size of 0. Filled posteriors highlight effect sizes where the 95% HDI excludes 0 (significance criterion used for the Bayesian cohort comparison).

References

1. Pinckard K, Baskin KK, Stanford KI. Effects of Exercise to Improve Cardiovascular Health. *Front Cardiovasc Med*. 2019;6:69. doi:10.3389/fcvm.2019.00069

2. Nystoriak MA, Bhatnagar A. Cardiovascular Effects and Benefits of Exercise. *Front Cardiovasc Med*. 2018;5:135. doi:10.3389/fcvm.2018.00135

3. Neufer PD, Bamman MM, Muoio DM, et al. Understanding the Cellular and Molecular Mechanisms of Physical Activity-Induced Health Benefits. *Cell Metab*. 2015;22(1):4-11. doi:10.1016/j.cmet.2015.05.011

4. Samad AKA, Taylor RS, Marshall T, Chapman M a. S. A meta-analysis of the association of physical activity with reduced risk of colorectal cancer. *Colorectal Dis*. 2005;7(3):204-213. doi:10.1111/j.1463-1318.2005.00747.x

5. Flück M, Kramer M, Fitze DP, Kasper S, Franchi MV, Valdivieso P. Cellular Aspects of Muscle Specialization Demonstrate Genotype – Phenotype Interaction Effects in Athletes. *Front Physiol*. 2019;10. Accessed November 6, 2022. https://www.frontiersin.org/articles/10.3389/fphys.2019.00526

6. Andersen JL, Aagaard P. Effects of strength training on muscle fiber types and size; consequences for athletes training for high-intensity sport. *Scand J Med Sci Sports*. 2010;20(s2):32-38. doi:10.1111/j.1600-0838.2010.01196.x

7. Meijer JP, Jaspers RT, Rittweger J, et al. Single muscle fibre contractile properties differ between body-builders, power athletes and control subjects. *Exp Physiol*. 2015;100(11):1331-1341. doi:10.1113/EP085267

8. Terzis G, Spengos K, Kavouras S, Manta P, Georgiadis G. Muscle Fibre Type Composition and Body Composition in Hammer Throwers. *J Sports Sci Med*. 2010;9(1):104-109.

9. Mills KR. The basics of electromyography. *J Neurol Neurosurg Psychiatry*. 2005;76(suppl 2):ii32-ii35. doi:10.1136/jnnp.2005.069211

10. Roberts TJ, Gabaldón AM. Interpreting muscle function from EMG: lessons learned from direct measurements of muscle force. *Integr Comp Biol*. 2008;48(2):312-320. doi:10.1093/icb/icn056

11. Schönau T, Anders C. EMG Amplitude-Force Relationship of Lumbar Back Muscles during Isometric Submaximal Tasks in Healthy Inactive, Endurance and Strength-Trained Subjects. *J Funct Morphol Kinesiol*. 2023;8(1):29. doi:10.3390/jfmk8010029

12. Le Rumeur E, Carré F, Bernard AM, Bansard JY, Rochcongar P, De Certaines JD. Multiparametric classification of muscle T1 and T2 relaxation times determined by magnetic resonance imaging. The effects of dynamic exercise in trained and untrained subjects. *Br J Radiol*. 1994;67(794):150-156. doi:10.1259/0007-1285-67-794-150

13. Sun H, Xu MT, Wang XQ, et al. Comparison Thigh Skeletal Muscles between Snowboarding Halfpipe Athletes and Healthy Volunteers Using Quantitative Multi-

Parameter Magnetic Resonance Imaging at Rest. *Chin Med J (Engl)*. 2018;131(9):1045-1050. doi:10.4103/0366-6999.230740

14. Marth AA, Auer TA, Bertalan G, et al. Low Back Pain in Adolescent Elite Rowers and its Association to Skeletal Muscle Changes Detected by Quantitative Magnetic Resonance Imaging | Research Square. Published online 2022. Accessed August 19, 2022. https://www.researchsquare.com/article/rs-1369489/v1

15. Emanuelsson EB, Berry DB, Reitzner SM, et al. MRI characterization of skeletal muscle size and fatty infiltration in long-term trained and untrained individuals. *Physiol Rep*. 2022;10(14):e15398. doi:10.14814/phy2.15398

16. Patten C, Meyer RA, Fleckenstein JL. T2 Mapping of Muscle. *Semin Musculoskelet Radiol*. 2003;7(4):297-307. doi:10.1055/s-2004-815677

17. Cagnie B, Elliott J, O'Leary S, D'Hooge R, Dickx N, Danneels L. Muscle Functional MRI as an Imaging Tool to Evaluate Muscle Activity. *J Orthop Sports Phys Ther*. 2011;41(11):896-903. doi:10.2519/jospt.2011.3586

18. Hiepe P, Güllmar D, Gussew A, R R, Reichenbach J. Improved IVIM Image Quantitation of Exercised Lower Back Muscles by Principle Component Analysis. In: *Proc. Int. Soc. Magn. Reson. Med.* ; 2013:3491.

19. Kolmer F, Bierry G, Willaume T. Exercise-related leg muscle signal changes: assessment using diffusion-weighted MRI. *Eur Radiol Exp*. 2023;7(1):10. doi:10.1186/s41747-023-00323-2

20. Nguyen A, Ledoux JB, Omoumi P, Becce F, Forget J, Federau C. Application of intravoxel incoherent motion perfusion imaging to shoulder muscles after a lift-off test of varying duration. *NMR Biomed*. 2016;29(1):66-73. doi:10.1002/nbm.3449

21. Federau C, Kroismayr D, Dyer L, Farshad M, Pfirrmann C. Demonstration of asymmetric muscle perfusion of the back after exercise in patients with adolescent idiopathic scoliosis using intravoxel incoherent motion (IVIM) MRI. *NMR Biomed*. 2020;33(3):e4194. doi:10.1002/nbm.4194

22. Englund EK, Berry DB, Behun JJ, Ward SR, Frank LR, Shahidi B. IVIM Imaging of Paraspinal Muscles Following Moderate and High-Intensity Exercise in Healthy Individuals. *Front Rehabil Sci*. 2022;3. https://www.frontiersin.org/articles/10.3389/fresc.2022.910068

23. Fleckenstein J, Canby R, Parkey R, Peshock R. Acute effects of exercise on MR imaging of skeletal muscle in normal volunteers. *Am J Roentgenol*. 1988;151(2):231-237. doi:10.2214/ajr.151.2.231

24. de Sousa PL, Vignaud A, Fleury S, Carlier PG. Fast monitoring of T1, T2, and relative proton density (M0) changes in skeletal muscles using an IR-TrueFISP sequence. *J Magn Reson Imaging*. 2011;33(4):921-930. doi:10.1002/jmri.22511

25. Hildebrandt M, Fankhauser G, Meichtry A, Luomajoki H. Correlation between lumbar dysfunction and fat infiltration in lumbar multifidus muscles in patients with low back pain. *BMC Musculoskelet Disord*. 2017;18(1):12. doi:10.1186/s12891-016-1376-1

26. Schlaeger S, Inhuber S, Rohrmeier A, et al. Association of paraspinal muscle water-fat MRI-based measurements with isometric strength measurements. *Eur Radiol*. 2019;29(2):599-608. doi:10.1007/s00330-018-5631-8

27. Keller S, Yamamura J, Sedlacik J, et al. Diffusion tensor imaging combined with T2 mapping to quantify changes in the skeletal muscle associated with training and endurance exercise in competitive triathletes. *Eur Radiol*. 2020;30(5):2830-2842. doi:10.1007/s00330-019-06576-z

28. Balagué F, Mannion AF, Pellisé F, Cedraschi C. Non-specific low back pain. *The Lancet*. 2012;379(9814):482-491. doi:10.1016/S0140-6736(11)60610-7

29. Shipton EA. Physical Therapy Approaches in the Treatment of Low Back Pain. *Pain Ther*. 2018;7(2):127-137. doi:10.1007/s40122-018-0105-x

30. Christensen KA, Grant DM, Schulman EM, Walling C. Optimal determination of relaxation times of fourier transform nuclear magnetic resonance. Determination of spin-lattice relaxation times in chemically polarized species. *J Phys Chem*. 1974;78(19):1971-1977. doi:10.1021/j100612a022

31. Sacolick LI, Wiesinger F, Hancu I, Vogel MW. B1 mapping by Bloch-Siegert shift. *Magn Reson Med*. 2010;63(5):1315-1322. doi:10.1002/mrm.22357

32. Dixon WT. Simple proton spectroscopic imaging. *Radiology*. 1984;153(1):189-194. doi:10.1148/radiology.153.1.6089263

33. Tournier JD, Smith R, Raffelt D, et al. MRtrix3: A fast, flexible and open software framework for medical image processing and visualisation. *NeuroImage*. 2019;202:116137. doi:10.1016/j.neuroimage.2019.116137

34. Güllmar D, Haueisen J, Reichenbach J. Analysis of b-value calculations in diffusion weighted and diffusion tensor imaging. *Concepts Magn Reson Part A*. 2005;25A:53-66. doi:10.1002/cmr.a.20031

35. Neeman M, Freyer JP, Sillerud LO. A simple method for obtaining cross-term-free images for diffusion anisotropy studies in NMR microimaging. *Magn Reson Med*. 1991;21(1):138-143. doi:10.1002/mrm.1910210117

36. Mozumder M, Beltrachini L, Collier Q, Pozo JM, Frangi AF. Simultaneous magnetic resonance diffusion and pseudo-diffusion tensor imaging. *Magn Reson Med*. 2018;79(4):2367-2378. doi:10.1002/mrm.26840

37. Gelman A, Hill J. Data Analysis Using Regression and Multilevel/Hierarchical Models. Higher Education from Cambridge University Press. doi:10.1017/CBO9780511790942

38. While PT. A comparative simulation study of bayesian fitting approaches to intravoxel incoherent motion modeling in diffusion-weighted MRI. *Magn Reson Med*. 2017;78(6):2373-2387. doi:10.1002/mrm.26598

39. Ferreira da Silva AR. A Bayesian multilevel model for fMRI data analysis. *Comput Methods Programs Biomed*. 2011;102(3):238-252. doi:10.1016/j.cmpb.2010.05.003

40. Orton MR, Collins DJ, Koh DM, Leach MO. Improved intravoxel incoherent motion analysis of diffusion weighted imaging by data driven Bayesian modeling. *Magn Reson Med*. 2014;71(1):411-420. doi:10.1002/mrm.24649

41. Spinner GR, von Deuster C, Tezcan KC, Stoeck CT, Kozerke S. Bayesian intravoxel incoherent motion parameter mapping in the human heart. *J Cardiovasc Magn Reson*. 2017;19(1):85. doi:10.1186/s12968-017-0391-1

42. Gustafsson O, Montelius M, Starck G, Ljungberg M. Impact of prior distributions and central tendency measures on Bayesian intravoxel incoherent motion model fitting. *Magn Reson Med*. 2018;79(3):1674-1683. doi:10.1002/mrm.26783

43. Ye C, Xu D, Qin Y, et al. Accurate intravoxel incoherent motion parameter estimation using Bayesian fitting and reduced number of low b-values. *Med Phys*. 2020;47(9):4372-4385. doi:10.1002/mp.14233

44. Phan D, Pradhan N, Jankowiak M. Composable Effects for Flexible and Accelerated Probabilistic Programming in NumPyro. Published online December 24, 2019. doi:10.48550/arXiv.1912.11554

45. Kruschke JK. Bayesian estimation supersedes the t test. *J Exp Psychol Gen*. 2013;142(2):573-603. doi:10.1037/a0029146

46. Damon BM, Ding Z, Anderson AW, Freyer AS, Gore JC. Validation of diffusion tensor MRI-based muscle fiber tracking. *Magn Reson Med*. 2002;48(1):97-104. doi:10.1002/mrm.10198

47. Sakurai Y, Tamura Y, Takeno K, et al. Association of T2 relaxation time determined by magnetic resonance imaging and intramyocellular lipid content of the soleus muscle in healthy subjects. *J Diabetes Investig*. 2011;2(5):356-358. doi:10.1111/j.2040-1124.2011.00108.x

48. Cercignani M, Dowell NG, Tofts PS. *Quantitative MRI of the Brain: Principles of Physical Measurement*.; 2018.

49. Okamoto Y, Mori S, Kujiraoka Y, Nasu K, Hirano Y, Minami M. Diffusion property differences of the lower leg musculature between athletes and non-athletes using 1.5T MRI. *Magma N Y N*. 2012;25(4):277-284. doi:10.1007/s10334-011-0294-3

50. Hoier B, Hellsten Y. Exercise-Induced Capillary Growth in Human Skeletal Muscle and the Dynamics of VEGF. *Microcirculation*. 2014;21(4):301-314. doi:10.1111/micc.12117

51. Hiepe P, Gussew A, Rzanny R, et al. Interrelations of muscle functional MRI, diffusion-weighted MRI and ^{31} P-MRS in exercised lower back muscles. *NMR Biomed*. 2014;27(8):958-970. doi:10.1002/nbm.3141

52. Tan ET, Zochowski KC, Sneag DB. Diffusion MRI fiber diameter for muscle denervation assessment. *Quant Imaging Med Surg*. 2022;12(1):80-94. doi:10.21037/qims-21-313

53. Berry DB, Regner B, Galinsky V, Ward SR, Frank LR. The relationships between tissue microstructure and the diffusion tensor in simulated skeletal muscle. *Magn Reson Med*. 2018;80(1):317-329. doi:10.1002/mrm.26993

54. Mazzoli V, Rubin E, Barbieri M, et al. Muscle hypertrophy in resistance training assessed with Diffusion Tensor Imaging. In: *Proc. Int. Soc. Magn. Reson. Med.* ; 2021:0668. doi:10.58530/2022/0668

55. Ohno N, Miyati T, Fujihara S, Gabata T, Kobayashi S. Biexponential analysis of intravoxel incoherent motion in calf muscle before and after exercise: Comparisons with arterial spin labeling perfusion and T2. *Magn Reson Imaging*. 2020;72:42-48. doi:10.1016/j.mri.2020.06.003

56. Filli L, Boss A, Wurnig MC, Kenkel D, Andreisek G, Guggenberger R. Dynamic intravoxel incoherent motion imaging of skeletal muscle at rest and after exercise. *NMR Biomed*. 2015;28(2):240-246. doi:10.1002/nbm.3245

57. Wurnig MC, Kenkel D, Filli L, Boss A. A Standardized Parameter-Free Algorithm for Combined Intravoxel Incoherent Motion and Diffusion Kurtosis Analysis of Diffusion Imaging Data. *Invest Radiol*. 2016;51(3):203-210. doi:10.1097/RLI.0000000000000223

58. Maeo S, Ando Y, Kanehisa H, Kawakami Y. Localization of damage in the human leg muscles induced by downhill running. *Sci Rep*. 2017;7(1):5769. doi:10.1038/s41598-017-06129-8

59. Lyu X, Gao Y, Liu Q, Zhao H, Zhou H, Pan S. Exercise-induced muscle damage: multi-parametric MRI quantitative assessment. *BMC Musculoskelet Disord*. 2021;22(1):239. doi:10.1186/s12891-021-04085-z

60. Adluru, N, Kijowski, R, Liu, F. Improved Muscle Microstructure Analysis with Diffusion Weighted Imaging and Advanced Tissue Modeling. In: *Proc. Int. Soc. Magn. Reson. Med.* ; 2017:88. https://archive.ismrm.org/2017/0088.html

61. Hoffman MD, Gelman A. The No-U-Turn Sampler: Adaptively Setting Path Lengths in Hamiltonian Monte Carlo. *J Mach Learn Res*. 2014;15(1):1593-1623.

Appendix

Appendix A: Multilevel Bayesian IVIM model

Prior to averaging the diffusion signal across left and right ROIs, the signal was independently averaged within each ROI and then scaled by the signal intensity at $b = 0$ to minimize the potential effect of large-scale intensity inhomogeneities.

The following equations capture the complete Bayesian multilevel model used for the IVIM evaluation.

$$S_i^{\text{subj}} \sim \text{Rice}(\mu_i^{\text{subj}}, \sigma^{\text{subj}}) \quad \text{(A1)}$$

$$\mu_i^{\text{subj}} = S_0^{\text{subj}} \left(f^{\text{subj}} e^{-b_i D^*} + (1 - f^{\text{subj}}) e^{-b_i D_{d(i)}^{\text{subj}}} \right) \quad \text{(A2)}$$

$$\sigma^{\text{subj}} \sim \text{Exp}(\lambda = 100.0) \quad \text{(A3)}$$

$$S_0^{\text{subj}} \sim \mathcal{N}_+(1.0, 0.1) \quad \text{(A4)}$$

$$f^{\text{subj}} \sim \mathcal{N}_{[0,1]}(f^{\text{coh}}, \sigma_f^{\text{coh}}) \quad \text{(A5)}$$

$$D_d^{\text{subj}} \sim \mathcal{N}_+(D_d^{\text{coh}}, \sigma_D^{\text{coh}}) \quad \text{(A6)}$$

$$f^{\text{coh}} \sim \mathcal{N}_{[0,1]}(0.1, 0.05) \quad \text{(A7)}$$

$$D_d^{\text{coh}} \sim \mathcal{N}_+(1.7, 0.4) \quad \text{(A8)}$$

$$\sigma_f^{\text{subj}} \sim \text{Exp}(\lambda = 5.0) \quad \text{(A9)}$$

$$\sigma_D^{\text{subj}} \sim \text{Exp}(\lambda = 5.0) \quad \text{(A10)}$$

$$D^* \sim \mathcal{N}_+(30.0, 7.0) \quad \text{(A11)}$$

where equations A1 and A2 capture the likelihood of the *i*-th observation (under Rician noise distribution), while the remaining equations define the (hierarchical) prior placed on the model parameters. $D_{d(i)}^{subj}$ in A6 represents a component of the diffusion tensor corresponding to the direction of the diffusion gradient used in the *i*-th observation.

All standard deviations, namely the standard deviation of the Rician noise σ^{subj} and the spread of the cohort-level distributions for f and D_d are given exponential priors parameterized with the rate parameter λ: $P(\sigma;\ \lambda) = \lambda\, exp\ (-\lambda\sigma)$, where higher λ places more probability on lower values. The choice of the exponential distribution was guided by the principle of maximum entropy, and the exact parameterization was chosen based on prior predictive simulations.

Both subject- and cohort-level perfusion fractions receive truncated normal priors constrained to intervals between 0 and 1. Similarly, all diffusion coefficients at each level receive the same truncated normal priors constrained to the positive domain. In addition, in the interest of numerical stability, all b-values were divided by 1000, effectively changing the units of both diffusion and perfusion coefficients to 10^{-3} mm²/s. S_0 also received a normal prior, truncated to the positive values, with a mean of 1 due to the aforementioned normalization by the mean signal at $b = 0$.

Of note, given the high SNR of the averaged signal, the use of a Rician distribution in the likelihood does not change the results compared to using the normal distribution, given that the average estimated SNR is 10.

Sampling from the posterior was performed using the No-U-Turn Sampler[61] using ten independent chains consisting of 1000 samples each (with the first 50% discarded as burn-in).

It was found that under certain overly broad priors, some chains can detect modes of D^* of the same order of magnitude as D, characterized by substantially increased f. MCMC chains ending in such modes (mean $D^* < 5\times10^{-3}$ mm²/s) were manually discarded as representing non-physical local minima.

Table 1. Parameters of the MRI protocol

	VFA GRE	B_1 map	VIBE Dixon	TSE	Diffusion EPI
TR [ms]	16	20	6.1	5	1600
TE [ms]	2.4	1.76	2.46, 3.69	7.8 – 218.4	63
Voxel [mm^3]	1.5×1.5×3	1.5×1.5×3	1.5×1.5×3	1.5×1.5×6	2.3×2.3×8
Averages	-	-	-	-	4
Slices	40	40	40	20	10
TA	15 min	40 s	2 min	16 min	12 min

Table 2. Summary of the values of fat fraction, T_1 and T_2 extracted using the MRI protocol. Values are given as mean ± standard deviation for each cohort. *MF — M. multifidus; ES — M. erector spinae.*

Cohort	T_2 (ms) MF	T_2 (ms) ES	T_1 (ms) MF	T_2 (ms) ES	Fat content (%) MF	Fat content (%) ES
Control	40 ± 3	39 ± 2	1400± 100	1400 ± 120	5	2
Endurance	37 ±1	37 ± 1	1420 ± 40	1440 ± 60	<1	1
Strength	37 ± 1	38 ± 1	142 ± 60	1430 ± 80	1	1

Table 3. Summary of the different parameters extracted using the MRI protocol. Values are given as posterior mode with the 95% HDI in brackets for each cohort. *MF — M. multifidus; ES — M. erector spinae*

Cohort	f (%) MF	f (%) ES	$D_\perp$ ($\times 10^{-3}$ mm/s²) MF	$D_\perp$ ($\times 10^{-3}$ mm/s²) ES	D_z ($\times 10^{-3}$ mm/s²) MF	D_z ($\times 10^{-3}$ mm/s²) ES
Control	2.3 [0.0, 4.5]	3.0 [0.9, 5.1]	1.45 [1.41, 1.48]	1.43 [1.40, 1.46]	1.82 [1.78, 1.87]	1.80 [1.76, 1.86]
Endurance	5.3 [2.2, 7.5]	4.8 [2.8, 7.2]	1.45 [1.41, 1.48]	1.45 [1.41, 1.48]	1.85 [1.81, 1.90]	1.85 [1.80, 1.89]
Strength	4.9 [2.8, 7.7]	5.6 [3.9, 7.8]	1.46 [1.43, 1.50]	1.48 [1.44, 1.51]	1.79 [1.74, 1.83]	1.74 [1.69, 1.78]

Table 4. Summary of effect sizes associated with different parameters extracted using the MRI protocol. Values are given as posterior mode with the 95% HDI in brackets for each cohort. Values in bold are considered significant. *MF — M. multifidus; ES — M. erector spinae*

Cohort	η_f MF	η_f ES	$\eta_{D_\perp}$ MF	$\eta_{D_\perp}$ ES	η_{D_z} MF	η_{D_z} ES
Endurance	0.6 [-0.2, 1.9]	1 [-0.3, 1.7]	-0.2 [-1.1, 0.9]	0.5 [-0.4, 1.6]	0.3 [-0.6, 1.4]	0.8 [-0.3, 1.7]
Strength	0.9 [-0.1, 2.0]	**1.0 [0.1, 2.1]**	1.0 [-0.2, 1.7]	0.3 [-0.5, 1.4]	-0.5 [-1.6, 0.3]	**-1.0 [-2.3, -0.3]**

List of abbreviations:

ADC	Apparent Diffusion Coefficient
AP	Anterior-Posterior
DWI	Diffusion Weighted Imaging
EMG	Electromyography
ES	Erector Spinae (muscle)
HARDI	High Angular Resolution Diffusion Imaging
HDI	Highest Density Interval
IVIM	Intra Voxel Incoherent Motion
IS	Inferior-Superior
LR	Left-Right
MAP	Maximum A Posteriori
MCSA	Muscle Cross Sectional Area
MCMC	Markov chain Monte Carlo

MF	Multifidus (muscle)
NODDI	Neurite Orientation Dispersion and Density Imaging
NSLBP	Non-Specific Low Back Pain
RAS	Right, Anterior, Superior
ROI	Region Of Interest
SEMG	Surface Electromyography
SPAIR	SPectral Attenuated Inversion Recovery
TSE	Turbo Spin Echo
VFA	Variable Flip Angle

6. Discussion

6.1 Summary of the results

The focus of the first published work (Krämer and Maggioni et al., 2019) (see also section 5.1) was to show the feasibility of in vivo UTE-based T_1 and T_2^* quantification for short T_2^* tissues of the knee. Since there was only a single reference (Ma et al., 2019) on the quantification of T_1 for tendons of the knee, T_1 values were acquired using two distinct methods. The employed methods were: Variable Flip Angle (VFA) (Christensen et al., 1974) and Variable Repetition Time (VTR), which were then compared, as illustrated in Figure 6.1. The comparison demonstrated good agreement between the methods: T_1 with VFA was 450±40 [ms], and with VTR was 430±60 [ms] for the patellar tendon, while T_1 with VFA was 689±127 [ms] and T_1 with VTR 676±80 [ms] for the quadriceps tendon. Additionally, it was consistently observed that the quadriceps tendon had higher T_1 values than the patellar tendon, this discrepancy could reflect the physiological distinctions between these tissues: the patellar tendon is known to have a much higher fibril-interstitium ratio than the quadriceps tendon (Hadjicostas et al., 2007), leading to a denser collagen network, which shortens the value of T_1. Figure 6.1 illustrates the T_1 and T_2^* maps calculated for the knee. The T_2^* values for both tendons in the knee closely matched those reported in the literature. Specifically, the patellar tendon exhibited a value of 1.8±0.2 ms, the quadriceps tendon had a value of 1.6±0.4 ms, and the sole reference available (only for the patellar tendon), reported a value of 2±0.4 ms (Kijowski et al., 2017). However, the T_1 values for the patellar and quadriceps

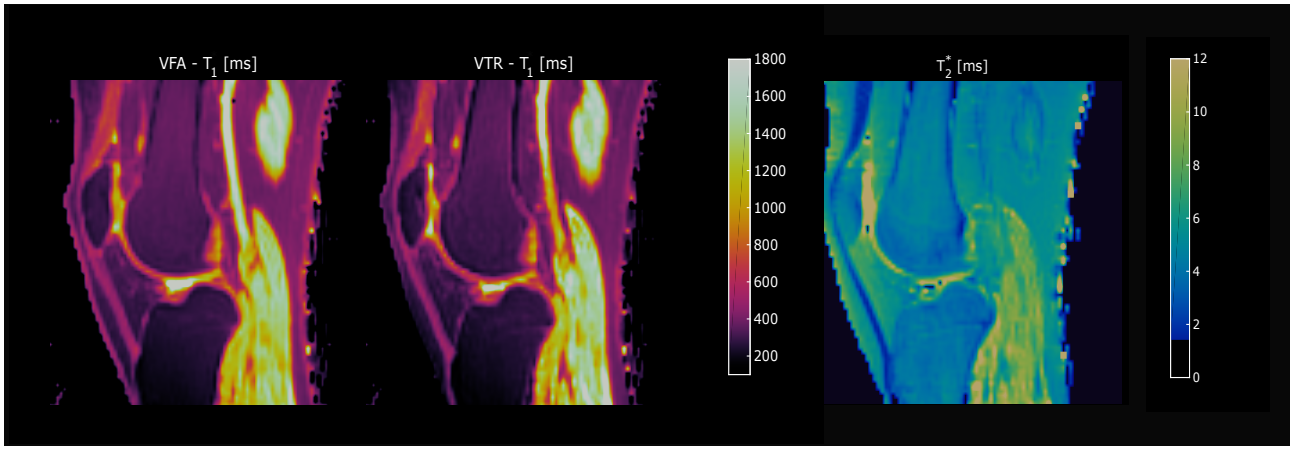

FIGURE 6.1: Parameter maps of T_1 and T_2^* of a volounteers knee, the two T_1 maps have been acquired with different methods: VFA and VTR respectively. The T_1 maps are scaled between 0 and 1800 ms, while the T_2^* maps between 0 and 12 ms. Image is adapted from (Krämer and Maggioni et al., 2019)

tendon were slightly underestimated when compared with the only reference available at the time (Ma et al., 2019).

The second published work (Maggioni et al., 2021b) (see also section 5.2) built upon the T_1 quantification introduced in the previous manuscript. The reason behind the underestimated T_1 values was the absence of B_1 correction. To address this, an existing B_1 correction method (Yarnykh, 2007), which was shown to be compatible with UTE acquisitions (Ma et al., 2018), was improved: making it faster and less dependent on RF phase increment factor. The B_1 correction maps obtained with the proposed improvement were validated both in phantom and in vivo showing high accuracy when estimating the T_1 of different phantom tubes and tissues of the knee. The results of the T_1 maps before and after B_1 correction are shown in Figure 6.2.

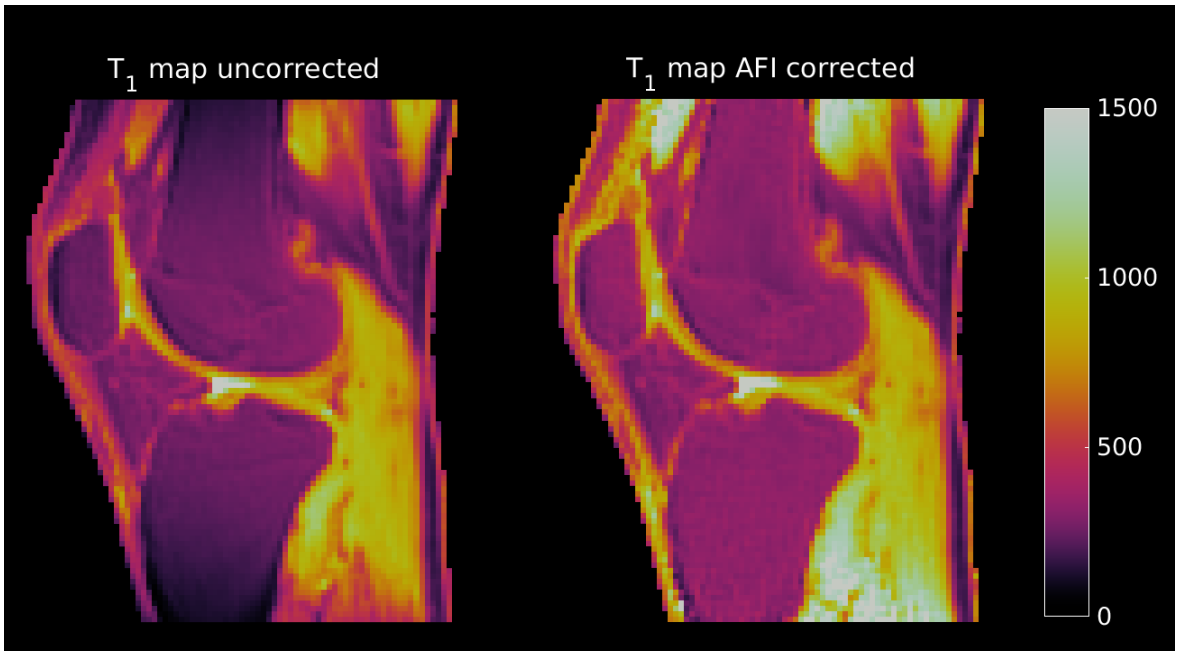

FIGURE 6.2: Parameter maps of T_1 before and after the proposed B_1 correction of a volounteers knee. Note the drop of signal at the edge of the field of view in the uncorrected map. The T_1 maps are scaled between 0 and 1500 ms.

In the (submitted) work on the lumbar back muscle (see section 5.3) a range of MRI parameters (T_1, T_2, fat fraction and IVIM diffusion, as depicted in Figure 6.3) was measured in three different cohorts, of 31 subjects in total, characterised by different levels of physical activity. Among the parameters analysed, T_2 and fat fraction exhibited the most significance, highlighting a difference between the athletes' cohorts and the (non-active) control group. Moreover, both diffusion and perfusion results also revealed a significant difference between the cohorts, and the diffusion coefficient was able to distinguish between the two athletes' groups. It is worth noting that differences in diffusion parameters of skeletal muscles have been only shown after a strenuous exercise session (Hiepe et al., 2014; Hata et al., 2019;

Fleckenstein et al., 1988) but never at rest for the Multifidus and Erector Spinae muscles. T_1 values weren't able to distinguish between the three cohorts, but were consistent with established findings in the literature (Gold et al., 2004).

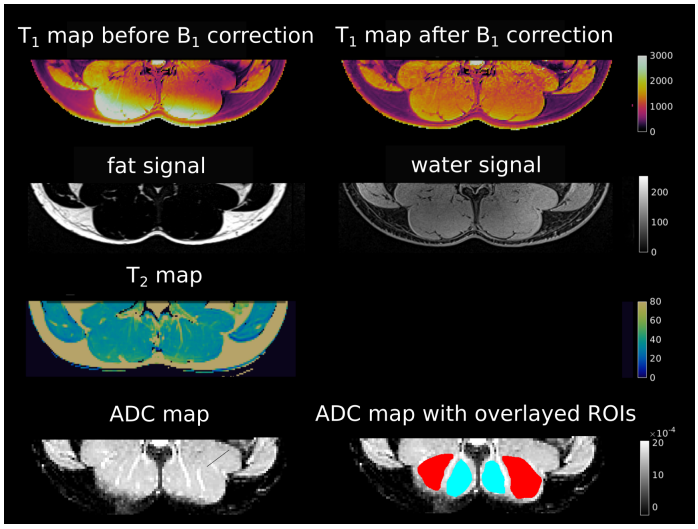

FIGURE 6.3: Results of the MR acquisition protocol of the multiparametric lumbar back muscle study. All the acquired parameters for one exemplary volunteer (of the endurance cohort) are included. Note the need for B_1 correction of the T_1 map. Superimposed on the IVIM ADC map are the ROIs, used to extract values of the qMRI parameters, for one slice in the muscles for this particular subject. Image is from the submitted manuscript.

Thus, all three manuscripts contributed to quantify MRI relaxation parameters in areas of the musculoskeletal system. The first two focused on T_2^* and T_1 UTE-based quantification in tendons of the knee. The third manuscript broadened this scope by assessing training adaptations in the lumbar back muscle, including additional quantitative parameters.

6.2 Quantitative MRI

Quantitative MRI allows to translate physiological and potentially pathological changes into measurable changes of MRI quantitative parameters (Cashmore et al., 2021; Cristinacce et al., 2022) that can be detected before they are visible on qualitative grayscale images. Along with all the benefits, however, comes a new set of challenges regarding the range of normal physiological values versus pathological abnormalities, accurate quantification of parameters and the choice (and sensitivity) of said parameters.

Towards the establishment of a baseline

Typically, the accuracy of a newly introduced technique in qMRI is gauged by its ability to accurately measure known quantitative parameter values. However, significant challenges

emerges when such a baseline of agreed upon quantitative reference values is missing. This situation applies to tissues like tendons, ligaments, and other short T_2^* tissues. Hence, the first and second published articles (Krämer and Maggioni et al., 2019; Maggioni et al., 2021b) are both focused in establishing accurate values for T_2^* and T_1 relaxation parameters for the tendons in the knee, thus contributing to the establishment of said baseline.

The absence of reference values for T_1 and T_2^* in tendons and ligaments of the knee is due to the limitations of standard MRI techniques, which can't effectively capture signal in such short T_2^* species. In the first of the two works (Krämer and Maggioni et al., 2019), two different methods (VTR and VFA) were used to obtain the reference values of T_1 and their results were compared, adding a first layer of internal validation to the results. Furthermore, the knee is composed by many different types of tissues, some of which can be analysed with standard sequences. Building upon prior experience, regions of interest within muscle and bone marrow, which have been more extensively investigated with conventional MRI methods, were analysed. The accurate estimation of T_1 in those tissues, allowed an "indirect" (second layer of) validation of the values that were estimated in the tendons.

At time of publication of the 2019 manuscript, there was only one other research group that had reported T_1 values in tendons in the knee (Ma et al., 2019) and later confirmed their findings (Wu et al., 2020). The results of our study, while comparable, consistently underestimated T_1 when compared with this reference. This was an expected results because the T_1 results presented in this work weren't yet B_1 corrected. Since B_1-field correction affects T_1 quantification also in the lumbar back muscle, this topic will be discussed more in detail in section 6.3.

Evaluation of physiological tissue changes

The work in section 5.3 addressed whether the known physiological adaptations that occur in skeletal muscle as a consequence of repeated physical activity (Thompson, 1994; Nygren et al., 2000; Marini and Veicsteinas, 2010) manifest in changes of quantitative MRI parameters, and which (of those) parameters are more sensitive to those changes. Differently from the majority of studies that have investigated acute, pronounced changes, which immediately follow a strenuous exercise session, (Fleckenstein et al., 1988; Hiepe et al., 2012; Hata et al., 2019; Zaeske et al., 2022) this study focused on the potential to detect more subtle, long term effects (that are associated with a variety of positive effects (Pinckard et al., 2019)) at rest. Investigating quantitative MRI parameters of skeletal muscle at rest is a less well researched topic in the field. Additionally, the lumbar back muscle region, in particular, has been the subject of fewer MRI studies due to challenges posed by (respiratory and peristaltic) movement artifacts, and the presence of a high degree of fat infiltrations, which can bias accurate quantification of quantitative parameters. The choice to focus on muscles of the lumbar spine (specifically targeting Multifidus and Erector Spinae) is motivated by their

involvement in non specific low back pain (Sions et al., 2017). Non specific low back pain is a leading cause of disability worldwide (Balagué et al., 2012), and physical activity has demonstrated its efficacy as a viable treatment option for this condition (Van Middelkoop et al., 2010). However, which type of physical activity is the most beneficial continues to be a subject of discussion. Thus, evaluating long-term effects of training in healthy cohorts and at rest using the multiparametric protocol may pave the way for treatment monitoring for low back pain patients.

Three cohorts of subject were chosen for the study: two (differently trained) athletes cohorts and one control group. The athletes were divided in a strength training group (powerlifters) and an endurance group (long distance runners and cyclists), while the control group was composed of individuals with a relatively sedentary lifestyle. The athletes groups were characterised by very different training routines, in order to examine whether the type of training also manifested in changes to the MRI quantitative parameters. Prior MRI studies conducted at rest have focused separately on endurance athletes (Keller et al., 2020), healthy sedentary subjects or even compared the latter to pathological subjects (Hooijmans et al., 2015), with no previous MRI investigation into the potential long-term influence of the type of training for the back muscle.

The choice of a multi-parametric protocol was because the MRI examination was conducted at rest where the differences between cohorts might be less pronounced and affect a wider range of different parameters rather than the well-established post intervention increase of the values of T_2^* and diffusion coefficients (Fleckenstein et al., 1988; Hiepe et al., 2012; Hata et al., 2019; Zaeske et al., 2022). This choice was also motivated by the goal to investigate some well established parameters such as T_2^* and fat fraction, but also some less well researched parameters such as T_1 and IVIM diffusion.

6.3 B_1-field correction

As previously mentioned, B_1-field correction is crucial to retrieve correct T_1 values both in the tendons and lumbar back muscles, however the sources of the B_1-field inhomogeneities and the strategies to address them depends on the characteristic of the investigated tissue and its surroundings.

The tendons of the knee lie close to the surface of the skin, thus are not affected by the most common sources of B_1 inhomogeneity such as RF penetration and conductivity issues (previously introduced in section 3.9), differently from the lumbar back muscle where these factors play a more significant role. However, in the knee, another source of B_1 inhomogeneity arises, not related to the characteristics of the tissue, but due to the type of coil often used for the measurements. As shown in paragraph 3.4, the signal is generated by the application of an oscillating B_1 field, and detected by a receiver RF coil. The additional source

of B_1 inhomogeneity for knee applications can arise when a transmit/receive (Tx/Rx) coil is used for knee imaging. In a Tx/Rx coil, both the transmission and reception of the B_1 field are performed by the coil itself, as opposed to a receiver-only coil where the transmission is done by the body coil or dedicated RF transmit coils. This results in the transmit field being influenced by the coil's sensitivity profile, which can be observed in the left image of Figure 6.2 as a drop of signal towards the edge of the field of view.

Furthermore, B_1-field correction for short T_2^* species is particularly challenging because most of the well established methods, aren't compatible with UTE acquisition, and the previous implementations of the AFI methods suffer from very long acquisition times and are strongly dependent on the choice of the RF phase increment (Yarnykh, 2007). Currently, the proposed implementations (Ma et al., 2019) of the AFI method rely on a careful choice of the RF phase factor and the use of large spoiler gradients to make sure that the "ideal spoiling" condition is met. However, the RF phase factor value is not readily accessible at most MRI scanners, and the use of large spoiling gradients (together with the TRs requirements introduced in section 3.9) result in extremely long acquisition times that hinder the applicability of this method in vivo. Moreover, the work of Nehrke (Nehrke, 2009) showed the importance of the diffusion coefficient of the measured sample to dephase residual transverse magnetisation. This coefficient not only influences the AFI method's dependence on the RF phase factor but is also influenced by temperature, potentially hindering the repeatability of the AFI method. To address this issue, an improvement on the existing AFI method was proposed (Maggioni et al., 2021b), making it quicker and more robust against spoiling issues with the addition of randomised gradient spoiling in the x and y directions. These modifications made the method more robust in that the dependence on the RF phase increment was completely eliminated, which consequently allowed for the removal of the method's dependency on the tissues' diffusion coefficient. This increased robustness also allowed the use of shorter gradient spoilers and shorter TR, reducing the acquisition time by a factor up to two, while keeping the quantitative T_1 values within an acceptable range (below 2 % of error).

The additional speed brings this method closer to in vivo applications, although still not in range of clinical routine. In a follow-up work, the AFI protocol was further accelerated by undersampling the acquisition of the 3D radial k-space (Maggioni et al., 2021a). This reduction in acquisition time enabled an AFI-based B_1 map to be acquired in just 2 minutes, thus allowing the AFI correction to be used for a wider range of applications (including dynamic and in vivo studies).

B_1-field correction in the lumbar muscle differs in some regards from knee applications. In this case, B_1-field inhomogeneities arise from two main physical properties of the imaged sample (Franklin et al., 2008): conductivity and permittivity. In a conductive sample, the oscillating B_1 field induces opposing currents, partially shielding deeper tissues from the

RF field. Furthermore, a strongly dielectric sample (as, for example, most tissues containing water) will cause the wavelength of the RF pulse to be reduced, leading to the formation of a standing wave pattern, with constructive and destructive interferences. The focus of the (third) submitted work (section 5.3) was the lower trunk of volunteers. In this body area, B_1-field correction is an especially challenging task because standing waves, RF penetration and conductivity issues combine resulting in signal inhomogeneities (Sled and Pike, 1998; Hoult, 2000; Fernandez-Seara et al., 2001). This signal inhomogeneity is clearly visible in Figure 6.3 where the overestimated T_1 values in the map before B_1 correction are corrected by the application of a B_1 map, leading to a more homogeneous distribution in the T_1 map. In this case the Bloch Siegert method (see section 3.9), which is routinely used for research applications and has been shown to work for a variety of tissues in the body, but has mostly been optimised for neuroimaging applications (Sacolick et al., 2010), was adapted for use in the area of the lumbar spine. This marked the first application of the method to correct T_1 in back muscle, displaying its versatility and ability to function in different body areas. However, this application faced additional challenges due to movement artifacts and the nature of the investigated tissues.

6.4 Challenges in quantifying MRI parameters in musculoskeletal tissues

There are a number of challenges associated with quantitative MR imaging of muscle and tendons. Firstly, both tendons and muscles are fibrous structures, which needs to be taken into account during MRI measurements. It is well known (Fullerton and Rahal, 2007) that the orientation of the fibres (with respect to the external magnetic field) can influence and bias the quantification of T_2^* and T_2. This is the so-called "magic angle" phenomenon, which arises due to dipolar interactions of neighbouring nuclear spins in structured tissues. On the other hand, some quantitative parameters such as diffusion coefficient values can offer insights into the organization of these tissues. Thus, they provide indirect information about the tissue ordering degree, which has been shown to be a marker for ageing (Jerban et al., 2019) and early disease detection in both muscle (Forsting et al., 2022) and tendon (Robson et al., 2004), as well as a mean to characterise healthy muscle tissue. Diffusion studies in tendons, however, are much more challenging due to the fast decay of the signal in these tissues, which requires positioning the investigated tendon at the magic angle (Wengler et al., 2020). In this work, great care was taken to align both tendons and muscle tissue as closely as possible with the main magnetic field in order to reduce the influence of fibre orientation.

Secondly, a variety of musculoskeletal tissues, but muscle in particular, are intrinsically heterogeneous (for example: even healthy muscles contain small fractions of fat and connective tissue). This heterogeneity poses a challenge in accurately quantifying qMRI parameters in these structures. One, possible, approach would be to filter out all fat-containing voxels from the data (manually or automatically using sequences to separate fat from water as best as possible). However, this diversity in fat content has also been shown to be an important marker for muscle health and functions: (Burakiewicz et al., 2017) used it to asses the progress of muscular distrophies, and in our study (5.3) and others (Emanuelsson et al., 2022) it was shown that the fat fraction correlated with a sedentary lifestyle.

Moreover, motion artifacts are another source of uncertainty that can affect correct quantification of parameters in a given ROI. The performed knee based studies were less susceptible to these artifacts due to the inherent protection offered by the 3D UTE radial application. The radial UTE acquisition is also robust against flow artifacts (Feng et al., 2016). However, the lumbar back muscle area is affected by both respiratory and peristaltic movements (Bellon et al., 1986). In this latter case, the surface coils were placed in a way to receive most of the signal only from the lumbar muscle and acquisition parameters were chosen to mitigate the artifacts.

Finally, ROI-based analysis always carry the risk of user bias due to the choice of the hand drawn ROI on a 2D slice. This is especially true for tendons, where the investigated structures on the image are small and comprise only a few voxels. To address this issue, it was decided to not restrict the analysis to a single slice, but to construct a volume ROI by drawing regions across multiple slices for the lumbar back muscle study. Moreover, in the 2019 work (Krämer and Maggioni et al., 2019), it was demonstrated that by combining the information from accurate UTE-based T_1 and T_2^* maps, a semi-automatic bivariate histogram based segmentation method could be developed, thus eliminating the need for 2D hand-drawn ROIs.

6.5 Outlook

The 2019 and 2021 works (Krämer and Maggioni et al., 2019; Maggioni et al., 2021b) provided accurate values of the T_1 and T_2^* relaxation parameters in the tendons of the knee. These values were rarely and, in the case T_2^* of the quadriceps tendon, never quantified before. Quantifying such values in healthy subject constitutes the first step towards setting a standard range for these parameter values. This baseline was expanded in subsequent works that investigated (both in vivo and in animal models) the influence of age and gender on T_2^* (Loegering et al., 2021; Pownder et al., 2022). These advances could pave the way for more advanced studies, where musculoskeletal pathologies such as tendinopathy or osteoarthritis (OA) could to be detected earlier by the use of UTE sequences (Agergaard et al.,

2021). Furthermore, dynamic studies (Aleksiev et al., 2022), investigating changes in knee morphology during movement, could benefit from quantitative mapping to explore how physiological movements affect the values of the quantitative parameters and try to identify early markers for OA developments. OA is known to disproportionally affect individuals that had a history of anterior cruciate ligament surgery and may be linked to biomechanical adaptations (Azus et al., 2018). Finally, dynamic mapping could be used to quantify athletes performance and assess injury risks, allowing for prompt intervention and treatment.

The work on lumbar back muscles in athletes demonstrates the potential of the multi parametric protocol to highlight adaptations of the muscle structure to known external stressors (in this case, long term effects of physical activity), even when the studies are performed at rest. The benefits of such an approach are twofold especially relating to non specific low back pain (NSLBP) patients. Firstly, since physical activity is a recognised treatment for NSLBP, MRI could be used as a non-invasive tool to track treatment progress, secondly, the investigation at rest is particularly beneficial for NSLBP patients, that cannot always be subjected to strenuous exercise interventions. Furthermore, the multi parametric protocol could be used as a non-invasive screening tool to evaluate the development and progression of occupational injuries in known at-risk groups. Finally, exploring more parameters such as Magnetisation Transfer (MT) (Sinclair et al., 2012) and $T_{1\rho}$ (Wáng et al., 2015; Wang and Regatte, 2015) could enhance the understanding of structural and biophysical changes in tendons and muscles. The work in this thesis focused mostly on T_1 and T_2, which are the fundamentals MRI relaxation parameters and are predominately influenced by tissue water (and fat) content. However, recent studies have shown that the values of MT and $T_{1\rho}$ are significantly influenced by macromolecules concentration and the chemical exchange process between bound and free water proton pools in tissues (Elliott et al., 2018; Noehren et al., 2021). This aspect opens up new diagnostic possibilities, because alteration in the macromolecules concentration or water proton pools can function as an early marker of a number of musculoskeletal pathologies such as tendinopathy, muscle atrophy and fibrosis (Abate et al., 2009; Menon et al., 2019; Kollmer et al., 2021).

7. Conclusions

Quantitative MRI for musculoskeletal applications has been shown to improve the diagnosis, tracking of disease progression and monitoring of treatment in musculoskeletal applications. Additionally, it also provides a non invasive tool for the characterisation of healthy tissue. However, significant challenges are present before clinical translation can be achieved, such as identifying the range of normal quantitative values in healthy tissues as well as accelerating sequences and providing accurate quantification in previously scarcely imaged areas.

In this work, multiparametric analysis was conducted for tissues in the knee and lumbar back muscle. The UTE-based knee studies, showed that a quantitative analysis is possible even in areas that were previously very difficult to analyse (as tendons) and constituted some of the first reference values of T_1 and T_2^* available for these tissues. However, the use of UTE requires novel methods also for B_1 quantification, which is crucial to retrieve correct T_1 values. The UTE compatible B_1 mapping methods available in the literature have been shown to be both strongly dependent on the values of several different parameters and characterised by very long acquisition times. In this work, an improvement of the current AFI method was proposed that manages to remove its dependency on the RF phase factor and, consequently, reduce the acquisition time. The acquisition time was further reduced with undersampling leading to an accurate and robust B_1 mapping sequence that can be acquired in under 2 min.

Furthermore, differences in lumbar back muscles parameter values due to different training routines were analysed. It was shown that: T_2, fat fraction and diffusion are able to distinguish between trained and untrained subjects as well as between athletes with drastically different training routines, even when the measurements are performed at rest. This opens the door to characterise training induced-changes in muscles not only after strong physical exertion as it is commonly done in literature. Since T_1 is unable to detect differences between the three cohorts it may not be a parameter of choice to characterise the low back muscles. On the other hand, the T_2 values of the back muscles, especially for the normal cohort, may have been biased by the increased fat fraction. This suggests that in future studies more complex data acquisition strategies (such as a 6-point Dixon approach (Grimm et al., 2019)) and fitting models (including a multi-peak fat model (Wang et al., 2016)) might be needed to ensure accurate distinction of the signal originating from fat and water protons.

In conclusion, this work showed that multiparametric MRI studies of the musculoskeletal system have the potential to quantitatively assess tissues in the knee and lumbar back muscle. This work contributed to setting a baseline of parametric values for tendons of the knee, where qMRI methods are not yet fully established, and thus reliable reference

values aren't available. For accurate T_1 quantification, this required the development of a novel spoiling scheme for a fast and accurate B_1 mapping method, compatible with UTE acquisition. The multiparametric approach was further extended to investigate the long term effects of training in the lumbar back muscles. During this investigation, additional quantitative parameters such as fat fraction and diffusion were incorporated to analyse the muscle tissues. This demonstrated that, with qMRI's is possible to identify adaptations even at rest, highlighting which parameters were more sensitive to training-induced adaptations in muscle fibres. It was possible to relate these results with known physiological adaptations resulting from training, thus showing the potential of this multiparametric protocol to characterise muscle tissues.

Declaration of Authorship

Hiermit erkläre ich, dass

mir die geltende Promotionsordnung der Medizinischen Fakultät der Friedrich-Schiller-Universität bekannt ist,

ich die Dissertation selbst angefertigt habe, keine Textabschnitte eines Dritten oder eigener Prüfungsarbeiten ohne Kennzeichnung übernommen und alle von mir benutzten Hilfsmittel, persönlichen Mitteilungen und Quellen in meiner Arbeit angegeben habe,

mich folgende Personen bei der Auswahl und Auswertung des Materials sowie bei der Herstellung des Manuskripts unterstützt haben: Prof. J. R. Reichenbach, Dr. M. Krämer.

die Hilfe einer kommerziellen Promotionsvermittlung nicht in Anspruch genommen wurde und dass Dritte weder unmittelbar noch mittelbar geldwerte Leistungen von mir für Arbeiten erhalten haben, die im Zusammenhang mit dem Inhalt der vorgelegten Dissertation stehen,

ich die Dissertation noch nicht als Prüfungsarbeit für eine staatliche oder andere wissenschaftliche Prüfung eingereicht habe,

eine gleiche, eine in wesentlichen Teilen ähnliche oder eine andere Abhandlung bei einer anderen Hochschule als Dissertation nicht eingereicht wurde

Ort, Datum: Unterschrift des Verfassers / der Verfasserin:

Curriculum Vitae

Personal Informations

Surname, First names Maggioni, Marta Brigid

Date and Place of Birth 24.12.1993, Monza, Italy

Education and Training

PhD student Since October 2019
Jena University Hospital Jena, Germany

M. Sc. Medical Photonics October 2016 – May 2018
Friedrich Schiller University Jena, Germany

B. Sc. Engineering Physics September 2012 – September 2016
Politecnico di Milano Milan, Italy

Highschool Diploma August 2012
Liceo Classico Tito Livio, Milan, Italy Milan, Italy

List of publications

M. Krämer, **M. B. Maggioni**, N.M. Brisson, S. Zachow, U. Teichgräber, G.N. Duda, J. R. Reichenbach. (2019). T_1 and T_2^* mapping of the human quadriceps and patellar tendons using ultra-short echo-time (UTE) imaging and bivariate relaxation parameter-based volumetric visualization. Magnetic resonance imaging, 63, 29–36. 10.1016/j.mri.2019.07.015

M. Krämer, M. Kollert, N. Brisson, **M. B. Maggioni**, G.N. Duda, J. R. Reichenbach. (2020) Immersion of Achilles tendon in phosphate-buffered saline influences T_1 and T_2^* relaxation times: An ex vivo study. NMR in Biomedicine. 33. 10.1002/nbm.4288.

M. B. Maggioni, M. Krämer, J. R. Reichenbach. (2021). Optimized gradient spoiling of UTE VFA-AFI sequences for robust T 1 estimation with B 1-field correction Magnetic Resonance Imaging. 10.1016/j.mri.2021.06.011.

M. Aleksiev, M. Krämer, N. Brisson, **M. B. Maggioni**, G.N. Duda, J. R. Reichenbach. (2022). High-resolution CINE imaging of active guided knee motion using continuously acquired golden-angle radial MRI and rotary sensor information. Magn Reson Imaging. 2022 Oct;92:161-168. doi: 10.1016/j.mri.2022.06.015.

Conferences and Presentations

M. Krämer, **M. B. Maggioni**, C. von Tycowicz, N. Brisson, S. Zachow, G.N Duda, J. R. Reichenbach (2018) Ultra-short echo-time (UTE) imaging of the knee with curved surface reconstruction-based extraction of the patellar tendon, Proc. Intl. Soc. mag. Reson. Med. 1431.

M. B. Maggioni, M. Krämer, J. R. Reichenbach (2019) T_1 and T_2^* quantification of the patellar tendon and entheses with UTE MRI, 22nd Ann. Meet. Ger. Chapter Proc. Int. Soc. Magn. Reson. Med.

M. Krämer, M. Kollert, N. Brisson, **M. B. Maggioni**, G.N Duda, J. R. Reichenbach. (2019) Immersion of ex vivo Achilles tendon in phosphate buffered saline influences their T_1 and T_2^* relaxation times, Proc. Intl. Soc. mag. Reson. Med. 2816

M. Krämer, **M. B. Maggioni**, J. R. Reichenbach. (2019) Volumetric tendon segmentation using ultra-short echo-time (UTE) imaging and bivariate relaxation parameter-based histogram analysis, Proc. Intl. Soc. mag. Reson. Med. 2808

M. Krämer, **M. B. Maggioni**, J. R. Reichenbach. (2019) MRT basierte Segmentierung des Kniegelenkes durch bivariate Analyse gewebespezifischer Relaxationsparameter, 26th Erfurter Tage of the BGN.

M. B. Maggioni, M. Krämer, J. R. Reichenbach. (2020) A three compartment complex signal model to describe the signal decay of ultrashort T_2^* tissues applied to ex-vivo ovine Achilles' tendons, Proc. Intl. Soc. mag. Reson. Med. 2817.

M. B. Maggioni, M. Krämer, J. R. Reichenbach. (2020). Optimized gradient Spoiling for B_1 mapping with UTE AFI that is less sensitive to the RF-spoiling phase increment,

Proc. Intl. Soc. mag. Reson. Med. 3386.

M. B. Maggioni, M. Krämer, J. R. Reichenbach. (2020) Accelerating 3D-UTE-AFI B_1 mapping to correct VFA-based T_1 estimations in short T_2^* tissues, abstract presented at DGMP 2020

M. B. Maggioni, M. Krämer, J. R. Reichenbach. (2021). Accelerated 3D-UTE-AFI B_1 mapping to correct VFA-based T_1 estimations in short T_2^* tissues, Proc. Intl. Soc. mag. Reson. Med. 3305.

M. Aleksiev, M. Krämer, N. Brisson, **M. B. Maggioni**, G.N Duda, J. R. Reichenbach. (2021). High resolution CINE imaging of guided knee motion using golden-angle radial MRI and a novel knee loading device, Proc. Intl. Soc. mag. Reson. Med. 0381.

M. B. Maggioni, M. Krämer, J. R. Reichenbach. (2021). Improved UTE AFI spoiling scheme for faster B_1 correction. 23th Ann. Meet. Ger. Chapter Int. Soc. Magn. Reson. Med. Zürich.

M. B. Maggioni, M. Krämer, D. Güllmar, C. Anders, J. R. Reichenbach. (2021) Einfluss von Kraft- und Ausdauertraining auf die Rückenmuskulatur aus Sicht der quantitativen MRT Bildgebung. 27th Erfurter Tage of the BGN.

M. Aleksiev, M. Krämer, N. Brisson, **M. B. Maggioni**, G.N Duda, J. R. Reichenbach. (2021). Hochaufgelöste dynamische ergometergestützte MRT-Bildgebung des Kniegelenkes. 27th Erfurter Tage of the BGN.

M. B. Maggioni, M. Krämer, C. Anders, J. R. Reichenbach. (2022) Investigations of the effects of differently trained subject cohorts on T_1 and T_2^* of the lumbar spine muscles. Proc. Intl. Soc. mag. Reson. Med. 2885.

M. B. Maggioni, M. Krämer, H. Stark, J. R. Reichenbach. (2022) T_1 and T_2^* mapping of sheep forelimb aponeuroses with high-resolution ultra-short echo time (UTE) imaging. Proc. Intl. Soc. mag. Reson. Med. 1491.

M. B. Maggioni, M. Krämer, C. Anders, J. R. Reichenbach. (2022) Untersuchungen zu den Auswirkungen unterschiedlich trainierter Probandenkohorten auf T_1 und T_2^* der Lendenwirbelsäulenmuskulatur, AKP meeting, Jena.

M. B. Maggioni, J. R. Reichenbach. (2023). Multiparametrische MR-Bildgebung zur Charakterisierung der lumbalen Rückenmuskulatur von Probanden mit unterschiedlichem Aktivitätsniveau. 28th Erfurter Tage of the BGN.

M. B. Maggioni, M. Krämer, J. R. Reichenbach. (2023). Temperaturabhängigkeit der quantitativen MRT-Relaxationsparameter in Schafsehnen. 28th Erfurter Tage of the BGN.

List of Figures

Acknowledgements

The work of this thesis and during my doctorate wouldn't be achieved without the help and support of many people. I'd like to take a moment to thank a few.

Firstly, I'd like to thank Prof. Jürgen Reichenbach for his supervisorship, deep knowledge of the field and meticulous attention to details, which I sometime lack.

I am thankful to Martin Krämer for being a scientific mentor and showing me the ropes of science and research. I am especially thankful for his near-constant availability for questions, his creation of a positive environment for scientific exchange and his open-mindness to "creative" methods (such as re-purposing Christmas ornaments as tendon holders).

I also want to thank my family for always being there for me, even from afar, with "quick" Skype calls that turn into hours-long chats *über Gott und die Welt* (sometimes literally, sometimes metaphorically). I deeply appreciate their personal and academical support, their willingness to listen to my rants and stretching the limits of my comfort zone: *dal profondo del mio cuore, grazie!*.

I am grateful to David for his constant support, unwavering optimism, endless patience and love. Thank you for being there with me in front of late summer bonfires after a long day of writing the thesis and for me in times where I struggled (including when we both got COVID two weeks before my original deadline). Also thanks for proofreading the (many) final versions of the thesis.

I would like to also thank Renat and Wan-Ting for being long-standing companions on this PhD journey. I am grateful for our travels together at international conferences, late night ISMRM submission scrambles and chats in the kitchen. I am grateful to Karl-Heinz for answering question and sparking interesting discussions on many topics, from physics to coffee, cooking and many more. All the other members of the Medical Physics Group (past and present) also deserve a special mention for having supported me in these years at the Steiger.

Finally, I want to acknowledge the The Rowena Morse Mentoring Programm, for providing me with a safe space of discussion and allowing me to reflect about my future steps during the last year of my PhD. I'd like to thank the Graduate Academy at the Friedrich-Schiller University for awarding me with the Landesgraduiertenstipendium, and the BGN (Berufsgenossenschaft Nahrungsmittel und Gastgewerbe) for contributing to my financial support during these years.

I truly wouldn't have made it here without all your help

Bibliography

Abate, M., Gravare Silbernagel, K., Siljeholm, C., Di Iorio, A., De Amicis, D., Salini, V., Werner, S., and Paganelli, R. 2009. "Pathogenesis of tendinopathies: inflammation or degeneration?" *Arthritis Research & Therapy* 11.3, pp. 1–15.

Affatato, S. 2015. "Biomechanics of the knee". *Surgical Techniques in Total Knee Arthroplasty and Alternative Procedures*. Elsevier, pp. 17–35.

Afsahi, A. M., Ma, Y., Jang, H., Jerban, S., Chung, C. B., Chang, E. Y., and Du, J. 2022. "Ultrashort echo time magnetic resonance imaging techniques: met and unmet needs in musculoskeletal imaging". *Journal of Magnetic Resonance Imaging* 55.6, pp. 1597–1612.

Agergaard, A.-S., Malmgaard-Clausen, N. M., Svensson, R. B., Nybing, J. D., Boesen, M., Kjaer, M., Magnusson, S. P., and Hansen, P. 2021. "UTE T_2^* mapping of tendinopathic patellar tendons: an MRI reproducibility study". *Acta Radiologica* 62.2, pp. 215–224.

Ahn, J. M. and El-Khoury, G. Y. 2007. "Role of magnetic resonance imaging in musculoskeletal trauma". *Topics in Magnetic Resonance Imaging* 18.3, pp. 155–168.

Aleksiev, M., Kraemer, M., Brisson, N. M., Maggioni, M. B., Duda, G. N., and Reichenbach, J. R. 2022. "High-resolution CINE imaging of active guided knee motion using continuously acquired golden-angle radial MRI and rotary sensor information". *Magnetic Resonance Imaging* 92, pp. 161–168.

Argentieri, E. C., Shah, P. H., Nwawka, O. K., and Koff, M. F. 2017. "Bilateral Differences in Patellar Tendon T_2^* Values Correlate With Differences in Morphologic Grade of Patellar Tendinosis Within Collegiate Basketball Players". *Proc. Int. Soc. Magn. Reson. Med.*, p. 1561.

Azus, A., Teng, H.-L., Tufts, L., Wu, D., Ma, C. B., Souza, R. B., and Li, X. 2018. "Biomechanical factors associated with pain and symptoms following anterior cruciate ligament injury and reconstruction". *PM&R* 10.1, pp. 56–63.

Balagué, F., Mannion, A. F., Pellisé, F., and Cedraschi, C. 2012. "Non-specific low back pain". *The Lancet* 379.9814, pp. 482–491.

Bellon, E. M., Haacke, E. M., Coleman, P. E., Sacco, D. C., Steiger, D. A., and Gangarosa, R. E. 1986. "MR artifacts: a review". *American Journal of Roentgenology* 147.6, pp. 1271–1281.

Bennett, J. L., Wood, A., Smith, N., Mistry, R., Allen, K., Jandial, S., Tuckett, J. D., Gowdy, S. C., Foster, H. E., and McErlane, F. 2019. "Can quantitative MRI be used in the clinical setting to quantify the impact of intra-articular glucocorticoid injection on synovial disease activity in juvenile idiopathic arthritis?" *Pediatric Rheumatology* 17.1, pp. 1–12.

Bergin, C. J., Pauly, J. M., and Macovski, A. 1991. "Lung parenchyma: projection reconstruction MR imaging." *Radiology* 179.3, pp. 777–781.

Bernstein, M. A., King, K. F., and Zhou, X. J. 2004. *Handbook of MRI Pulse Sequences*. Elsevier.

Bloch, F. 1946. "Nuclear induction". *Physical Review* 70.7-8, p. 460.

Bloch, F. and Siegert, A. 1940. "Magnetic resonance for nonrotating fields". *Physical Review* 57.6, p. 522.

Breda, S. J., Poot, D. H., Papp, D., Vries, B. A. de, Kotek, G., Krestin, G. P., Hernández-Tamames, J. A., Vos, R.-J. de, and Oei, E. H. 2020. "Tissue-specific T_2^* biomarkers in patellar tendinopathy by subregional quantification using 3D ultrashort Echo time MRI". *Journal of Magnetic Resonance Imaging* 52.2, pp. 420–430.

Burakiewicz, J., Sinclair, C. D., Fischer, D., Walter, G. A., Kan, H. E., and Hollingsworth, K. G. 2017. "Quantifying fat replacement of muscle by quantitative MRI in muscular dystrophy". *Journal of Neurology* 264, pp. 2053–2067.

Bydder, G. M., Fullerton, G. D., and Young, I. R. 2012. *MRI of Tissues with Short T_2s or T_2^*s*. John Wiley & Sons.

Bydder, G. M., Steiner, R. E., Young, I., Hall, A., Thomas, D., Marshall, J., Pallis, C., and Legg, N. 1982. "Clinical NMR imaging of the brain: 140 cases". *American Journal of Neuroradiology* 3.5, pp. 459–480.

Cashmore, M. T., McCann, A. J., Wastling, S. J., McGrath, C., Thornton, J., and Hall, M. G. 2021. "Clinical quantitative MRI and the need for metrology". *The British Journal of Radiology* 94.1120, p. 20201215.

Christensen, K. A., Grant, D. M., Schulman, E. M., and Walling, C. 1974. "Optimal determination of relaxation times of Fourier transform nuclear magnetic resonance. Determination of spin-lattice relaxation times in chemically polarized species". *The Journal of Physical Chemistry* 78.19, pp. 1971–1977.

Collins, C. M., Liu, W., Schreiber, W., Yang, Q. X., and Smith, M. B. 2005. "Central brightening due to constructive interference with, without, and despite dielectric resonance". *Journal of Magnetic Resonance Imaging* 21.2, pp. 192–196.

Cristinacce, P. L. H., Keaveney, S., Aboagye, E. O., Hall, M. G., Little, R. A., O'Connor, J. P., Parker, G. J., Waterton, J. C., Winfield, J. M., and Jauregui-Osoro, M. 2022. "Clinical translation of quantitative magnetic resonance imaging biomarkers–An overview and gap analysis of current practice". *Physica Medica* 101, pp. 165–182.

Damon, B. M., Li, K., Dortch, R. D., Welch, E. B., Park, J. H., Buck, A. K., Towse, T. F., Does, M. D., Gochberg, D. F., and Bryant, N. D. 2016. "Quantitative magnetic resonance imaging of skeletal muscle disease". *Journal of Visualized Experiments* 118, e52352.

de Mello, R., Ma, Y., Ji, Y., Du, J., and Chang, E. Y. 2019. "Quantitative MRI MSK techniques: An update". *American Journal of Roentgenology* 213.3, pp. 524–533.

Dietrich, O., Reiser, M. F., and Schoenberg, S. O. 2008. "Artifacts in 3-T MRI: physical background and reduction strategies". *European Journal of Radiology* 65.1, pp. 29–35.

Dixon, W. T. 1984. "Simple proton spectroscopic imaging." *Radiology* 153.1, pp. 189–194.

Du, J. and Bydder, G. M. 2013. "Qualitative and quantitative ultrashort-TE MRI of cortical bone". *NMR in Biomedicine* 26.5, pp. 489–506.

Du, J., Chiang, A. J.-T., Chung, C. B., Statum, S., Znamirowski, R., Takahashi, A., and Bydder, G. M. 2010. "Orientational analysis of the Achilles tendon and enthesis using an ultrashort echo time spectroscopic imaging sequence". *Magnetic Resonance Imaging* 28.2, pp. 178–184.

Duck, F. 2013. *Physical properties of tissues: a comprehensive reference book*. Academic press.

Eck, B. L., Yang, M., Elias, J. J., Winalski, C. S., Altahawi, F., Subhas, N., and Li, X. 2023. "Quantitative MRI for evaluation of musculoskeletal disease: cartilage and muscle composition, joint inflammation, and biomechanics in osteoarthritis". *Investigative Radiology* 58.1, pp. 60–75.

Einstein, A. 1905. "Über die von der molekularkinetischen Theorie der Wärme geforderte Bewegung von in ruhenden Flüssigkeiten suspendierten Teilchen". *Annalen der Physik* 4.322, pp. 549–560.

Elliott, J. M., Hancock, M. J., Crawford, R. J., Smith, A. C., and Walton, D. M. 2018. "Advancing imaging technologies for patients with spinal pain: with a focus on whiplash injury". *The Spine Journal* 18.8, pp. 1489–1497.

Emanuelsson, E. B., Berry, D. B., Reitzner, S. M., Arif, M., Mardinoglu, A., Gustafsson, T., Ward, S. R., Sundberg, C. J., and Chapman, M. A. 2022. "MRI characterization of skeletal muscle size and fatty infiltration in long-term trained and untrained individuals". *Physiological Reports* 10.14, e15398.

Englund, E. K., Reiter, D. A., Shahidi, B., and Sigmund, E. E. 2022. "Intravoxel incoherent motion magnetic resonance imaging in skeletal muscle: review and future directions". *Journal of Magnetic Resonance Imaging* 55.4, pp. 988–1012.

Feng, X., Salerno, M., Kramer, C. M., and Meyer, C. H. 2016. "Non-Cartesian balanced steady-state free precession pulse sequences for real-time cardiac MRI". *Magnetic Resonance in Medicine* 75.4, pp. 1546–1555.

Fernandez-Seara, M. A., Song, H. K., and Wehrli, F. W. 2001. "Trabecular bone volume fraction mapping by low-resolution MRI". *Magnetic Resonance in Medicine* 46.1, pp. 103–113.

Fernández-Seara, M. A., Wehrli, S. L., and Wehrli, F. W. 2002. "Diffusion of exchangeable water in cortical bone studied by nuclear magnetic resonance". *Biophysical Journal* 82.1, pp. 522–529.

Filli, L., Boss, A., Wurnig, M. C., Kenkel, D., Andreisek, G., and Guggenberger, R. 2015. "Dynamic intravoxel incoherent motion imaging of skeletal muscle at rest and after exercise". *NMR in Biomedicine* 28.2, pp. 240–246.

Finni, T. 2006. "Structural and functional features of human muscle–tendon unit". *Scandinavian Journal of Medicine & Science in Sports* 16.3, pp. 147–158.

Fleckenstein, J. L., Canby, R. C., Parkey, R. W., and Peshock, R. M. 1988. "Acute effects of exercise on MR imaging of skeletal muscle in normal volunteers". *American Journal of Roentgenology* 151.2, pp. 231–237.

Flück, M., Kramer, M., Fitze, D. P., Kasper, S., Franchi, M. V., and Valdivieso, P. 2019. "Cellular Aspects of Muscle Specialization Demonstrate Genotype–Phenotype Interaction Effects in Athletes". *Frontiers in Physiology* 10, p. 526.

Forsting, J., Rohm, M., Froeling, M., Güttsches, A.-K., Südkamp, N., Roos, A., Vorgerd, M., Schlaffke, L., and Rehmann, R. 2022. "Quantitative muscle MRI captures early muscle degeneration in calpainopathy". *Scientific Reports* 12.1, p. 19676.

Franklin, K. M., Dale, B. M., and Merkle, E. M. 2008. "Improvement in B_1-inhomogeneity artifacts in the abdomen at 3T MR imaging using a radiofrequency cushion". *Journal of Magnetic Resonance Imaging* 27.6, pp. 1443–1447.

Fullerton, G. D. and Rahal, A. 2007. "Collagen structure: the molecular source of the tendon magic angle effect". *Journal of Magnetic Resonance Imaging* 25.2, pp. 345–361.

Gold, G. E., Han, E., Stainsby, J., Wright, G., Brittain, J., and Beaulieu, C. 2004. "Musculoskeletal MRI at 3.0 T: relaxation times and image contrast". *American Journal of Roentgenology* 183.2, pp. 343–351.

Granziera, C., Wuerfel, J., Barkhof, F., Calabrese, M., De Stefano, N., Enzinger, C., Evangelou, N., Filippi, M., Geurts, J. J., and Reich, D. S. 2021. "Quantitative magnetic resonance imaging towards clinical application in multiple sclerosis". *Brain* 144.5, pp. 1296–1311.

Green, R. and Wilson, D. 2000. "A pilot study using magnetic resonance imaging to determine the pattern of muscle group recruitment by rowers with different levels of experience". *Skeletal Radiology* 29, pp. 196–203.

Grimm, A., Meyer, H., Nickel, M., Nittka, M., Raithel, E., Chaudry, O., Friedberger, A., Uder, M., Kemmler, W., and Engelke, K. 2019. "A comparison between 6-point Dixon MRI and MR spectroscopy to quantify muscle fat in the thigh of subjects with sarcopenia". *The Journal of Frailty & Aging* 8, pp. 21–26.

Gurney, P. T., Hargreaves, B. A., and Nishimura, D. G. 2006. "Design and analysis of a practical 3D cones trajectory". *Magnetic Resonance in Medicine* 55.3, pp. 575–582.

Haacke, E. M. 1999. *Magnetic resonance imaging: physical principles and sequence design*. John Wiley & Sons.

Haacke, E. M., Xu, Y., Cheng, Y.-C. N., and Reichenbach, J. R. 2004. "Susceptibility weighted imaging (SWI)". *Magnetic Resonance in Medicine* 52.3, pp. 612–618.

Haase, A., Frahm, J., Matthaei, D., Hänicke, W., and Merboldt, K.-D. 1986. "FLASH imaging. Rapid NMR imaging using low flip-angle pulses". *Journal of Magnetic Resonance* 67.2, pp. 258–266.

Hadjicostas, P. T., Soucacos, P. N., Berger, I., Koleganova, N., and Paessler, H. H. 2007. "Comparative analysis of the morphologic structure of quadriceps and patellar tendon: a descriptive laboratory study". *Arthroscopy: The Journal of Arthroscopic & Related Surgery* 23.7, pp. 744–750.

Hansen, P., Bojsen-Moller, J., Aagaard, P., Kjaer, M., and Magnusson, S. P. 2006. "Mechanical properties of the human patellar tendon, in vivo". *Clinical Biomechanics* 21.1, pp. 54–58.

Hata, J., Endo, K., Tsuji, O., Arakawa, S., Sato, M., Yagi, K., Fujiyoshi, K., Okano, H., and Nakamura, M. 2019. "Analysis of skeletal-muscle condition after excessive loading of the lower legs by sequential magnetic resonance imaging". *Journal of Orthopaedic Science* 24.5, pp. 873–880.

Herrmann, K.-H., Krämer, M., and Reichenbach, J. R. 2016. "Time efficient 3D radial UTE sampling with fully automatic delay compensation on a clinical 3T MR scanner". *PLoS One* 11.3, e0150371.

Hiepe, P., Gussew, A., Rzanny, R., Anders, C., Walther, M., Scholle, H.-C., and Reichenbach, J. R. 2014. "Interrelations of muscle functional MRI, diffusion-weighted MRI and 31P-MRS in exercised lower back muscles". *NMR in Biomedicine* 27.8, pp. 958–970.

Hiepe, P., Rzanny, R., Gussew, A., Anders, C., Scholle, H., and Reichenbach, J. 2012. "Functional diffusion weighted MRI for assessment of muscle fatigue in the lower back muscles". *Biomedical Engineering/Biomedizinische Technik* 57.SI-1-Track-B, p. 512.

Hirschmann, M. T. and Müller, W. 2015. "Complex function of the knee joint: the current understanding of the knee". *Knee Surgery, Sports Traumatology, Arthroscopy* 23, pp. 2780–2788.

Hooijmans, M. T., Damon, B., Froeling, M., Versluis, M., Burakiewicz, J., Verschuuren, J., Niks, E., Webb, A., and Kan, H. 2015. "Evaluation of skeletal muscle DTI in patients with duchenne muscular dystrophy". *NMR in Biomedicine* 28.11, pp. 1589–1597.

Hoult, D. I. 2000. "The principle of reciprocity in signal strength calculations—a mathematical guide". *Concepts in Magnetic Resonance* 12.4, pp. 173–187.

Janssen, B. H., Pillen, S., Voet, N. B., Heerschap, A., Engelen, B. G. van, and Alfen, N. van. 2014. "Quantitative muscle ultrasound versus quantitative magnetic resonance imaging in facioscapulohumeral dystrophy". *Muscle & Nerve* 50.6, pp. 968–975.

Jerban, S., Ma, Y., Namiranian, B., Ashir, A., Shirazian, H., Wei, Z., Le, N., Wu, M., Cai, Z., and Du, J. 2019. "Age-related decrease in collagen proton fraction in tibial tendons estimated by magnetization transfer modeling of ultrashort echo time magnetic resonance imaging (UTE-MRI)". *Scientific Reports* 9.1, p. 17974.

Johnson, K. M., Fain, S. B., Schiebler, M. L., and Nagle, S. 2013. "Optimized 3D ultrashort echo time pulmonary MRI". *Magnetic Resonance in Medicine* 70.5, pp. 1241–1250.

Kalia, V., Leung, D. G., Sneag, D. B., Del Grande, F., and Carrino, J. A. 2017. "Advanced MRI techniques for muscle imaging". *Seminars in Musculoskeletal Radiology*. Vol. 21. 04. Thieme Medical Publishers, pp. 459–469.

Keenan, K. E., Biller, J. R., Delfino, J. G., Boss, M. A., Does, M. D., Evelhoch, J. L., Griswold, M. A., Gunter, J. L., Hinks, R. S., and Hoffman, S. W. 2019. "Recommendations towards standards for quantitative MRI (qMRI) and outstanding needs". *Journal of Magnetic Resonance Imaging* 49.7, e26.

Keenan, K. E., Gimbutas, Z., Dienstfrey, A., Stupic, K. F., Boss, M. A., Russek, S. E., Chenevert, T. L., Prasad, P., Guo, J., and Reddick, W. E. 2021. "Multi-site, multi-platform comparison of MRI T 1 measurement using the system phantom". *PloS One* 16.6, e0252966.

Keller, S., Yamamura, J., Sedlacik, J., Wang, Z., Gebert, P., Starekova, J., and Tahir, E. 2020. "Diffusion tensor imaging combined with T_2 mapping to quantify changes in the skeletal muscle associated with training and endurance exercise in competitive triathletes". *European Radiology* 30, pp. 2830–2842.

Kijowski, R., Wilson, J. J., and Liu, F. 2017. "Bicomponent ultrashort echo time analysis for assessment of patients with patellar tendinopathy". *Journal of Magnetic Resonance Imaging* 46.5, pp. 1441–1447.

Kollmer, J., Kessler, T., Sam, G., Hayes, J. M., Lentz, S. I., Heiland, S., Bendszus, M., Wick, W., and Weiler, M. 2021. "Magnetization transfer ratio: a quantitative imaging biomarker for 5q spinal muscular atrophy". *European Journal of Neurology* 28.1, pp. 331–340.

Krämer, M., Maggioni, M., Brisson, N., Zachow, S., Teichgräber, U., Duda, G., and Reichenbach, J. 2019. "T_1 and T_2* mapping of the human quadriceps and patellar tendons using ultra-short echo-time (UTE) imaging and bivariate relaxation parameter-based volumetric visualization". *Magnetic Resonance Imaging* 63, pp. 29–36.

Kronthaler, S., Rahmer, J., Börnert, P., Makowski, M. R., Schwaiger, B. J., Gersing, A. S., and Karampinos, D. C. 2021. "Trajectory correction based on the gradient impulse response function improves high-resolution UTE imaging of the musculoskeletal system". *Magnetic Resonance in Medicine* 85.4, pp. 2001–2015.

Kucharz, E. J. 1992. "Musculoskeletal system". *The Collagens: Biochemistry and Pathophysiology*, pp. 149–175.

Le Bihan, D. 2019. "What can we see with IVIM MRI?" *Neuroimage* 187, pp. 56–67.

Le Bihan, D., Breton, E., Lallemand, D., Aubin, M.-L., Vignaud, J., and Laval-Jeantet, M. 1988. "Separation of diffusion and perfusion in intravoxel incoherent motion MR imaging." *Radiology* 168.2, pp. 497–505.

Lins, C. F., Salmon, C. E. G., and Nogueira-Barbosa, M. H. 2020. "Applications of the Dixon technique in the evaluation of the musculoskeletal system". *Radiologia Brasileira* 54, pp. 33–42.

Loegering, I. F., Denning, S. C., Johnson, K. M., Liu, F., Lee, K. S., and Thelen, D. G. 2021. "Ultrashort echo time (UTE) imaging reveals a shift in bound water that is sensitive to sub-clinical tendinopathy in older adults". *Skeletal Radiology* 50.1, pp. 107–113.

Lyu, X., Gao, Y., Liu, Q., Zhao, H., Zhou, H., and Pan, S. 2021. "Exercise-induced muscle damage: multi-parametric MRI quantitative assessment". *BMC Musculoskeletal Disorders* 22, pp. 1–13.

Ma, J. 2008. "Dixon techniques for water and fat imaging". *Journal of Magnetic Resonance Imaging* 28.3, pp. 543–558.

Ma, Y.-j., Lu, X., Carl, M., Zhu, Y., Szeverenyi, N. M., Bydder, G. M., Chang, E. Y., and Du, J. 2018. "Accurate T_1 mapping of short T_2 tissues using a three-dimensional ultrashort echo time cones actual flip angle imaging-variable repetition time (3D UTE-Cones AFI-VTR) method". *Magnetic Resonance in Medicine* 80.2, pp. 598–608.

Ma, Y.-j., Zhao, W., Wan, L., Guo, T., Searleman, A., Jang, H., Chang, E. Y., and Du, J. 2019. "Whole knee joint $T_{1\rho}$ values measured in vivo at 3T by combined 3D ultrashort echo time cones actual flip angle and variable flip angle methods". *Magnetic Resonance in Medicine* 81.3, pp. 1634–1644.

Maggioni, M. B., Krämer, M., and Reichenbach, J. R. 2021a. "Accelerated 3D-UTE-AFI B_1 mapping to correct VFA-based T_1 estimations in short T_2^* tissues". *Proc. Int. Soc. Magn. Reson. Med.*, p. 3305.

— 2021b. "Optimized gradient spoiling of UTE VFA-AFI sequences for robust T_1 estimation with B_1-field correction". *Magnetic Resonance Imaging* 82, pp. 1–8.

Marden, F. A., Connolly, A. M., Siegel, M. J., and Rubin, D. A. 2005. "Compositional analysis of muscle in boys with Duchenne muscular dystrophy using MR imaging". *Skeletal Radiology* 34, pp. 140–148.

Marini, M. and Veicsteinas, A. 2010. "The exercised skeletal muscle: a review". *European Journal of Translational Myology* 20.3, pp. 105–120.

Márquez-Flórez, K., Shefelbine, S., Ramírez-Martínez, A., and Garzón-Alvarado, D. 2018. "Computational model for the patella onset". *PloS One* 13.12, e0207770.

Matzat, S. J., Tiel, J. van, Gold, G. E., and Oei, E. H. 2013. "Quantitative MRI techniques of cartilage composition". *Quantitative Imaging in Medicine and Surgery* 3.3, pp. 162–174.

Mazzoli, V., Oudeman, J., Nicolay, K., Maas, M., Verdonschot, N., Sprengers, A. M., Nederveen, A. J., Froeling, M., and Strijkers, G. J. 2016. "Assessment of passive muscle elongation using Diffusion Tensor MRI: Correlation between fiber length and diffusion coefficients". *NMR in Biomedicine* 29.12, pp. 1813–1824.

Mendez-Villanueva, A., Suarez-Arrones, L., Rodas, G., Fernandez-Gonzalo, R., Tesch, P., Linnehan, R., Kreider, R., and Di Salvo, V. 2016. "MRI-based regional muscle use during hamstring strengthening exercises in elite soccer players". *PLoS One* 11.9, e0161356.

Menon, R. G., Raghavan, P., and Regatte, R. R. 2019. "Quantifying muscle glycosaminoglycan levels in patients with post-stroke muscle stiffness using $T_{1\rho}$ MRI". *Scientific Reports* 9.1, p. 14513.

Mosher, T. J. 2006. "Musculoskeletal imaging at 3T: current techniques and future applications". *Magnetic Resonance Imaging Clinics* 14.1, pp. 63–76.

Mukund, K. and Subramaniam, S. 2020. "Skeletal muscle: A review of molecular structure and function, in health and disease". *Wiley Interdisciplinary Reviews: Systems Biology and Medicine* 12.1, e1462.

Nehrke, K. 2009. "On the steady-state properties of actual flip angle imaging (AFI)". *Magnetic Resonance in Medicine* 61.1, pp. 84–92.

Noehren, B., Hardy, P. A., Andersen, A., Brightwell, C. R., Fry, J. L., Vandsburger, M. H., Thompson, K. L., and Fry, C. S. 2021. "$T_{1\rho}$ imaging as a non-invasive assessment of collagen remodelling and organization in human skeletal muscle after ligamentous injury". *The Journal of Physiology* 599.23, pp. 5229–5242.

Nygren, A. T., Greitz, D., and Kaijser, L. 2000. "Changes in cross-sectional area in human exercising and non-exercising skeletal muscles". *European Journal of Applied Physiology* 81, pp. 210–213.

Okoroha, K. R., Mehran, N., Duncan, J., Washington, T., Spiering, T., Bey, M. J., Van Holsbeeck, M., and Moutzouros, V. 2017. "Characterization of rotator cuff tears: ultrasound versus magnetic resonance imaging". *Orthopedics* 40.1, e124–e130.

Pedersen, B. K. 2011. "Muscle as a secretory organ". *Comprehensive Physiology* 3.3, pp. 1337–1362.

Pinckard, K., Baskin, K. K., and Stanford, K. I. 2019. "Effects of exercise to improve cardiovascular health". *Frontiers in Cardiovascular Medicine* 6, pp. 69–81.

Portakal, Z. G., Shermer, S., Jenkins, C., Spezi, E., Perrett, T., Tuncel, N., and Phillips, J. 2018. "Design and characterization of tissue-mimicking gel phantoms for diffusion kurtosis imaging". *Medical Physics* 45.6, pp. 2476–2485.

Pownder, S. L., Neri, J. P., Hayashi, K., Vanderbeek, A. M., and Koff, M. F. 2022. "Age and Sex Comparison of the Canine Supraspinatus Tendon Using Quantitative Magnetic Resonance Imaging T_2 Mapping". *Veterinary and Comparative Orthopaedics and Traumatology* 36.02, pp. 087–092.

Purcell, E. M., Torrey, H. C., and Pound, R. V. 1946. "Resonance absorption by nuclear magnetic moments in a solid". *Physical Review* 69.1-2, pp. 37–38.

Qian, Y., Williams, A. A., Chu, C. R., and Boada, F. E. 2012. "High-resolution ultrashort echo time (UTE) imaging on human knee with AWSOS sequence at 3.0 T". *Journal of Magnetic Resonance Imaging* 35.1, pp. 204–210.

Reichenbach, J., Schweser, F., Serres, B., and Deistung, A. 2015. "Quantitative susceptibility mapping: concepts and applications". *Clinical Neuroradiology* 25, pp. 225–230.

Robson, M. D., Benjamin, M., Gishen, P., and Bydder, G. 2004. "Magnetic resonance imaging of the Achilles tendon using ultrashort TE (UTE) pulse sequences". *Clinical Radiology* 59.8, pp. 727–735.

Sacolick, L. I., Wiesinger, F., Hancu, I., and Vogel, M. W. 2010. "B_1 mapping by Bloch-Siegert shift". *Magnetic Resonance in Medicine* 63.5, pp. 1315–1322.

Schönau, T. and Anders, C. 2023. "Force capacity of trunk muscle extension and flexion in healthy inactive, endurance and strength-trained subjects—a pilot study". *German Journal of Exercise and Sport Research*, pp. 1–8.

Schweser, F., Deistung, A., Lehr, B. W., and Reichenbach, J. R. 2011. "Quantitative imaging of intrinsic magnetic tissue properties using MRI signal phase: an approach to in vivo brain iron metabolism?" *Neuroimage* 54.4, pp. 2789–2807.

Sinclair, C., Morrow, J., Miranda, M., Davagnanam, I., Cowley, P., Mehta, H., Hanna, M., Koltzenburg, M., Yousry, T., and Reilly, M. 2012. "Skeletal muscle MRI magnetisation transfer ratio reflects clinical severity in peripheral neuropathies". *Journal of Neurology, Neurosurgery & Psychiatry* 83.1, pp. 29–32.

Sions, J. M., Elliott, J. M., Pohlig, R. T., and Hicks, G. E. 2017. "Trunk muscle characteristics of the multifidi, erector spinae, psoas, and quadratus lumborum in older adults with and without chronic low back pain". *Journal of Orthopaedic & Sports Physical Therapy* 47.3, pp. 173–179.

Sled, J. G. and Pike, G. B. 1998. "Standing-wave and RF penetration artifacts caused by elliptic geometry: an electrodynamic analysis of MRI". *IEEE Transactions on Medical Imaging* 17.4, pp. 653–662.

Solomon, D. H., Katz, J. N., Carrino, J. A., Schaffer, J. L., Bohn, R. L., Mogun, H., and Avorn, J. 2003. "Trends in knee magnetic resonance imaging". *Medical care*, pp. 687–692.

Stahl, R., Luke, A., Li, X., Carballido-Gamio, J., Ma, C. B., Majumdar, S., and Link, T. M. 2009. "$T_{1\rho}$, T 2 and focal knee cartilage abnormalities in physically active and sedentary healthy subjects versus early OA patients—A 3.0-tesla MRI study". *European Radiology* 19, pp. 132–143.

Stejskal, E. O. and Tanner, J. E. 1965. "Spin diffusion measurements: spin echoes in the presence of a time-dependent field gradient". *The Journal of Chemical Physics* 42.1, pp. 288–292.

Tadros, A. S., Huang, B. K., and Pathria, M. N. 2018. "Muscle-tendon-enthesis unit". *Seminars in Musculoskeletal Radiology*. Vol. 22. 03. Thieme Medical Publishers, pp. 263–274.

Thompson, L. V. 1994. "Effects of age and training on skeletal muscle physiology and performance". *Physical Therapy* 74.1, pp. 71–81.

Tyler, D. J., Robson, M. D., Henkelman, R. M., Young, I. R., and Bydder, G. M. 2007. "Magnetic resonance imaging with ultrashort TE (UTE) PULSE sequences: technical considerations". *Journal of Magnetic Resonance Imaging* 25.2, pp. 279–289.

Van Middelkoop, M., Rubinstein, S. M., Verhagen, A. P., Ostelo, R. W., Koes, B. W., and Tulder, M. W. van. 2010. "Exercise therapy for chronic nonspecific low-back pain". *Best practice & research Clinical rheumatology* 24.2, pp. 193–204.

Varghese, J., Scandling, D., Joshi, R., Aneja, A., Craft, J., Raman, S. V., Rajagopalan, S., Simonetti, O. P., and Mihai, G. 2015. "Rapid assessment of quantitative T_1, T_2 and T_2^* in lower extremity muscles in response to maximal treadmill exercise". *NMR in Biomedicine* 28.8, pp. 998–1008.

Visser, J. J., Goergen, S. K., Klein, S., Noguerol, T. M., Pickhardt, P. J., Fayad, L. M., and Omoumi, P. 2020. "The value of quantitative musculoskeletal imaging". *Seminars in Musculoskeletal Radiology*. Vol. 24. 04. Thieme Medical Publishers, pp. 460–474.

Wang, D., Zwart, N. R., Li, Z., Schär, M., and Pipe, J. G. 2016. "Analytical three-point Dixon method: With applications for spiral water–fat imaging". *Magnetic resonance in medicine* 75.2, pp. 627–638.

Wang, L. and Regatte, R. R. 2015. "$T_{1\rho}$ MRI of human musculoskeletal system". *Journal of Magnetic Resonance Imaging* 41.3, pp. 586–600.

Wáng, Y.-X. J., Zhang, Q., Li, X., Chen, W., Ahuja, A., and Yuan, J. 2015. "$T_{1\rho}$ magnetic resonance: basic physics principles and applications in knee and intervertebral disc imaging". *Quantitative Imaging in Medicine and Surgery* 5.6, pp. 858–885.

Wengler, K., Fukuda, T., Tank, D., Komatsu, D. E., Paulus, M., Huang, M., Gould, E. S., Schweitzer, M. E., and He, X. 2020. "In vivo evaluation of human patellar tendon microstructure and microcirculation with diffusion MRI". *Journal of Magnetic Resonance Imaging* 51.3, pp. 780–790.

Wokke, B. H., Bos, C., Reijnierse, M., Rijswijk, C. S. van, Eggers, H., Webb, A., Verschuuren, J. J., and Kan, H. E. 2013. "Comparison of dixon and T_1-weighted MR methods to assess the degree of fat infiltration in duchenne muscular dystrophy patients". *Journal of Magnetic Resonance Imaging* 38.3, pp. 619–624.

Wu, M., Zhao, W., Wan, L., Kakos, L., Li, L., Jerban, S., Jang, H., Chang, E. Y., Du, J., and Ma, Y.-J. 2020. "Quantitative three-dimensional ultrashort echo time cones imaging of the knee joint with motion correction". *NMR in Biomedicine* 33.1, e4214.

Yarnykh, V. L. 2007. "Actual flip-angle imaging in the pulsed steady state: a method for rapid three-dimensional mapping of the transmitted radiofrequency field". *Magnetic Resonance in Medicine* 57.1, pp. 192–200.

Zaeske, C., Brueggemann, G.-P., Willwacher, S., Maehlich, D., Maintz, D., and Bratke, G. 2022. "The behaviour of T_2^* and T_2 relaxation time in extrinsic foot muscles under continuous exercise: A prospective analysis during extended running". *PloS One* 17.2, e0264066.

Zelaya, F. O., Roffmann, W. U., Crozier, S., Teed, S., Gross, D., and Doddrell, D. M. 1997. "Direct visualisation of B_1 inhomogeneity by flip angle dependency". *Magnetic Resonance Imaging* 15.4, pp. 497–504.

Zlatkin, M. B., Iannotti, J., Roberts, M., Esterhai, J., Dalinka, M., Kressel, H., Schwartz, J. S., and Lenkinski, R. 1989. "Rotator cuff tears: diagnostic performance of MR imaging." *Radiology* 172.1, pp. 223–229.

Zoga, A. C., Kamel, S. I., Hynes, J. P., Kavanagh, E. C., O'Connor, P. J., and Forster, B. B. 2021. "The evolving roles of MRI and ultrasound in first-line imaging of rotator cuff injuries". *American Journal of Roentgenology* 217.6, pp. 1390–1400.

Zur, Y., Wood, M. L., and Neuringer, L. J. 1991. "Spoiling of transverse magnetization in steady-state sequences". *Magnetic Resonance in Medicine* 21.2, pp. 251–263.